

Diss. ETH No. 15700

Modeling and Compensation of the Fuel Path Dynamics of a Spark Ignited Engine

A dissertation submitted to the
SWISS FEDERAL INSTITUTE OF TECHNOLOGY
ZURICH

for the degree of
Doctor of Technical Sciences
presented by

MARZIO A. LOCATELLI

Dipl. Masch.-Ing. ETH

born December 9, 1975

citizen of Lugano, TI, Switzerland

accepted on the recommendation of

Prof. Dr. H. P. Geering, examiner

Prof. Dr. Ph. Rudolf von Rohr, co-examiner

2004

ISBN 3-906483-07-X

IMRT Press
c/o Institut für Mess- und Regeltechnik
ETH Zentrum
8092 Zürich
Schweiz

11/2004

Acknowledgements

This thesis was written at the Measurement and Control Laboratory from 2000 to 2004 in cooperation with the Robert Bosch company. During this period I have been in contact with many people, who I would like to thank.

- First of all, I would like to thank my supervisor, Prof. Dr. Hans Peter Geering for his support throughout the whole process, in particular at the end of the thesis.
- My thanks also go to Prof. Dr. Rudolf vor Rohr, who agreed to be my co-examiner.
- My special thanks go to the technical staff of the laboratory. In particular I would like to thank the head mechanic Hans Ulrich Honegger and the electronic specialist Daniel Matter. Without their contribute, the time spent on the test bench would have been doubled.
- Many thanks go to all the past and present colleagues at IMRT, among them Michael Simons and Theo Auckenthaler, with whom I shared office and theorized the existence of the OB space. In addition: Oli Tanner, Carlos Cuelar, David Zogg, Roberto Cirillo, Roger Wimmer, Mikael Bianchi, Brigitte Rohrbach, Essi Shafai, and all the others.

- I thank also Chris Onder for his help on the technical issues and for sharing his large experience on the field, and Raymond Turin for his greatest support and the various interesting discussions. In particular I owe Raymond for helping me to focus on the actual requirements of the automotive industry.
- As they played an important role, I cannot forget to thank all the diploma and term paper students, who helped me by the realization of parts of this thesis: Marco Ancona, Ezio Alfieri, Luca Sormani, Igor Pasta, Gabriel Barroso, Michele Marotta, and Roland Benz.
- Finally, I want to thank my family for allowing me to study at the ETH. The last special thanks go to my girlfriend Marina for her greatest support.

Abstract

In the last decade, the technical evolution of the combustion engines has reached an high level of growth. This evolution was surely triggered by the increasing restrictions for the emission levels imposed by the governments. The direct consequence of this improvement is an increase in the complexity of the engine management systems, which means an increase of algorithms that have to be parameterized. To cope with this complexity, the current parametrization methods have to be refined. For instance, the implementation of parametrical models based on physical principles can reduce dramatically the time spent on the test-bench to calibrate a specific engine.

This thesis is focused on the modeling of the fuel path dynamics, from the injection of the fuel into the intake manifold up to the measurement of the air/fuel ratio in the exhaust, for a Port Fuel Injected engine (PFI engine). The main dynamics which are present in the fuel path are the wall wetting dynamics and the exhaust gas dynamics. They represent the storage and evaporation of fuel in the intake manifold, and the mixing of the fuel vapor in the cylinder and in the exhaust. On one hand, the goal is to obtain a model with a simple structure (control-oriented modeling) and based on few tunable parameters, so that it can be implemented easily in a standard engine management system. On the other hand, the obtained model has to cover the whole operating

region of an engine, including the operating condition which can only occur by particular unexpected events.

The investigation is conducted on a single cylinder of a V6 engine. To estimate the fuel mass in the cylinder, a continuous air/fuel ratio meter is used, which is mounted very near to the exhaust valves. In addition to this sensor, a very fast NO measurement device is used in the same spot to calibrate the model of the exhaust gas dynamics. The optimal placement of these sensors is investigated by means of a preliminary study of the fluid waves in the exhaust.

Firstly, all the dynamics which are adjacent to the wall wetting are investigated, namely, the intake manifold dynamics, the exhaust gas dynamics, and the sensor dynamics. To identify the parameters of the model of the exhaust gas dynamics, i.e., everything that occurs between cylinder and sensor, a linear approach is chosen. This model can be treated separately without disturbing the wall wetting dynamics with the NO device, because the system can be excited maintaining a constant air mass flow and a constant fuel mass flow. As additional result of this method, the residual gas fraction can be estimated. At this point of the investigation, the effects of the wall wetting system can be measured without interferences.

Secondly, the model structure of the wall wetting dynamics is built on the basis of the phenomenon of physics known as forced convection with phase change. The model is separated into two main blocks: the evaporation of the droplets, and the evaporation of the wall film. The combination of these models describes the nonlinear wall wetting dynamics, i.e., everything that occurs to the fuel upstream the cylinder.

The parameters of the wall wetting model are identified by means of off-line optimizations and the Kalman filtering technique is used to produce an observer and an on-line estimator.

The obtained model and the observer are used as basis for the wall wetting compensator with two different approaches. In the first approach, the parameters of a linear compensator are calculated on the basis of the model and used with a LPV technique. The other approach implies the use of the observed value of the evaporation mass in the cylinder to calculate the fuel mass to be injected.

The results of the compensator show that the use of the LPV method yields the best results. The compensator is able to cope with difficult operating conditions, like those represented by warming-up engine temperatures, as happens during the first phase after a cold start of the engine.

Riassunto

Nell'ultima decade, l'evoluzione tecnologica dei motori a combustione interna ha raggiunto un notevole livello di crescita. Questa evoluzione é stata sicuramente incoraggiata dalle crescenti restrizioni imposte dai governi in materia di livelli massimi di emissioni. La conseguenza diretta di questo miglioramento e senz'altro l'aumento di complessità dei sistemi di gestione elettronica, il che comporta un aumento del numero di algoritmi da parametrizzare. Per potersi mantenere al passo con questa complessità, i metodi di ottimizzazione esistenti devono essere migliorati. Per esempio, utilizzando dei modelli parametrici basati su eventi fisici in modo da ridurre sensibilmente il tempo necessario al banco prova per calibrare un motore specifico.

Il tema principale di questa tesi é la modellazione delle dinamiche relative al percorso del carburante, dalla sua iniezione alla misurazione del rapporto di miscela nello scarico, per un motore multi-point (PFI engine). Le principali dinamiche che influenzano il percorso del carburante sono il film bagnato (wall wetting) e la dinamica dei gas di scarico. Esse rappresentano l'effetto di stoccaggio e di evaporazione del combustibile, e una miscelazione dei vapori del combusto all'interno del cilindro e dello scarico. Lo scopo finale é lo sviluppo di un modello con una struttura semplice (modellazione orientata al controllo) ma basato su pochi parametri adattabili, così che possa coprire tutto lo spettro di fun-

zionamento del motore (inclusi i tagli di alimentazione). I requisiti per il modello sono dunque di compromesso. Da una parte il sistema deve mantenere una struttura semplice con pochi parametri da identificare, d'altra parte il modello deve riprodurre adeguatamente il sistema non lineare nei punti di difficile misurazione.

Lo studio é condotto su di un singolo cilindro di un motore 6 cilindri a V. Per stimare la massa di carburante presente nel cilindro, si utilizza un sensore λ continuo montato molto vicino alle valvole di scarico. Oltre a questo sensore ci si avvale di un apparecchio di misurazione rapida di NO per ottimizzare il modello per la dinamica dello scarico. Il piazzamento ottimale di questi sensori é oggetto di uno studio preliminare sui flussi nel condotto di scarico.

Come prima cosa sono studiate tutte le dinamiche adiacenti al film bagnato, ovvero la dinamica del condotto d'aspirazione, la dinamica dei gas di scarico, e la dinamica del sensore λ . Per identificare i parametri del modello della dinamica dei gas di scarico, ovvero tutto quello che succede tra il cilindro e il sensore, é stato scelto un approccio lineare. Questo modello puo essere trattato separatamente senza disturbare la dinamica del film bagnato grazie al sensore di NO, perché il sistema puo essere eccitato mantenendo costanti la massa d'aria e di benzina nel cilindro. Come risultato aggiuntivo, la frazione di gas residui nel cilindro puo essere stimata. A questo punto del lavoro, gli effetti della dinamica del film bagnato possono essere misurati senza interferenze.

Come seconda cosa la struttura della dinamica del film bagnato é stata costruita sulla base del fenomeno fisico conosciuto come convezione forzata con cambiamento di fase. Il modello é separato in due blocchi principali: l'evaporazione delle gocce, e l'evaporazione del film bagnato. La combinazione di questi due blocchi descrive la dinamica complessa del film bagnato, ovvero tutto quello che succede al combustibile a monte del cilindro.

I parametri del modello del film bagnato sono stati stimati grazie ad ottimizzazioni e alle tecniche basate sul filtro di Kalman.

Per identificare i parametri del modello dei gas di scarico, ovvero tutto ciò che succede tra cilindro e sensore, è stato scelto un approccio lineare. Si è potuto identificare questo modello separatamente perché, grazie agli esperimenti sull'angolo di anticipo, è stato possibile eccitare il sistema senza disturbare la dinamica del film bagnato. Come risultato accessorio, la frazione di gas residui può essere stimata.

A questo punto dello studio gli effetti del sistema del film bagnato possono essere misurati senza interferenze per mezzo di ottimizzazione off-line e con tecniche basate sui filtri di Kalman.

Il modello così ottenuto e il suo osservatore sono stati utilizzati come base per il compensatore del film bagnato grazie a due approcci differenti. Da una parte, i parametri di un compensatore lineare sono calcolati e utilizzati con una metodologia di tipo LPV (Linear Parameter Varying). L'altro metodo implica l'uso del valore stimato della massa evaporata verso il cilindro per calcolare la massa di benzina da iniettare.

I risultati ottenuti con il compensatore mostrano che il metodo LPV dà i risultati migliori. Il compensatore è in grado di lavorare in condizioni operative rappresentate da temperature del motore crescenti, ovvero durante la prima fase dopo l'accensione a freddo del motore.

Contents

1. Introduction	1
1.1. Motivation	1
1.2. Strategy and Structure of the Thesis	4
1.2.1. Strategy	4
1.2.2. Structure of the Thesis	5
2. Experimental Conditions	7
2.1. Description of the Test Bench	7
2.1.1. DSP-Motronic and ICX-3	11
2.1.2. Description of the Sensors	14
2.2. Adequate Sensors Position	16
2.2.1. Method of Characteristics	16
2.3. Discussion	26
3. Dynamics Adjacent to the Wall Wetting	27
3.1. Introduction	27
3.2. Intake Manifold Model	29
3.3. Estimation of the Exhaust Gas Dynamics	34
3.3.1. Measurement Setup	34
3.3.2. Models for the Elements of the Exhaust Gas Dynamics	35
3.3.3. Identification of the Parameters	42
3.3.4. Influence of External EGR on the Structure of the Model	52

Contents

3.3.5. Identification Results	55
3.4. Discussion	59
4. Model of the Wall Wetting Dynamics based on Physics	61
4.1. Introduction	61
4.2. Description of the Convection Phenomenon	62
4.2.1. Free Convection	62
4.2.2. Forced Convection	62
4.2.3. Reynolds Analogy	64
4.2.4. Evaporating Fuel Mass	65
4.2.5. Fuel Properties	67
4.3. Droplet Evaporation	69
4.3.1. Forced Convection on a Droplet	69
4.3.2. Description of the Model	71
4.3.3. Impact Model of the Droplets on the Wall	72
4.3.4. Main Dependencies and Tuning Parameters	76
4.3.5. Temperature Model for the Droplets	78
4.4. Results of the Droplet Model	80
4.4.1. Event-Based Wall Wetting Model	80
4.4.2. Comparison between Model-based Parameters and Aquino Parameters	83
4.5. Wall Film Evaporation	86
4.5.1. Free and Forced Convection on the Wall Film	87
4.5.2. Fuel Film Flow in the Intake	88
4.5.3. Assumption for the Wall Film Geometry	91
4.5.4. Main Dependencies and Tuning Parameters	94
4.6. Results of the Wall Film Model	98
4.6.1. Identified Parameters	98
4.6.2. Comparison between Model-based Parameters and Simons' Parameters	99
4.7. Temperature Model of the Intake Valve	102
4.7.1. Physical Background	102

4.7.2.	Intake-Valve Thermal Balance	104
4.7.3.	Intake-Valve Duct Thermal Balance	109
4.8.	Discussion	114
5.	Identification of the Wall Wetting Parameters	115
5.1.	Introduction	115
5.2.	Off-Line Optimization	117
5.2.1.	Starting Point	117
5.2.2.	Off-Line Method	118
5.2.3.	Description of the Experiments	119
5.3.	On-Line Optimization	131
5.3.1.	Kalman Filter	131
5.3.2.	Extended Kalman Filter Applied to the Wall Film and the Exhaust	136
5.3.3.	First Step	142
5.3.4.	Second Step	150
5.4.	Discussion	155
6.	Wall Wetting Compensator	157
6.1.	Introduction	157
6.2.	Compensation of the Timing Error	159
6.3.	LPV Structure of Aquino	161
6.3.1.	Design of the Compensator	164
6.3.2.	Stability of the Compensator	165
6.4.	Compensator Based on the Estimated State Variables	170
6.5.	Results with the Compensators	174
6.5.1.	Experiments with Fuel Modulation	174
6.5.2.	Experiments with Throttle Tip-In and Tip- Out	176
6.5.3.	Experiments on the Test Bench	179
6.6.	Discussion	182

Contents

7. Conclusions	183
A. Frequency Response Plots	187
Curriculum Vitae	199

List of Symbols

Indexes

0	Reference state
A	Related to air
D	Related to droplets
d	Related to duct
F	Related to fuel film
I	Related to intake manifold
k	Related to discrete time k
M	Related to reference model
W	Related to wall
NO	Related to NO gas
cyl	Related to cylinder
EG	Related to exhaust gas
in	Related to incoming
LSU	Related to broadband A/F Sensor

List of Symbols

out	Related to outgoing
U	Related to ambient conditions

Greek Symbols

$\alpha_{Th,0}$	Throttle closed angle	[rad]
α_{Th}	Throttle angle	[rad]
$\chi_{vs,\%}$	Fraction of evaporated mass at the surface	[—]
Δ	Cycle period	[s]
δ_{delay}	Delay of the exhaust	[s]
δ_{eEGR}	Delay of the external EGR	[s]
δ_{exh}	Exhaust delay	[s]
δ_{IGnat}	Natural delay	[s]
δ_{TE}	Timing error	[s]
δ_{WF}	Thickness of the fuel film	[m]
κ	Isentropic exponent	[—]
Λ	Observability matrix	[—]
λ, β	Characteristics	[—]
λ_w	Desired A/F ratio in the cylinder	[—]
μ	Dynamic viscosity	$[\frac{\text{kg}}{\text{m}\cdot\text{s}}]$
ν	Kinematic viscosity	$[\frac{\text{m}^2}{\text{s}}]$
Φ	Discrete state matrix	[—]

List of Symbols

Ψ	Throttle function	[—]
ρ_l	Liquid density	$[\frac{\text{kg}}{\text{m}^3}]$
ρ_v	Vapor density	$[\frac{\text{kg}}{\text{m}^3}]$
Σ	Covariance matrix	[—]
σ_0	Stoichiometric factor	[—]
τ_{DA}	Droplets exponential decrease rate	[s]
τ_{EV}	Wall wetting evaporation parameter by Aquino	[—]
τ_{mix}	Exhaust gas mixing time constant	[s]
τ_s	Shear stress	$[\frac{\text{N}}{\text{m}^2}]$
ξ_y	Fraction of fuel on the intake valve	[—]

Latin Symbols

\bar{x}	Propagated state variable	[—]
\hat{x}	Estimated state variable	[—]
A_f	NO reduction fraction	[—]
C	Residual gas fraction	[—]
$\text{Tay}(x)$	Taylor approximation	[—]
A, B, C, D	System matrices	[—]
A_D	Droplets surface	$[\text{m}^2]$
A_F	Fluid surface	$[\text{m}^2]$

List of Symbols

A_P	Wall wetting evaporation parameter by Simons and Aquino	[—]
A_s	Intake valve seat area	[m ²]
$A_{Th,bypass}$	Throttle bypass area	[m ²]
A_{Th}	Throttle area	[m ²]
B	Spalding number	[—]
B_P	Wall wetting impingement parameter by Aquino	[—]
c	Sound speed	[$\frac{m}{s}$]
C_1	Proportionality constant	[$\frac{kg}{m \cdot s}$]
C_2	Proportionality constant	[$\frac{m}{kg}$]
C_c	Combustion heat coefficient	[$\frac{m^2}{s^2}$]
C_p	Multiplicative factor	[—]
C_r, m_r, n_r	Parameter of the Reynolds analogy	[—]
C_s	Conduction heat coefficient	[$\frac{m}{s \cdot K}$]
C_A	Mass concentration	[$\frac{kg}{m^3}$]
C_f	Friction factor	[—]
c_{pF}	Specific heat of the fuel	[$\frac{J}{kg \cdot K}$]
d_D	Droplet diameter	[m]
D_{AB}	Binary diffusion coefficient	[$\frac{m^2}{s}$]
d_{in}	Internal diameter of the duct	[m]

List of Symbols

d_{WF}	Internal diameter of the fuel film	[m]
E_i	Internal energy	[J]
f	Friction coefficient	[—]
$G(s)$	Continuous-time transfer function	[—]
$G(z)$	Discrete-time transfer function	[—]
h_m	Convection mass transfer coefficient	[$\frac{m}{s}$]
h_q	Heat transfer coefficient	[$\frac{W}{m^2 \cdot K}$]
h_{WF}	Height of the fuel film	[m]
K	Kalman gain	[—]
k_q	Thermal conductivity	[$\frac{W}{m \cdot K}$]
K_{fill}	Filling coefficient	[—]
k_s	Heat conductivity of the intake valve seat	[$\frac{W}{m \cdot K}$]
L_d	Reference length	[m]
m_c	Characteristic of velocity profile type	[—]
M_{NO}	Molar mass of NO	[$\frac{kg}{mol}$]
m_{EGtot}	Total mass of gas that exits from the cylinder	[kg]
m_{EVD}	Evaporated mass of the droplets	[kg]
m_{EVF}	Evaporated mass of the fuel film	[kg]
$m_{F cyl_w}$	Desired fuel mass in the cylinder	[kg]
$m_{F inj}$	Injected fuel mass	[kg]

List of Symbols

m_{MTOF}	Total gas mass involved in the mixing in the exhaust	[kg]
m_{WF}	Fuel film mass	[kg]
N_{tot}	Droplets quantity	[-]
Nu	Nusselt number	[-]
p_R	Stagnation pressure	[Pa]
p_{EG}	Exhaust pressure	[Pa]
p_{Icorr}	Corrected cylinder pressure	[Pa]
p_{vs0}	Tuning factor	[Pa]
p_{vs}	Saturation pressure	[Pa]
Q, R	Noise covariance matrices	[-]
R	Gas constant	$[\frac{\text{J}}{\text{kg}\cdot\text{K}}]$
R_F	Fuel gas constant	$[\frac{\text{J}}{\text{kg}\cdot\text{K}}]$
r_{in}	Internal radius of the duct	[m]
Re	Reynolds number	[-]
s_I	Correction coefficient	[-]
Sc	Schmidt number	[-]
Sh	Sherwood number	[-]
svc	Tuning factor	[K]
T_R	Stagnation temperature	[K]
T_s	Sample time	[s]

List of Symbols

T_{Ad}	Temperature of the intake duct	[K]
T_{Av}	Temperature of the air-fuel mixture leaving the intake valve duct	[K]
T_{cool}	Coolant temperature	[K]
t_{fin}	Reference time	[s]
t_{fin}	Reference time	[s]
T_F	Fuel temperature	[K]
T_I	Intake manifold temperature	[K]
T_v	Intake valve temperature	[K]
U	Overall heat transfer coefficient	$[\frac{W}{m^2 \cdot K}]$
u	Gas flow speed	$[\frac{m}{s}]$
u_∞	Flow velocity	$[\frac{m}{s}]$
v, r	White noise	[—]
V_A	Exhaust volume between cylinder and sensor	$[m^3]$
V_{cyl}	Volume of the cylinder	$[m^3]$
$v_{D\infty}$	Speed of the droplets	$[\frac{m}{s}]$
V_D	Droplets volume	$[m^3]$
v_{Flow}	Speed of the waves in the duct	$[\frac{m}{s}]$
v_{inj}	Speed of injected fuel	$[\frac{m}{s}]$
V_I	Intake manifold volume	$[m^3]$

List of Symbols

V_{WF}	Fuel film volume	$[\text{m}^3]$
w	Perturbation speed	$[\frac{\text{m}}{\text{s}}]$
$x(t)$	State variable	$[-]$
x_c	Combustion heat coefficient	$[-]$
y_I	Correction coefficient	$[\text{Pa}]$
z_E	Total number of cylinders	$[-]$
z_I	Number of investigated cylinders	$[-]$
\dot{H}_i	Enthalpy fluxes	$[\text{W}]$
\dot{m}_{EG}	Exhaust mass flow	$[\frac{\text{kg}}{\text{s}}]$
\dot{m}_{EVD}	Evaporation rate of the droplet	$[\frac{\text{kg}}{\text{s}}]$
\dot{m}_{EVF}	Evaporation rate of the fuel film	$[\frac{\text{kg}}{\text{s}}]$
\dot{N}_A	Molar flux	$[\frac{\text{kmol}}{\text{s}}]$
\dot{q}	Heat flux per unit of area	$[\frac{\text{W}}{\text{m}^2}]$
\dot{Q}_c	Combustion heat flux	$[\text{W}]$
\dot{Q}_d	Heat transfer to the air by the cooling medium	$[\text{W}]$
\dot{Q}_s	Duct conduction heat flux	$[\text{W}]$
\dot{Q}_{Av}	Convective heat flux	$[\text{W}]$
\dot{Q}_{bf}	Overlap heat flux	$[\text{W}]$
\dot{Q}_{Fv}	Spray cooling heat flux	$[\text{W}]$

List of Symbols

\dot{Q}_g	Valve conduction heat flux	[W]
\dot{V}_{EG}	Exhaust volume flow	$[\frac{\text{m}^3}{\text{s}}]$
E	External EGR dilution	[-]

Used Acronyms

A/F	Air to fuel ratio	[-]
ECU	Engine management CPU	
EGR	Exhaust gas recycling	
EKF	Extended Kalman filter	
gTDC	Top dead center of the gas exchange stroke	
iTDC	Top dead center of the ignition stroke	
LPV	Linear parameter varying	
PFI	Port fuel injected	
SI	Spark ignited	
ZOH	Zero order hold	

List of Symbols

1. Introduction

1.1. Motivation

In the last decade, the technical evolution of the combustion engines has reached an high level of growth. This evolution was surely triggered by the restrictions imposed by the governments for the emission levels. The direct consequence of this improvement is an increase in the complexity of the engine management systems. This complexity results in a large number of parameters to be tuned, with the consequence that the time spent on the test bench became an important cost factor. To optimize the process, the existing parametrization methods have to be refined. For example, parametrical models based on physical understanding of the system can dramatically reduce the time spent measuring on the test bench and so the costs. The utilization of these models can also improve the design of the solution for the control problems.

The major control problem for the reduction of the emissions in the port injected spark ignited engines lies in the preparation of the air-fuel mixture, in particular with the introduction of the three-way catalytic converters, whose working principle requires the air-to-fuel ratio (A/F) to be maintained within narrow bounds.

In order to obtain the desired A/F ratio, the engine management system has to compensate all the disturbances caused by the dy-

1. Introduction

namics that are involved. The main dynamics that play a role are the air filling dynamics of the intake manifold, the wall wetting dynamics, and the exhaust gas dynamics. The feed-forward compensation of these effects supports the feed-back control of the A/F ratio in the exhaust manifold. In fact, although the feed-back control plays an important role, the feed-forward systems (compensators) cannot be completely eliminated. This is because the feed-back systems can react only once an error is measured, whereas the feed-forward systems try to avoid the error before it is generated. However, a wrong or an insufficient compensation may disturb the work of the controller and hence lead to a remarkable loss in driveability and consequently to an augmented emission level [32](HC, CO and NO_x).

The wall wetting dynamics play a particular role among these disturbances. The fuel injection in the intake manifold has to be performed the latest possible to minimize the delay between the estimation of the filling air mass and the calculation of the quantity of the fuel to be injected. The consequence of this fact is that the fuel does not have enough time to evaporate, and therefore it deposits on the manifold walls, building a wall film which evaporates slowly. Moreover, it should not occur too late, otherwise the injected fuel would reach the cylinder without proper evaporation, causing an increased emission of HC.

At steady-state engine conditions, i.e., when the evaporation rate equals the wall wetting rate, the fuel film reaches a constant mass. As soon as the state of equilibrium is disturbed, e.g., by a change in the throttle position or in the engine speed, the conditions for the evaporation change so that a dynamic correction of the fuel to be injected is necessary. Due to the fact that the evaporation rate, the wetting rate and the point of equilibrium are strongly dependent on the operating condition, the parametrization of a wall wetting compensator is not easy. To cope with the complex-

ity of this task a model of the system based on physics is thus needed.

The model has two different requirements: First, it has to be as simple as possible to permit the utilization in a controller. Second, it should be sensible to all the relevant physical phenomena in order to be as flexible as possible. Figure 1.1 shows the current two main model philosophies and the desired trade-off.

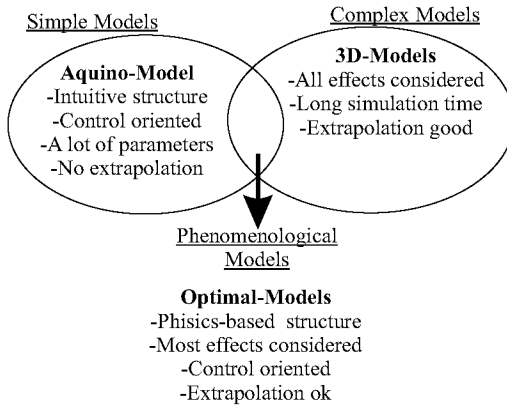


Figure 1.1: Modeling approaches for the wall wetting dynamics.

There exist several models in the group of complex models, while an example of a simple model is the Aquino model. Actually, the Aquino model reproduces the real structure of the wall wetting dynamics and it can be easily implemented into a commercial ECU. The negative aspect of the Aquino model is the quantity of necessary parameters for the tuning. Without including cold engine conditions, the Aquino model requires at least 40 parameters, and the capability to extrapolate to non-measured operating conditions is low.

1. Introduction

1.2. Strategy and Structure of the Thesis

1.2.1. Strategy

The main topics of this thesis are the investigation of the structure of the wall wetting model, its behavior under warm engine conditions and during the warm-up phase, the methodology to parameterize the model efficiently on the test bench, and the methodology for the development of an optimal wall wetting compensator.

Although the exhaust gases are usually measured after the conjunction of various cylinders, the experiments were conducted on the wall wetting of a single cylinder. This was preferred in order to avoid cross-effects between different cylinders that disturb a correct investigation. In fact, the result of this work can be easily applied to the whole engine by the aid of an additional model for the mixing between the exhaust gases of every cylinder.

The mixing path of a port-fuel-injected (PFI) engine is roughly depicted in Figure 1.2. The values that can be directly measured are the injected fuel mass m_{Finj} , the air mass m_{Ain} , and the air to fuel ratio in the exhaust λ_{out} . In order to isolate the effects of the wall wetting dynamics, models for the intake manifold and for the exhaust gas dynamics were developed and identified separately with specific methodologies.

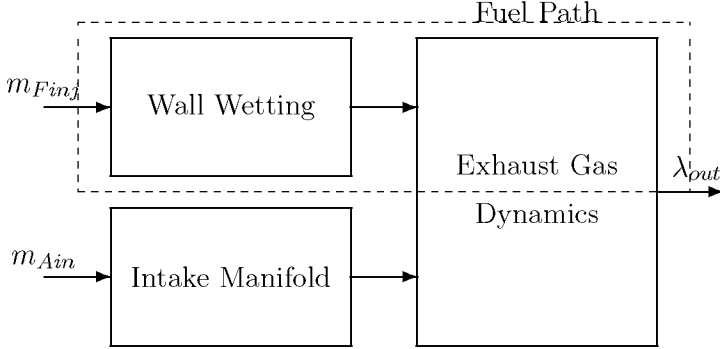


Figure 1.2: Signal flow diagram of the PFI engine mixing path.

The resulting new wall wetting model is then compared to the well-known linear model structure of Aquino [4] in its discrete form with the parameters identified in [58].

1.2.2. Structure of the Thesis

This thesis is structured into two main parts: The first part is introductory and is focused on the estimation of the systems upstream and downstream the wall wetting, namely the intake manifold dynamics and the exhaust gas dynamics. The second part is focused on the main topic of the thesis with the development of the model, the identification of the parameters, and finally the development of the compensator.

More in detail, Chapter 2 describes the engine and the test-bench which were used in this investigation. In this chapter an impor-

1. Introduction

tant point regarding the position of the sensor in the exhaust is discussed.

Chapter 3 introduces the systems upstream and downstream the wall wetting, i.e., the model that represents the systems between the wall wetting and the measurement of the A/F ratio in the exhaust.

In Chapter 4 both the development of the wall wetting model and the comparison between this model and the current models are presented.

Chapter 5 presents the methodology for the estimation of the model parameters, for the off-line and on-line identification. This chapter introduces the relevant parameters which will be used in Chapter 6 for the development of the enhanced wall wetting compensator.

In Chapter 7 the thesis is closed with the conclusive remarks.

2. Experimental Conditions

This chapter presents the test bench and the measurement facilities that were used for this investigation. The first section summarily describes the hardware part of the test bench, while the second section introduces the software that was specially developed for the test bench and experiment management (DSP-Motronic with ICX-3 interface). The last part of this chapter is focused on the research of the best position for the different sensors in the exhaust manifold.

2.1. Description of the Test Bench

The experiments were executed on a dynamic test bench equipped with an electric brake with 160 kW nominal power (BBC: GNW 225 S33-F). This brake permits to perform experiments with high bandwidth controlled engine speed. In fact, its dynamic properties avoid remarkable oscillations of the engine speed and permit to brake the engine at a defined speed and eventually to drag the engine.

The engine used is an Audi V6 port-fuel-injected engine. Its technical data are listed in Table 2.1.

2. Experimental Conditions

Table 2.1: Engine data.

Engine	Audi 2.8V6 30V
No. of cylinders [-]	6
Displacement [cm ³]	2771
Arrangement of the cylinders	V
Bore [mm]	82.5
Stroke [mm]	86.4
Compression ratio [-]	10.6
Valves per cylinder [-]	5
Maximum torque [Nm] / [rpm]	280 / 3200
Output power [kW] / [rpm]	142 / 6000
Opening intake valves [°crank] early - late	350 - 372
Closing intake valves [°crank] early - late	560 - 582
Opening exhaust valves [°crank]	142
Closing exhaust valves [°crank]	352

This engine normally has a very short exhaust manifold upstream the first catalytic converter. This is meant to optimize the space in the car and to warm-up the catalytic converter as quickly as possible. Due to its “V” characteristic, the engine has two banks of three cylinders each. The exhaust flows from each bank are connected very near to the exhaust valves, thus mixing the exhaust gases of the cylinders before the measurement of the A/F ratio. This geometry is not optimal for this investigation, so a special manifold was built and placed between the actual manifold and the engine block to solve this problem. This manifold can be spotted in Figure 2.1. The regular manifold can be seen downstream the custom-made manifold.

2.1. Description of the Test Bench

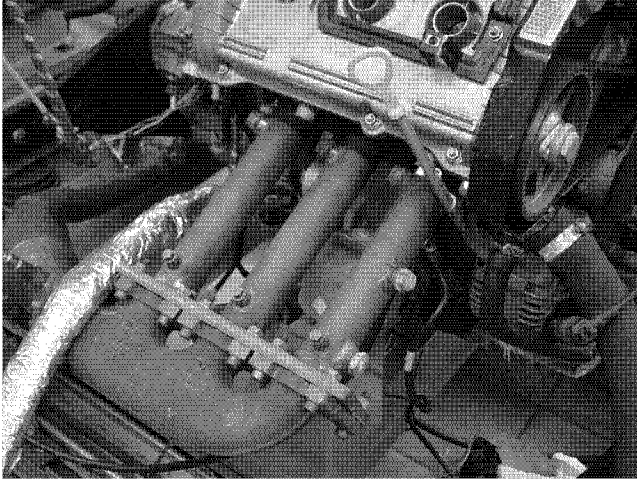


Figure 2.1: Modification of the exhaust manifold (three pipes placed between the engine block and the original manifold).

2. Experimental Conditions

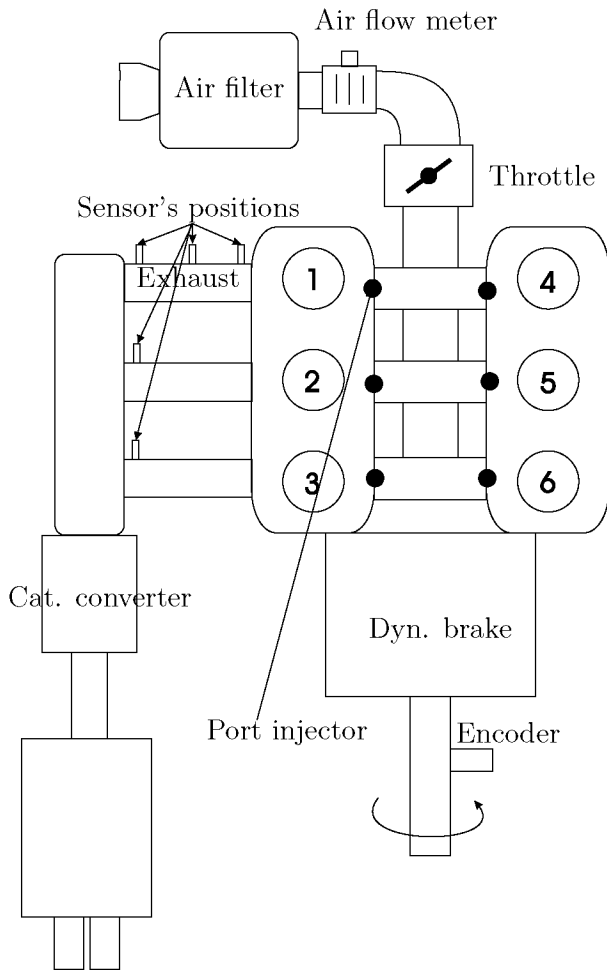


Figure 2.2: Engine setup.

2.1.1. DSP-Motronic and ICX-3

The software used on the test bench is mainly ControlDesk of the dSpace company [18]. The application running in the ControlDesk environment is the *DSP-Motronic*. The DSP-Motronic is a complete engine management system based on the concept of the ICX-chipset engine management [25, 48]. It was specifically developed for the operation on test benches by the author of this thesis and by Theo Auckenthaler.

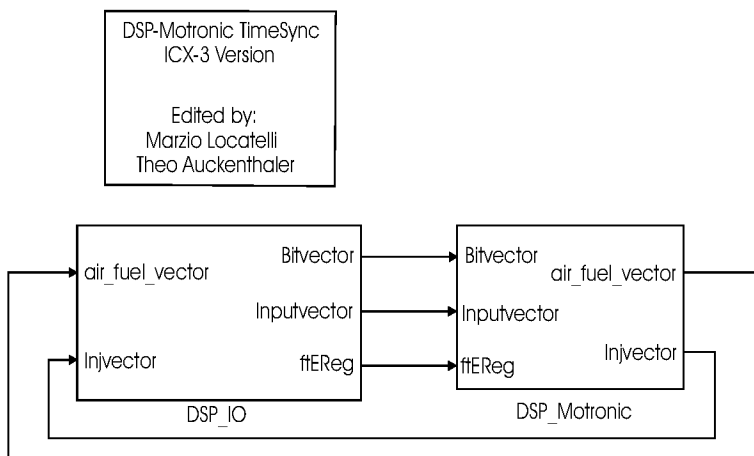


Figure 2.3: DSP-Motronic.

The software was developed almost entirely with Matlab-Simulink, with the sole exceptions of specific functions which are in *C*. The DSP-Motronic program is structured into two functional blocks. The first block (the DSP_IO-block in Figure 2.3) handles the communication with the sensors and the actuators of the whole test bench, while the second block, the DSP_Motronic

2. Experimental Conditions

block, contains the engine management software, such as the λ -controller, the idle-speed controller, ignition timing, etc.

Basically, the DSP_Motronic block is the core of the whole DSP-Motronic. In fact, the behavior of that block is totally independent from the hardware of the test bench, provided that all its necessary inputs are prepared and delivered by the IO-block. The hardware used to interface the DSP-Motronic with the engine is listed in Table 2.2.

Table 2.2: Hardware for the interface.

Type	Description	Maker
Industrial PC	SBC81821VE	Axiomtek
AD/DA card	DS2002 32in/out	dSpace [19]
AD/DA card	DS1103 20in/8out	dSpace [19]
Digital I/O card	DS4003 32in/out	dSpace [19]
Real-time processor card	DS1005 PPC	dSpace [19]
Incremental encoder	ROD-426 3600	Heidenhain
Engine-PC interface	ICX-3	IMRT [48]

All this hardware can be acquired on the market with the exclusion of the ICX-3 chip-set. In fact, the print of the ICX-3 circuit was developed in the laboratory of engine systems of the ETH (Figure 2.4). The concept of ICX was introduced in [25] and is depicted in Figure 2.5. The functions of the ICX-3 chip-set are intended to simplify the exchange of data between an engine, whose events are based on the position of the crankshaft (injection, ignition, etc.), and the time-based management hardware (normally a PC). The ICX-3 uses the signal of an incremental encoder to monitor the position of the crankshaft every 0.1° crank. It can handle different tasks at different crankshaft positions and mea-

2.1. Description of the Test Bench

sure the engine speed with an improved precision compared to the standard sensor.

The main advantage of this system, confronted to the existing systems, is the flexibility that it permits. Actually, the user has just to pre-set the starting time for the injection/ignition and the length of the event in [ms] or in [°crank] and the ICX-3 send the signal to the actuator at the right moment with the right duration.

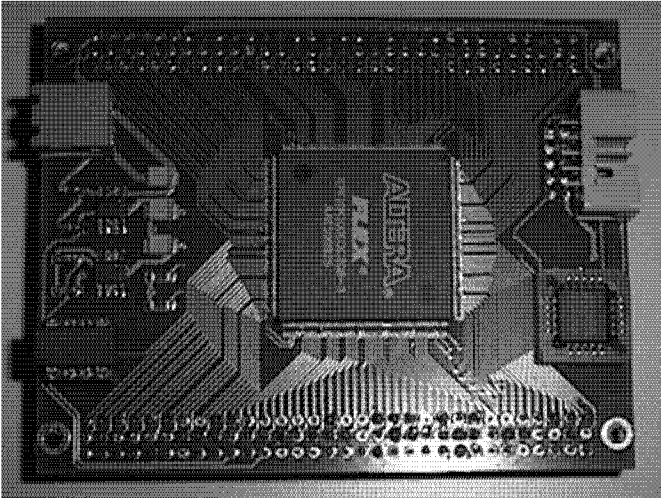


Figure 2.4: ICX-3 print layout.

2. Experimental Conditions

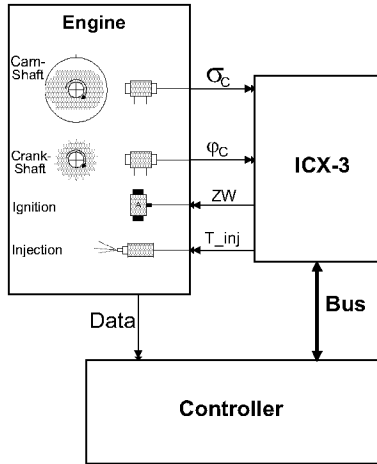


Figure 2.5: ICX-3 concept.

With this setup almost every possible experiment can be executed. All the sensor outputs are integrated, so that the acquisition of measurement data is straightforward. The compatibility between ControlDesk and Matlab permits to exchange these data seamlessly.

2.1.2. Description of the Sensors

Different types of sensor are needed for this investigation. Temperature and pressure sensors are necessary to model the systems of the intake, of the exhaust manifold, and obviously of the wall wetting system. To measure the exhaust gas composition, in other words the visible effects of the investigated systems, a fast NO sensor and a λ sensor are needed. The most important sensors are

2.1. Description of the Test Bench

listed in Table 2.3.

Table 2.3: Main sensors data.

Type	Pressure	Temp.	NOx	λ
Brand	Sensortechinics	Philips	Cambustion	Bosch
Name	BTE6002	PT100	fNO_x400	LSU 4
Range	0..2 bar	0..1200 °C	0..10 ⁶ ppm	0.7..1.6
T90%	1 ms	< 1 min	4 ms	≈ 20 ms
Delay	-	-	8 ms	-
Accuracy	± 0.01 %	± 0.5 °C	± 1 %	± 1.5 %

In order to place the sensors in the optimal position so that measurement problems due to gas oscillations in the exhaust could be avoided, an investigation of the fluxes in the exhaust manifold was necessary. This addresses particularly to the investigation of the exhaust gas dynamics.

2. *Experimental Conditions*

2.2. Adequate Sensors Position

The behavior of the exhaust gases has to be taken into account to place the sensors in the exhaust. As a matter of fact, an incorrect position leads to errors in the estimation of the exhaust dynamics, in particular if they are modeled with mean-value models. As a rule of thumb, the closer the sensors sit to the exhaust valve, the smaller is the eventual error. If the sensor sits near enough, the error is not present.

This section is focused on a quantification for the expression near enough in the investigated engine with the modified exhaust manifold (see Figure 2.1). The method used is the standard method for the calculation of the waves in the exhaust, namely the method of characteristics. Due to the fact that the procedure is not the main topic of this thesis, the methods will be presented in a very concise form, more details can be found in [10].

The results of this study were indeed interesting and gave an indication about the critical positioning of the sensor.

2.2.1. Method of Characteristics

The method of characteristics is the first mathematical method for the resolution of hyperbolic partial differential equations. Its application to the exhaust waves was introduced by R. S. Benson [10].

To simplify the calculation a reference state (index $_0$) was defined and isentropic reaction were assumed unless necessary. The

2.2. Adequate Sensors Position

stagnation condition of an ideal gas can be defined:

$$\begin{aligned} p_R &= p \cdot \left[1 + \frac{\kappa - 1}{2} \left(\frac{u}{c} \right)^2 \right]^{\kappa/(\kappa-1)} \\ T_R &= T \cdot \left[1 + \frac{\kappa - 1}{2} \left(\frac{u}{c} \right)^2 \right], \end{aligned} \quad (2.1)$$

where with stagnation conditions are meant the conditions that would rule for the gas, if it reduced its actual speed isentropically to null. In this equation c is the sound speed and u is the gas speed. The gas speed u can be defined as:

$$u = \pm \frac{2 \cdot c_0}{\kappa - 1} \left[\left(\frac{p}{p_0} \right)^{(\kappa-1)/2\kappa} - 1 \right], \quad (2.2)$$

where the sign distinguish the waves traveling upstream (-) or downstream (+). The sound speed is calculated with:

$$c = \sqrt{\kappa \cdot R \cdot T}. \quad (2.3)$$

The speed of the perturbation in the tube is:

$$w = u \pm c. \quad (2.4)$$

The method of characteristics says that along a perturbation (Equation (2.4)) the following equation rules:

$$u \pm \frac{2c}{\kappa - 1} = \text{const.} \quad (2.5)$$

These constants, P for $w = u + c$ and N for $w = u - c$, are called characteristics. The constant value on the right hand side of Equation 2.5 is called λ for the perturbation P and β for the perturbation N .

The evolution in time of λ and β at a specific distance x from the source (e.g., the exhaust valves) is then dependent on the conditions that rule upstream and downstream of it.

2. Experimental Conditions

Boundary Conditions

For this method there are two types of boundary conditions: The tube in which the waves travel can be close-end or open-end. The main difference in those conditions lies in the nature of the waves that are generated when a shock wave reaches the bounds. In fact, a wave that reaches an open-end generates an expansion wave which travels in the opposite direction, thus increasing the purge effect. If a wave reaches a close-end, a compression wave which travels the opposite direction is generated. This wave behaves like the expansion wave but reducing the purge effect.

The same wave generations can be observed when the diameter of the tube changes. If the tube enlarges, infinitesimally it is as if the gas would reach an open-end, whereas if the tube tightens it is as if the gas reaches a close-end. This means that in the first case expansion waves and in the second case compression waves are generated. A small scheme of the behavior of the waves is depicted in Figure 2.6.

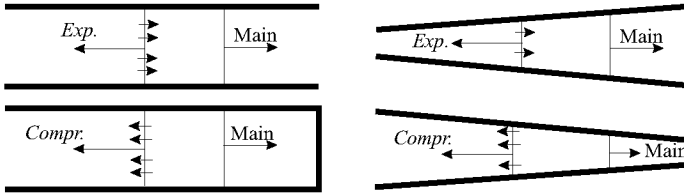


Figure 2.6: Waves in a tube.

The waves in the tube are triggered by a pressure shock, which in our case is caused by the opening of the exhaust valves. While the valves are opened, the cylinder is part of the system and therefore its internal pressure is disturbed by the behavior in the exhaust.

2.2. Adequate Sensors Position

The boundary condition by the cylinder can thus be modeled as an open-end tube where the pressure outside the tube is calculated with the gas equation and the cylinder volume. While the exhaust valves are closed, the boundary condition by the cylinder can be modeled as a close-end tube. The boundary condition at the exit of the exhaust is obviously modeled as an open-end tube. Particular attention must be paid by the modeling of the valves and by the modeling of the pressure in the cylinder.

Due to the fact that our exhaust pipe intersects with two other cylinder, special boundary conditions have to be used. Basically, they can be assumed as an open-end tube with variable boundary pressure [10].

Validation of the Model

To validate the model three pressure sensors were mounted in the custom-made extension of the exhaust manifold at different distances from the valves (see Figure 2.1). The results depicted in Figures 2.7-2.9 show that this simple model is able to predict the behavior of the waves in the tube very well, in particular when the distance is minimal. The farther is the sensor, the more unprecise is the prediction. However, only the high-frequency waves are not replicated, while the main waves (responsible for the relevant changes in the trajectory of the exhaust particles) are replicated satisfactorily.

2. Experimental Conditions

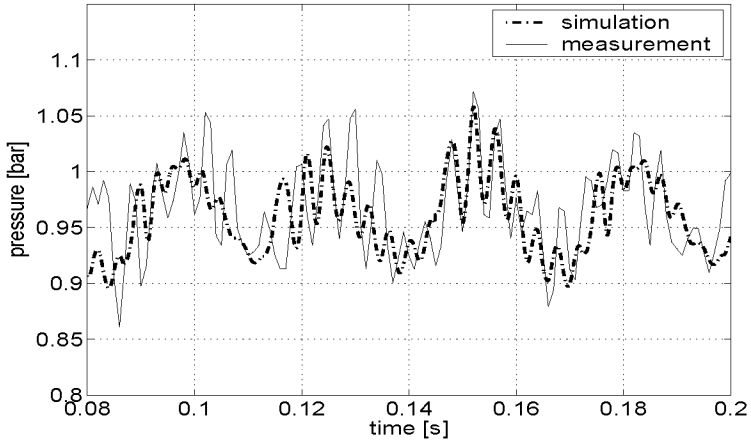


Figure 2.7: Results of the method of characteristics for 1500 rpm, 5 cm downstream the exhaust valves.

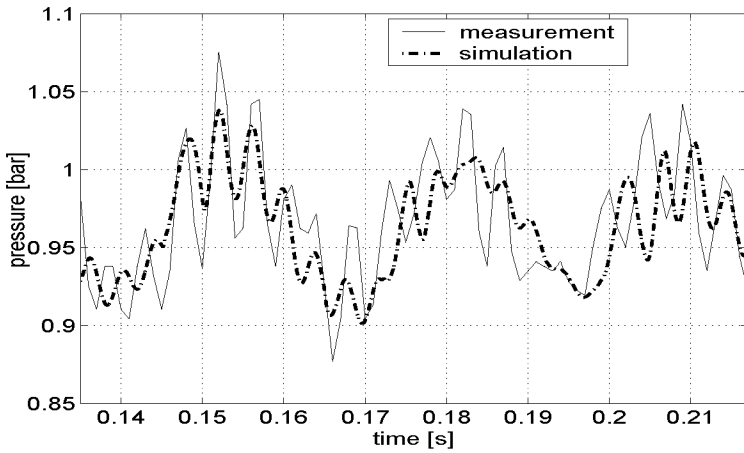


Figure 2.8: Results of the method of characteristics for 1500 rpm, 15 cm downstream the exhaust valves.

2.2. Adequate Sensors Position

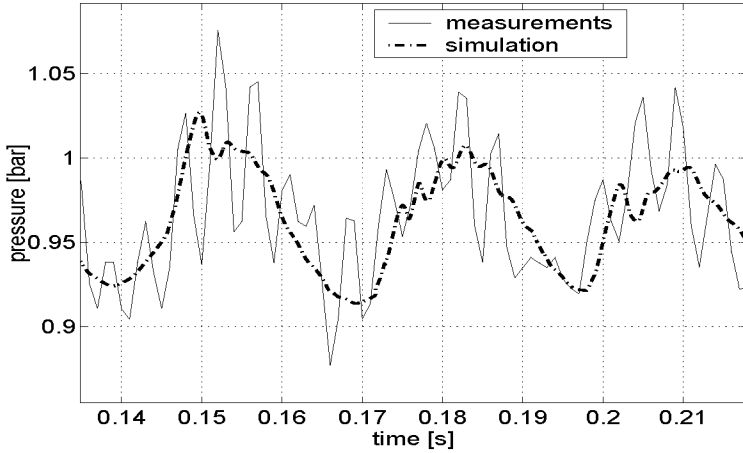


Figure 2.9: Results of the method of characteristics for 1500 rpm, 30 cm downstream the exhaust valves.

The method of characteristics is not only able to predict the pressure in each exhaust spot at every instant but also the velocity of the gas flow. The different velocities for the same air mass in the cylinder are depicted in Figure 2.10. The negative sign means that the flow goes from the valves to the ambient. A positive mass flow here would mean a back-flow of exhaust gas into the cylinder. In these experiments this was never the case.

2. Experimental Conditions

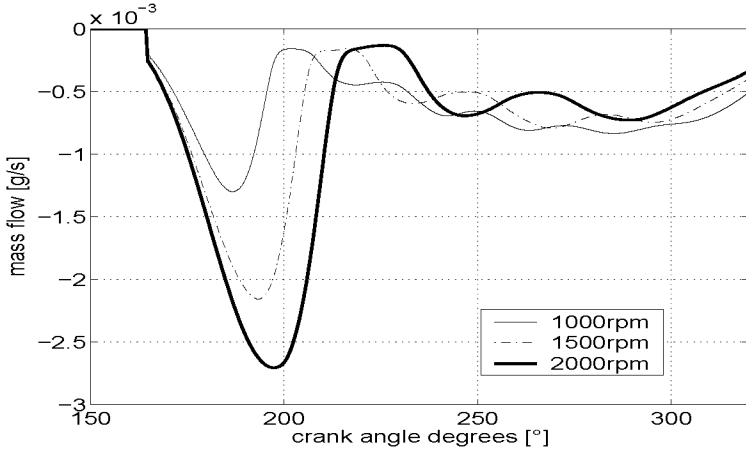


Figure 2.10: Exhaust mass flow near the exhaust valves (0.2 g/-cyl).

Now that this tool is available, the exhaust particles can be followed along the tube to estimate their trajectory and check whether a single particle can be measured twice or more. The methodology used is called *Particle tracking*.

Particle Tracking

The gas motion along the pipe is calculated integrating the flow velocities that a specific particle encounters along the duct. The position of the particle at the time t_k is calculated as:

$$x(t_k) = u(x(t_{k-1}), t_{k-1}) \cdot (t_k - t_{k-1}). \quad (2.6)$$

The results show that in some duct sections the particle moves with small oscillations during the time when the exhaust valves

2.2. Adequate Sensors Position

are closed. At the valves opening the gas has an high velocity, due to the pressure difference between upstream and downstream the valve. In Figure 2.11 the behavior of the first particle that exits the cylinder is depicted.

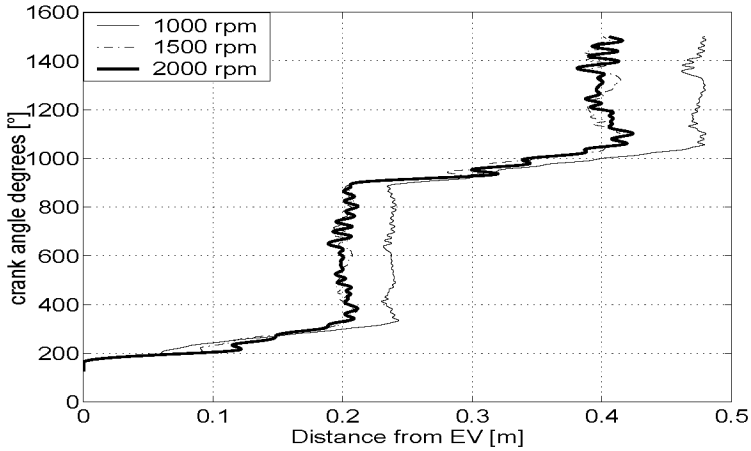


Figure 2.11: Particle tracking for 0.2 g/cyl.

While the exhaust valves are closed, a certain stall of the particle can be observed. This is expected because the waves lose their excitation source and their energy is gradually adsorbed.

The suspect that some particles can be measured twice or more grows during this stall. A closer look at the stall zone reveals the expected problem, in particular for 2000 rpm (Figure 2.12). The particle has an “S”-shaped trajectory, which means that it travels in front of an infelicitous place three times.

2. Experimental Conditions

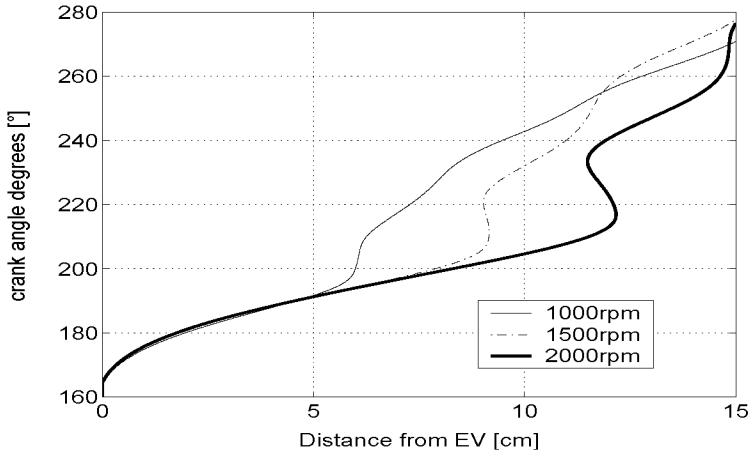


Figure 2.12: Particle tracking for 0.2 g/cyl.

A second observation that can be made is that the higher the engine speed, the more space the particle travels smoothly. However, the trajectory in the critical point is much more disturbed, causing a back-flow. This can be explained by looking at Figure 2.10. For higher engine speed the velocity of the flow is much bigger than for lower engine speed, thus producing more energetic reflected waves. For a load lower than 0.2 g/cyl the behavior of the particle tends to be more “healthy”, because the pressure difference between cylinder and exhaust is smaller, thus generating weaker shock waves, but disturbing the trajectory nearer to the exhaust valves. The distance of the critical point from the exhaust valves is listed for reference in Table 2.4.

2.2. Adequate Sensors Position

Table 2.4: Critical point where the flow is disturbed (1000 rpm).

Air mass in cylinder	0.1 g/cyl	0.2 g/cyl	0.3 g/cyl
Distance critical point	≈ 5 cm	≈ 6 cm	≈ 8 cm

At 1000 rpm and 0.1 g/cyl the critical point is unproblematic, because the disturbance in the trajectory is minimal and it does not cause any “S”-effect.

2. *Experimental Conditions*

2.3. Discussion

The goal of this task was to determine whether measurement problems could occur in the nearest possible mounting point of the test bench setup (≈ 5 cm). The results show that problems can occur at low loads and low engine speed, however their influence is negligible with the chosen mounting point of the sensors. The most important remark is that at the chosen mounting point the feared “S”-effect does not occur. Moreover, the particles fly with the same speed at least up to the place where they are measured, allowing the use of linear approximations for the delay between opening of the exhaust valves and measurements (Chapter 3). For the problematic operating points (low engine speed, low load) this approximation may lead to an underestimation of the discussed delay.

3. Dynamics Adjacent to the Wall Wetting

3.1. Introduction

Usually, during transients such as throttle opening and closing, gear change, etc., the control of the A/F ratio is disturbed by following dynamic phenomena:

- The air mass that flows into the cylinder is not directly measured but, because of the intake manifold dynamics, it can be only estimated. Additionally, some residual air may be already present in the cylinder (residual gas fraction).
- The gas that is in the cylinder (air + fuel) is not directly measured, but only in the exhaust. Because of the exhaust mixing dynamics its value has to be estimated. If the gas is measured near to the exhaust valves, the importance of these dynamics is reduced. A big influence will be expected if the sensors are placed downstream a connection of various exhaust ducts.
- The injected fuel mass does not flow directly into the cylinder, but partially impinges on the wall of the intake manifold.

3. *Dynamics Adjacent to the Wall Wetting*

- The fuel mass to be injected can be calculated on the basis of an estimate of the air mass flow, because it has to happen before the opening of the intake valves (timing error).

Because of these dynamics, the quantity of fuel to inject during transients cannot be known precisely and has to be estimated.

This chapter copes with the problems caused by the first two items in the list, the third dynamics is treated in Chapter 4, and the last item is treated in Chapter 6.

In the first section, a state-of-the-art intake manifold model is presented.

In the second section, the exhaust gas dynamics is investigated. The second section includes a presentation of the measurement setup, a description of the involved processes, a mathematical formulation of the exhaust gas dynamics, and the resulting parameters of the identification.

3.2. Intake Manifold Model

The model for the intake manifold which is used in this thesis is the usual, state-of-the-art model, based on a mass balance on the intake manifold (see [26])

$$\frac{dm_{AI}}{dt} = \dot{m}_{Ain} - \dot{m}_{Aout}. \quad (3.1)$$

Equation 3.1 can be written as a function of the intake pressure:

$$\frac{dp_I}{dt} = \frac{R_A \cdot T_I}{V_I} \cdot (\dot{m}_{Ain} - \dot{m}_{Aout}), \quad (3.2)$$

where T_I stands for intake temperature and V_I stands for intake volume. The temperature T_I is constant (≈ 315 K).

The value of \dot{m}_{Ain} is obtained from the throttle angle (α_{Th}), the manifold pressure (p_I), and the environmental conditions (p_U , T_U):

$$\dot{m}_{Ain} = A_{Th}(\alpha_{Th}) \cdot \frac{p_U}{\sqrt{R_A \cdot T_U}} \cdot \Psi \left(\frac{p_I}{p_U} \right), \quad (3.3)$$

where A_{Th} stands for the opened area of the throttle. This area is given by:

$$A_{Th}(\alpha_{Th}) = \pi \cdot \frac{d_{Th}^2}{4} \cdot \left(1 - \frac{\cos(\alpha_{Th})}{\cos(\alpha_{Th,0})} \right) + A_{Th,bypass}. \quad (3.4)$$

The value of $\alpha_{Th,0}$ stands for the residual angle of the closed throttle and $A_{Th,bypass}$ stands for the bypass area of the throttle [64, pp. 47-48]. Ψ stands for the throttle function [6]:

$$\Psi = \begin{cases} \sqrt{\frac{2\kappa}{\kappa-1} \cdot \left[\left(\frac{p_I}{p_U} \right)^{2/\kappa} - \left(\frac{p_I}{p_U} \right)^{\frac{\kappa+1}{\kappa}} \right]} & \frac{p_I}{p_U} \geq \left(\frac{2}{\kappa+1} \right)^{\frac{\kappa}{\kappa-1}} \\ \sqrt{\kappa \cdot \left(\frac{2}{\kappa+1} \right)^{\frac{\kappa+1}{\kappa-1}}} & \frac{p_I}{p_U} < \left(\frac{2}{\kappa+1} \right)^{\frac{\kappa}{\kappa-1}} \end{cases}. \quad (3.5)$$

3. Dynamics Adjacent to the Wall Wetting

The value of \dot{m}_{Aout} depends on various factors, in particular the engine speed n and the intake manifold pressure p_I :

$$\dot{m}_{Aout} = \frac{z_E}{2} \cdot \frac{n}{60} \cdot m_{Acyl,ideal}. \quad (3.6)$$

The value for the ideal air mass into the cylinder $m_{Acyl,ideal}$ is yielded by the standard gas equation under the assumptions that the same conditions of the intake manifold rule in the cylinder at the bottom dead center (BDC) [30]:

$$m_{Acyl,ideal} = K_{fill} \cdot \frac{V_{cyl} \cdot p_I}{R_A \cdot T_I}. \quad (3.7)$$

The filling efficiency of the engine is described by the value of K_{fill} which can be described as a function of the intake pressure p_I and of the engine speed n . Another expression for $m_{Acyl,ideal}$ is given by correcting the cylinder pressure as shown in [6]:

$$m_{Acyl,ideal} = \underbrace{[s_I(n) \cdot p_I + y_I(n)]}_{p_{Icorr}} \cdot \frac{V_{cyl}}{R_A \cdot T_I}, \quad (3.8)$$

where the parameters $s_I(n)$ and $y_I(n)$ have to be identified. The investigation on the engine yielded the results depicted in Figure 3.1 and Figure 3.2.

3.2. Intake Manifold Model

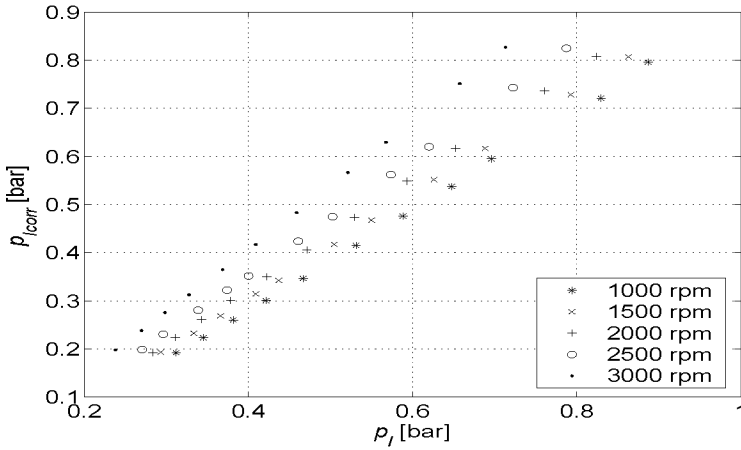


Figure 3.1: Corrected cylinder pressure p_{Icorr} [bar].

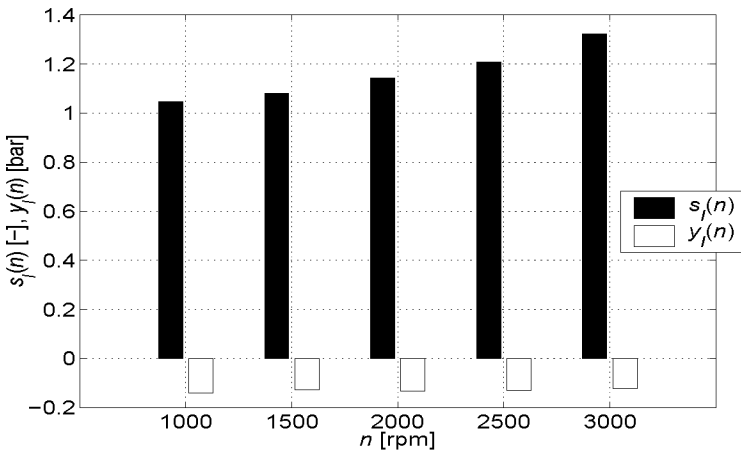


Figure 3.2: Values for the parameters $s_I(n)$ [-] and $y_I(n)$ [bar].

3. Dynamics Adjacent to the Wall Wetting

Figure 3.2 shows that only the parameter $s_I(n)$ actually depends on the engine speed. The parameter $y_I(n)$ can be considered as constant and it has the value:

$$y_I(n) = y_I = -13.1 \text{ kPa.} \quad (3.9)$$

Moreover, the dependency of $s_I(n)$ shows a quadratic behavior, which can be expressed as:

$$s_I(n) = s_I(1) \cdot n^2 + s_I(2) \cdot n + s_I(3), \quad (3.10)$$

with

$$\begin{aligned} s_I(1) &= 3.44 \cdot 10^{-8} \text{ 1/rpm}^2 \\ s_I(2) &= -2.90 \cdot 10^{-5} \text{ 1/rpm} \\ s_I(3) &= 1.049 \text{ [-]}. \end{aligned} \quad (3.11)$$

The intake manifold volume V_I can be estimated by exciting the intake system by opening and closing the throttle and confronting the measured pressure with the model (Figure 3.3). The resulting volume for the investigated engine is:

$$V_I = 6.3 \text{ dm}^3 \quad (3.12)$$

3.2. Intake Manifold Model

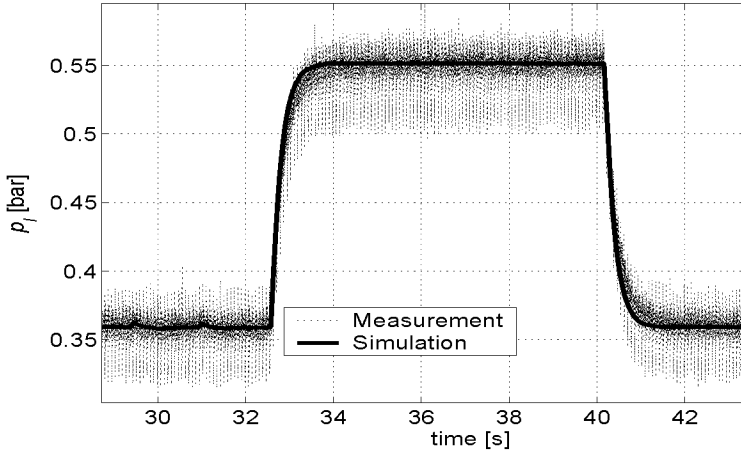


Figure 3.3: Intake manifold pressure [bar].

The estimation of the air mass flow into the cylinder is very important for the study of the wall wetting; the procedure described in the rest of this work is based on a good knowledge of this quantity. A successful estimation of the air mass flow into cylinder solves more than 50% of the whole fuel injection compensation.

3.3. Estimation of the Exhaust Gas Dynamics

3.3.1. Measurement Setup

The measurement setup is introduced by considering the time line of the cylinder's events for a single cylinder.

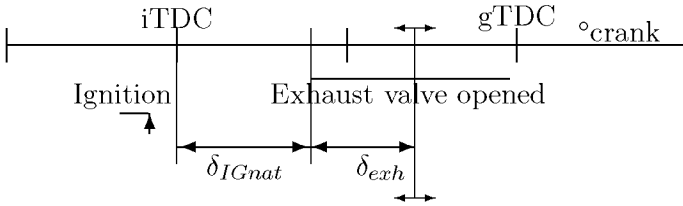


Figure 3.4: Time line of the ignition of the cylinder.

As explained in Chapter 2, the DSP-Motronic real-time engine management system can feed back the values of injection and ignition used for every cylinder. In addition to that, the timing when the signals are to be sent to the output channels (output-timing) can be decided. As a matter of fact, the natural delay between ignition and opening of the exhaust valves δ_{IGnat} , as depicted in Figure 3.4, could be eliminated by setting the output-timing to the opening of the exhaust valve. In this investigation however, the output-timing of the ignition is set to the ignition top dead center (iTDC). The delay between the iTDC and the opening of the exhaust valves (δ_{nat}) has to be added to the model of the

3.3. Estimation of the Exhaust Gas Dynamics

exhaust delay (δ_{exh}).

The ignition signal output is held up to its next value, reproducing a zero-order-hold behavior (ZOH), while the output signals (NO concentration and A/F ratio) are measured continuously in the exhaust pipe.

The method used for the identification is a frequency domain method based on the frequency response of the investigated system.

3.3.2. Models for the Elements of the Exhaust Gas Dynamics

The exhaust gas dynamics can be described by three dynamic elements in series [41, 58]. The first element of the system is the in-cylinder mixing which is a sampled system, because the intake and the exhaust valves open once per engine cycle. As a consequence, the following elements receive a new, constant input every new cycle (ZOH in Figure 3.5).

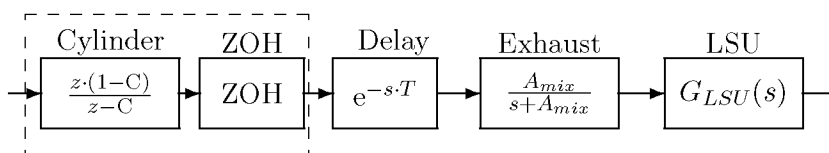


Figure 3.5: Exhaust-gas dynamic processes.

Downstream the in-cylinder mixing is a transport delay. The physical process it models is an uniform flow of the the new gas in the first part of the exhaust tube, pushed by the impulse of

3. Dynamics Adjacent to the Wall Wetting

the shock wave generated at the moment when the exhaust valve opens. As soon as the impulse loses its strength, the new gas mixes with the old gas. This effect is taken into account with the exhaust mixing element. Obviously, the sensor dynamics must be well-known (for example the λ sensor dynamics (LSU), which are usually described as a first order low-pass filter).

In-Cylinder Mixing

Idea: The burned gas mass does not exit completely from the cylinder by the exhaust valve's opening. One part remains in the cylinder and mixes with the incoming fresh gases. The gas composition in the cylinder at the current cycle k is the result of this mixing process. The cylinder is assumed as a container where the gases enter, mix, and exit. In the sampled system, at the cycle k the remaining gases of the cycle $k - 1$ mix with the incoming fresh gases and a part of them exit to the exhaust after being burned. The signal flow diagram of this system is depicted in Figure 3.6 and the transfer function is given in Equation 3.13.

3.3. Estimation of the Exhaust Gas Dynamics

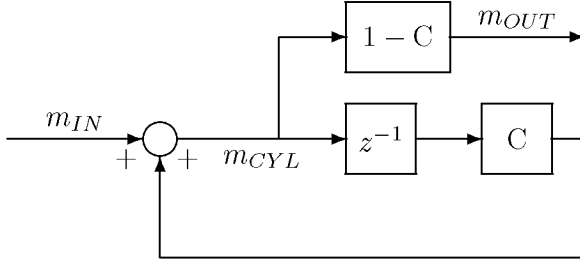


Figure 3.6: Signal flow diagram of the in-cylinder mixing.

$$m_{OUT}(k) = m_{IN}(k) \cdot \frac{z \cdot (1 - C)}{z - C}. \quad (3.13)$$

The parameter C expresses the part of gas that remains in the cylinder, i.e., the residual gas fraction. The value $C=0.2$ means that 20% of the burned gas remains in the cylinder and mixes with the incoming fresh gas. The variable z comes from the \mathcal{Z} -Transformation where $z = e^{j \cdot \omega \cdot T_s}$, where T_s is the sampling time of the system, namely the cycle time of the engine. For a four-stroke engine is given by $\frac{20 \cdot z_E}{n_{[\text{rpm}] \cdot z_I}$, where z_E is the number of cylinders of the engine and z_I is the number of cylinders involved in the investigation. For example, if we consider a single cylinder of a V6 cylinder engine we have $z_E = 6$ and $z_I = 1$, with a resulting sample time for the signals of $\frac{120}{n_{[\text{rpm}]}}$.

The residual gas fraction C is not constant over the operating range of the engine. The value of C mainly depends on the inlet and exhaust pressure, engine speed, compression ratio, valve timing, and exhaust system dynamics [49], but it depends negligibly

3. Dynamics Adjacent to the Wall Wetting

on the ignition spark-advance [30].

Transport Delay in the Exhaust Manifold

The delay in this system, clearly noticed in the measurements, is given partly by the natural delay described in Section 3.3.1 and partly by the incoming new gas that fills the volume between the exhaust valve and the λ -sensor.

The natural delay is described by crank degrees ($^{\circ}$ crank), and is thus dependent on the engine speed. For the investigated engine it can be calculated with:

$$\delta_{nat}[s] = \frac{142 \text{ }^{\circ}\text{crank}}{6 \cdot n \text{ [rpm]}}, \quad (3.14)$$

where the value of 142 $^{\circ}$ crank is given for the investigated engine (see Table 2.1). The volume in the exhaust to be filled will be described as V_A . Assuming that the gas flows uniformly at a constant volume flow \dot{V}_{EG} , the volume V_A will be filled in δ_{exh} seconds:

$$\delta_{exh} = \frac{V_A}{\dot{V}_{EG}}. \quad (3.15)$$

The volume flow \dot{V}_{EG} can be expressed in dependency of the mass flow \dot{m}_{EG} by the standard gas equation and substituted in Equation 3.15 yielding:

$$\dot{m}_{EG} \cdot \delta_{exh} = \frac{p_{EG} \cdot V_A}{R_{EG} \cdot T_{EG}}. \quad (3.16)$$

In Equation 3.16 it is assumed, that the air mass flow \dot{m}_{EG} is constant during the engine cycle. Actually, \dot{m}_{EG} varies from quasi still to very high during the opening period of the exhaust valves.

3.3. Estimation of the Exhaust Gas Dynamics

However the process is approximated with the mean value:

$$\dot{m}_{EG} = \frac{n \cdot m_{EGtot}}{120}, \quad (3.17)$$

where m_{EGTOT} is the total mass of gas that exits from the cylinder. Usually, m_{EGTOT} can be expressed in function of m_A and λ :

$$m_{EGtot} = m_{EGtot}(k) = m_A(k) \cdot \left(1 + \frac{\sigma_0}{\lambda(k)}\right). \quad (3.18)$$

Utilizing Equations 3.16 and 3.18 with some unit adjustments, the final expression for the exhaust delay is:

$$\delta_{exh}[s] = \frac{p_{EG} \cdot V_A \cdot 120000}{m_A \cdot n \cdot \left(1 + \frac{\sigma_0}{\lambda}\right) \cdot R \cdot T_{EG}}. \quad (3.19)$$

In this investigation, the value of δ_{exh} lies in the milliseconds range. According to Figure 3.4 the total delay is:

$$\delta_{delay} = \delta_{mat} + \delta_{exh} \quad (3.20)$$

Exhaust Mixing

If the volume between exhaust valves and λ -sensor is too large, the shock wave cannot push the old gas strongly enough to avoid mixing. The mathematical expression for the mixing is derived from a mass balance equation:

$$\frac{dm_{EGexh}}{dt} = \dot{m}_{EG} - \dot{m}_{EGout}. \quad (3.21)$$

Expressed by λ with $m_{(A+F)} = m_A(1 + \sigma_0/\lambda)$:

$$\frac{d\left(\frac{1}{\lambda}\right)}{dt} = \frac{\dot{m}_A}{m_{Aexh}} \cdot \left[-\frac{1}{\lambda(t)} + \frac{1}{\lambda_{IN}(t)}\right], \quad (3.22)$$

3. Dynamics Adjacent to the Wall Wetting

where m_{Aexh} is the only unknown of the equation. It stands for the total exhaust gas mass involved in the mixing and can be calculated from the identified mixing time constant. The value of \dot{m}_A can be substituted with the mean value as well. The relationship between the time constant of the mixing τ_{mix} and the mixing air mass m_{Aexh} can be expressed as:

$$\tau_{mix}[\text{s}] = \frac{120}{n} \cdot \frac{m_{Aexh}}{m_A} = T_s \left[\frac{\text{s}}{\text{cyl}} \right] \cdot \frac{m_{Aexh}[\text{g}]}{m_A \left[\frac{\text{g}}{\text{cyl}} \right]}. \quad (3.23)$$

Note that if the volume between the exhaust valve and the sensor is smaller than the volume occupied by the gas in the cylinder at the pressure and temperature condition in the exhaust, the exhaust mixing phenomena will be negligible. To verify this condition the volume of the total exhaust mass that exits from the cylinder is calculated with Equation 3.26 at the measured pressure and temperature. The result is that the volume occupied by the gas at the worst conditions¹ is almost 2.5 times bigger than the volume between the cylinder and the sensor. Exhaust mixing cannot be completely neglected, but it plays an unimportant role in this investigation.

Sensor Dynamics

The dynamics of the λ sensor were identified using the measured frequency response compared to the measurements with the NO measurement device [53]. The resulting dynamic element has the behavior of a first order low-pass filter with a time constant of about 20 ms (Figure 3.7).

¹low temperature, low mass-flow

3.3. Estimation of the Exhaust Gas Dynamics

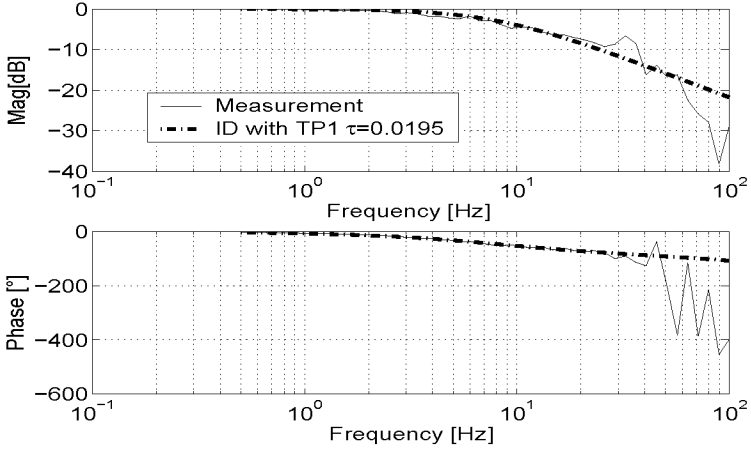


Figure 3.7: Measured λ sensor dynamics and model results.

$$G_{LSU}(s) = \frac{1}{0.02 \cdot s + 1}. \quad (3.24)$$

This sensor is connected to special electronics, which have been modified in order to increase its bandwidth.

As explained in Section 3.3.3, the identification is based on the NO measurement device, whose dynamics are given by a low-pass element and a delay resulting in the following transfer function:

$$G_{NO}(s) = \frac{1}{0.004 \cdot s + 1} \cdot e^{-0.008 \cdot s}. \quad (3.25)$$

3. Dynamics Adjacent to the Wall Wetting

3.3.3. Identification of the Parameters

Methodology

In order to identify the system parameters without involving other dynamics, the experiments have to be chosen so that the excitation signal for the frequency response is focused on the specific elements, i.e., from the cylinder to the sensor. The mechanism of formation of NO has the advantage that by holding the other operating conditions (constant air mass flow and constant fuel injection), it depends linearly on the spark-advance angle (over the wide region depicted in Figure 3.8). In addition to that, NO is formed in the cylinder when the intake valves are closed. The post-formation in the exhaust can be assumed to be negligible, for the NO reaction freezes at high temperatures [30] (higher than in the exhaust).

3.3. Estimation of the Exhaust Gas Dynamics

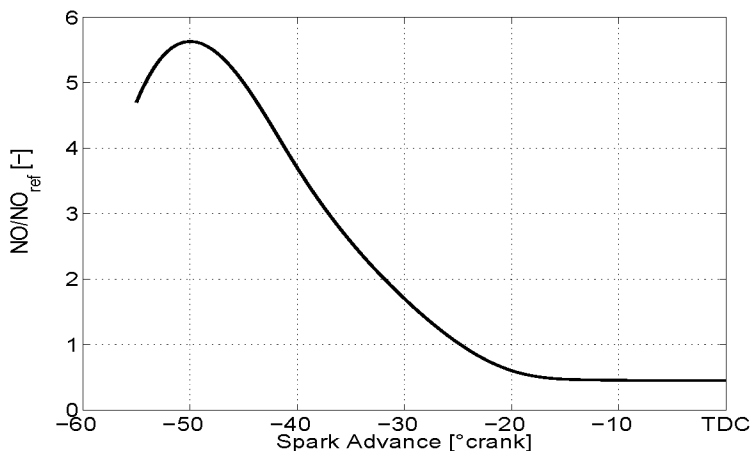


Figure 3.8: Relationship spark-advance — relative NO concentration in the exhaust.

Last but not least, the NO device is a very fast sensor (see Equation 3.25), which enables to measure the high-frequent dynamics.

Measurement of the Determinable Variables

Exhaust temperature: The exhaust temperature for the interesting operating range of the engine was measured directly after the exhaust valves, that is, in the same spot where the NO measurement device and the A/F sensor are placed. The resulting temperatures for 1500 rpm are depicted in Figure 3.9.

3. Dynamics Adjacent to the Wall Wetting

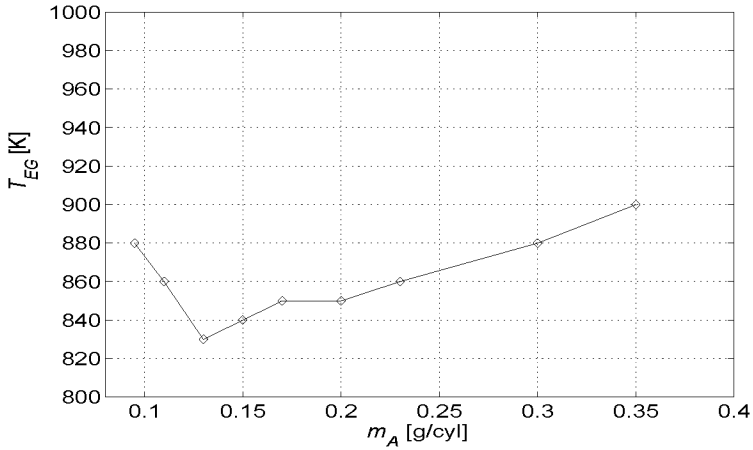


Figure 3.9: Measured exhaust temperature T_{EG} .

Exhaust pressure: The exhaust pressure for the interesting operating range of the engine was measured directly after the exhaust valves, as well. The result for 1500 rpm is depicted in Figure 3.10.

3.3. Estimation of the Exhaust Gas Dynamics

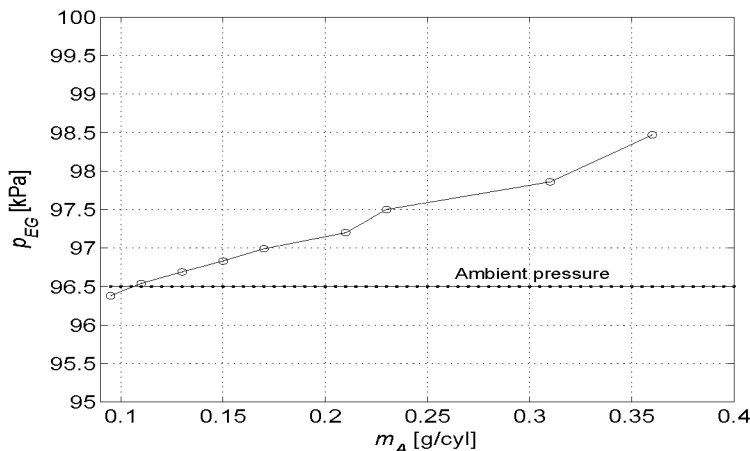


Figure 3.10: Measured exhaust pressure p_{EG} .

Notice that in the operating point with the lowest air mass flow the measured exhaust pressure lies slightly below the measured ambient pressure of 96.5 kPa.

Maximum exhaust volume: With the maximum exhaust volume is intended the largest volume between the exhaust valves and the sensor position. This is given by the diameter of the tube and the distance between the exhaust valve's seat and the sensor, namely

$$V_{Amax} = \frac{(0.04\text{m})^2 \cdot \pi \cdot 0.05\text{m}}{4} = 6.28318 \cdot 10^{-5} \text{m}^3. \quad (3.26)$$

Note that if there is no exhaust mixing ($\tau_{mix} \equiv 0$) the volume used in the model for the exhaust delay is exactly V_{Amax} . On this case the expected delay is depicted in Figure 3.11 (example for 1500 rpm).

3. Dynamics Adjacent to the Wall Wetting

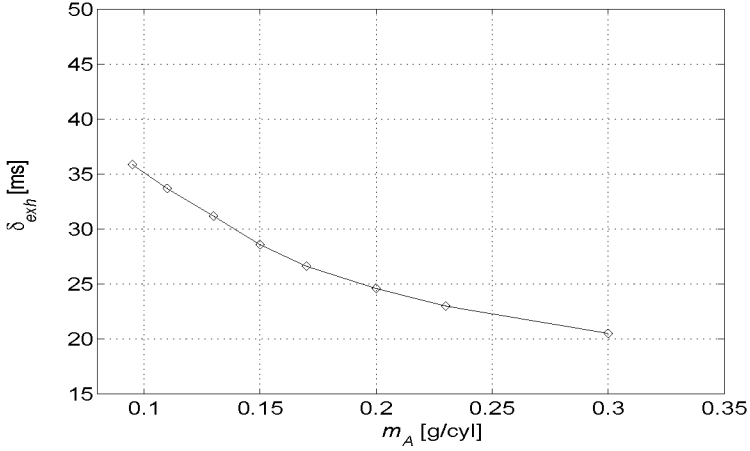


Figure 3.11: Modeled exhaust delay δ_{exh} [ms].

Identification of the Unknown Variables

Residual gas fraction C:

$$\begin{aligned}
 (m_A + m_F)_{out} &= (1 - C) \cdot (m_A + m_F)_k & C &= f(m_A, n) \\
 (m_A + m_F)_k &= C \cdot (m_A + m_F)_{k-1} + (m_A + m_F)_{in}. \quad (3.27)
 \end{aligned}$$

Usually, the mass of NO is so small in comparison to the total mass, that it is negligible for the exhaust dynamics. However, when the air mass m_A and the fuel mass m_F are constant, the mass of NO becomes the tracking value for the measurement of the dynamics. The NO device cannot measure the mass directly, but the concentration. Therefore, Equation 3.27 must be written as:

$$\begin{aligned}
 (\text{NO} \cdot K_I)_{out} &= (1 - C) \cdot (\text{NO} \cdot K_I)_k \\
 (\text{NO} \cdot K_I)_k &= C \cdot (\text{NO} \cdot K_I)_{k-1} + (\text{NO} \cdot K_I)_{in}, \quad (3.28)
 \end{aligned}$$

3.3. Estimation of the Exhaust Gas Dynamics

where K_I is the conversion between [ppm] and [g] [33]:

$$[\text{ppm}] \sim \frac{V}{V_{tot}} = \frac{n_m}{n_{mtot}} = \frac{M_{tot}}{\underbrace{M_{NO} \cdot m_{tot}}_{\sim 1/K_I}} \cdot m[\text{g}] \quad (3.29)$$

where M_{NO} is the molar mass of NO, M_{tot} is the molar mass of the exhaust gas, n_m is the number of moles of NO, and n_{mtot} is the number of moles of the exhaust gas. If K_I is constant in all operating points, it can be concluded that concentration measurements are equivalent to mass measurements. By looking closely at Equation 3.28 it can be seen that the factor K_I can be effectively handled as constant, because M_{NO} is constant and the variations of the total mass and the total molar mass are negligible due to the very small contribution of NO. As a result, Equation 3.28 becomes:

$$\begin{aligned} (\text{NO}[\text{ppm}])_{out} &= (1 - C) \cdot (\text{NO}[\text{ppm}])_k \\ (\text{NO}[\text{ppm}])_k &= C \cdot (\text{NO}[\text{ppm}])_{k-1} + (\text{NO}[\text{ppm}])_{in}. \end{aligned} \quad (3.30)$$

And around an operating point:

$$\begin{aligned} \Delta \text{NO}_{out} &= (1 - C_{OP}) \cdot \Delta \text{NO}_k \\ \Delta \text{NO}_k &= C_{OP} \cdot \Delta \text{NO}_{k-1} + \Delta \text{NO}(\Delta ZW)_{in}, \end{aligned} \quad (3.31)$$

where C_{OP} is the value of C in a specific operating point.

Exhaust volume V_A : This element has to be identified if there is a reasonable doubt that the exhaust mixing phenomena occur. In this case, the observability of the whole system is in danger. In order to avoid problems, the sensor has to be placed the nearest possible.

3. Dynamics Adjacent to the Wall Wetting

If there is no exhaust mixing to be expected the physical model for the exhaust delay with the maximum volume yields optimal identification results.

Discussion on the NO-Based Approach

Problems: The measurement of NO concentration has some disadvantages. Actually, the identification model is based on the assumption that the NO generated in the previous cycle remains inert during the following cycle. This is due to the fact, that at low temperatures the reaction of NO is blocked. In the cylinder these temperatures are reached only during the next combustion stroke. The main questions are: how much old NO is reduced during this stroke? And how much does this extra reduction affect the quality of the identification (correctness)?

Influence of a reduction of NO on the dynamics: To obtain Equation 3.30 and Equation 3.31 a negligible reduction of the NO was assumed. This subsection shows what happens, if this assumption is not valid. In order to determine the changes in the dynamics, a closer look at the physical process has to be considered.

There are various possibilities in which the NO may be reduced, violating the assumption of continuity for its concentration. To describe the two most important options, the time line of the events is observed (Figure 3.12).

3.3. Estimation of the Exhaust Gas Dynamics

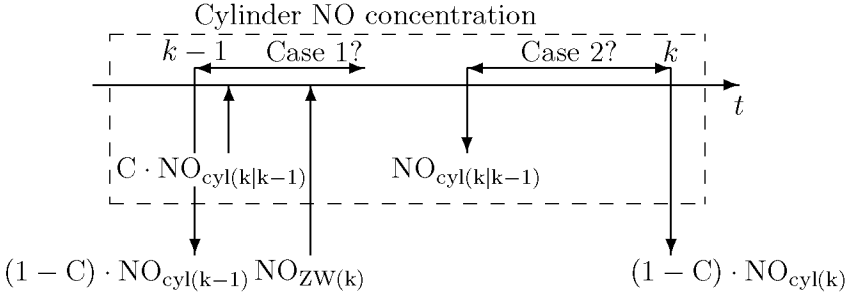


Figure 3.12: Time line of the cylinder's events.

During the time between two opening of the exhaust valves, marked with $k - 1$ and k , various NO masses are present in the cylinder: At the beginning, i.e., as soon as the exhaust valves are closed, the NO mass in the cylinder consists of the remaining part of the NO previously generated (in Figure 3.12 it appears as $C \cdot \text{NO}_{\text{cyl}(k|k-1)}$). In a second moment, i.e., during the combustion, the new NO is generated ($\text{NO}_{\text{ZW}(k)}$). These NO concentrations are added to obtain $\text{NO}_{\text{cyl}(k|k-1)}$. After the combustion, while the exhaust valves are still closed, the new mass can be reduced to the final mass $\text{NO}_{\text{cyl}(k)}$, whose part of it $(1 - C)$ exits to the exhaust after the opening of the valves.

Case 1: We assume that a part of the remaining NO is reduced before or during the combustion. This means that $\text{NO}_{\text{cyl}(k|k-1)}$ is not equal to $\text{NO}_{\text{cyl}(k-1)}$, but to $A_r \cdot \text{NO}_{\text{cyl}(k-1)}$, with A_r being the reduction coefficient ($A_r=0 \dots 1$, $A_r=1$ is equivalent to no

3. Dynamics Adjacent to the Wall Wetting

reduction). The transfer function can be easily adjusted:

$$G(z) = \frac{z \cdot (1 - C)}{z - A_r \cdot C}. \quad (3.32)$$

In this case the changes to the frequency response of the in-cylinder mixing are depicted in Figure 3.13.

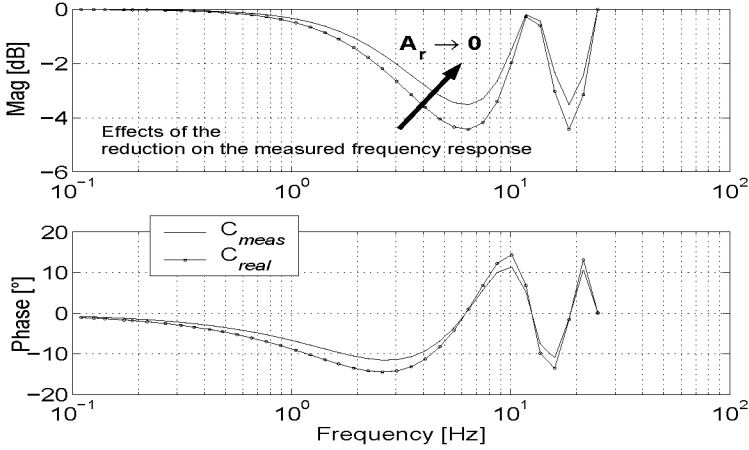


Figure 3.13: Effects of the reduction on the measured frequency response (Case 1), steady-state scaled to 0 dB.

Note that the changes in the static transfer coefficient ($z=1$, frequency=0 Hz) are eliminated by measuring around an operating point. By a smaller value of A_r the measured response seems faster than the reality. This leads to an identified C_{meas} which is smaller than the real, namely $C_{meas} = A_r \cdot C_{real}$. The real value of A_r is not measurable and thus C_{real} cannot be calculated. However, the fact that the identified C_{meas} has decent values shows that the reduction is negligible.

3.3. Estimation of the Exhaust Gas Dynamics

Case 2: We assume that the back-reduction is performed after the formation of the new NO and involves the whole species, i.e., $\text{NO}_{\text{cyl}(k)}$ is equal to $A_r \cdot \text{NO}_{\text{cyl}(k|k-1)}$. The transfer function is shown in Equation 3.33.

$$G(z) = \frac{z \cdot (1 - C) \cdot A_r}{z - C} \quad (3.33)$$

In this case the changes to the frequency response of the in-cylinder mixing are depicted in Figure 3.14.

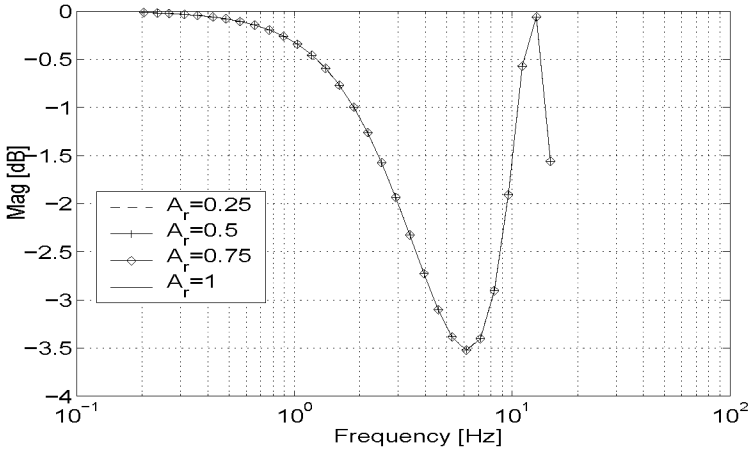


Figure 3.14: Effects of the reduction on the measured frequency response (Case 2), steady-state scaled to 0 dB.

Since the identification of C is based on the measurement of the dynamic behavior and not on the steady-state values, it is not disturbed by the effects of the reduction which leave the poles of Equation 3.33 undisturbed, i.e., a bias in the steady-state transfer coefficient cannot be distinguished.

3. Dynamics Adjacent to the Wall Wetting

Which one of these cases is correct? Without a very specific modeling effort, which would exceed the boundaries of this thesis, it cannot be stated for sure. However, it can be assumed that the effects described in the first case are negligible [50].

The conclusion is that the back-reduction of NO is possible, but this causes no particular problems to the identification of the residual gas fraction C since it does not interfere remarkably with the poles of the transfer function (Equation 3.13).

3.3.4. Influence of External EGR on the Structure of the Model

Up to this point, the model represents the case where no external EGR is present on the system. However, modern engines can have an external EGR circuit. It is thus interesting to consider the case where NO is feeded back through the external EGR. The structure can be obtained by extending the discrete in-cylinder mixing with the EGR feed back.

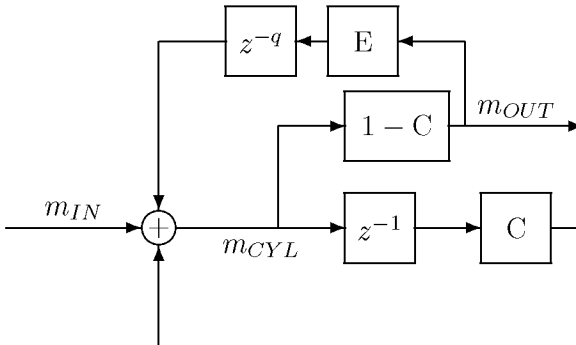


Figure 3.15: In-cylinder mixing with external EGR.

3.3. Estimation of the Exhaust Gas Dynamics

Note that in this scheme the delay caused by the external EGR circuit has been approximated for simplicity with an multiple of the sample time, namely $\delta_{eEGR} = q \cdot T_s$ with $q = 1, \dots, n$. This scheme contains the new parameter E, which stands for the dilution of the concentration of NO by the mixing with the fresh gases entering the cylinder. The result of this scheme is the following transfer function:

$$G(z) = \frac{z^q \cdot (1 - C)}{z^q - C \cdot z^{q-1} - E(1 - C)}. \quad (3.34)$$

It is evident that if no external EGR is present ($E=0$), the model is the same as in Equation 3.13.

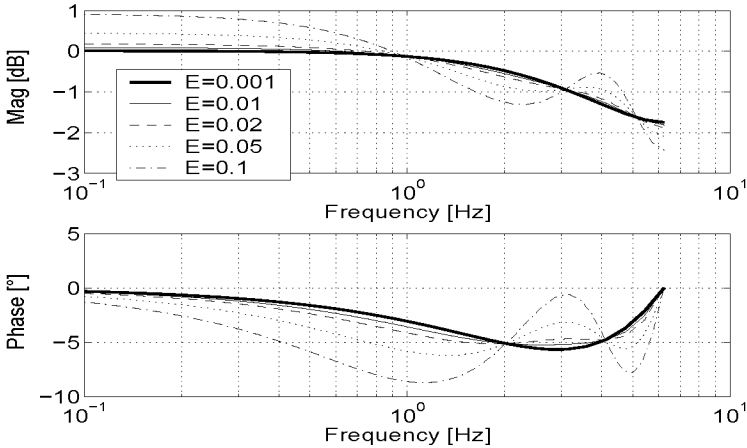


Figure 3.16: Influence of the parameter E ($C=0.1$).

The influence of E is negligible up to 1% dilution ($E=0.01$). Above that, it becomes relevant for the behavior of the system. Above 10% dilution, the effect is remarkable, in particular on the phase

3. Dynamics Adjacent to the Wall Wetting

of the system. This comparison is done with the assumption of a 10% residual gas fraction ($C=0.1$) and $q = 4$.

The simulations showed that the influence of the external EGR (E) was inversely proportional to the internal residual gas fraction (C).

Interestingly, the presence of external EGR does not change the influence of the residual gas fraction C on the result (see Figure 3.13). In Figure 3.17 is depicted the influence of C by a 10% external EGR ($E=0.1$).

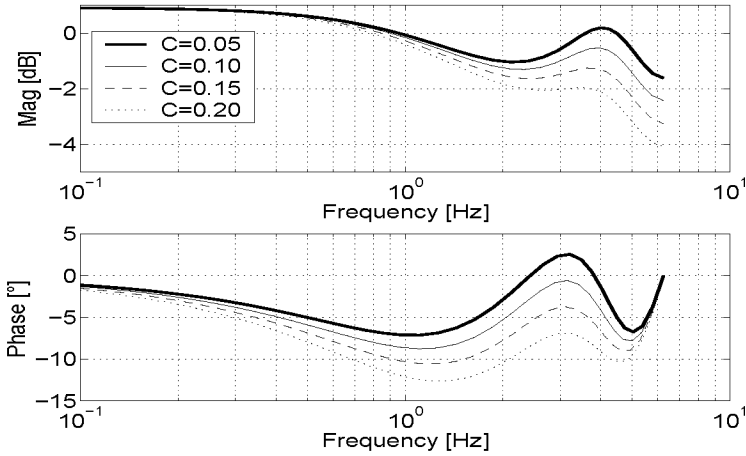


Figure 3.17: Influence of the parameter C ($E=0.1$).

By the presence of the external EGR the emission level of NO is significantly reduced. Therefore, in the operating points where a large external EGR percentage is used, an inconvenient signal for the identification is expected.

3.3.5. Identification Results

Before presenting the results obtained, the identification of the parameters is discussed.

As explained in Section 3.3.3, the delay δ_{delay} can be identified simultaneously with the residual gas fraction C . The use of the modeled delay was tested, as well. Due to the fact that by most of the operating points the identified delay is very near to the modeled delay (Figure 3.18) the results for the residual gas fraction C were almost the same.

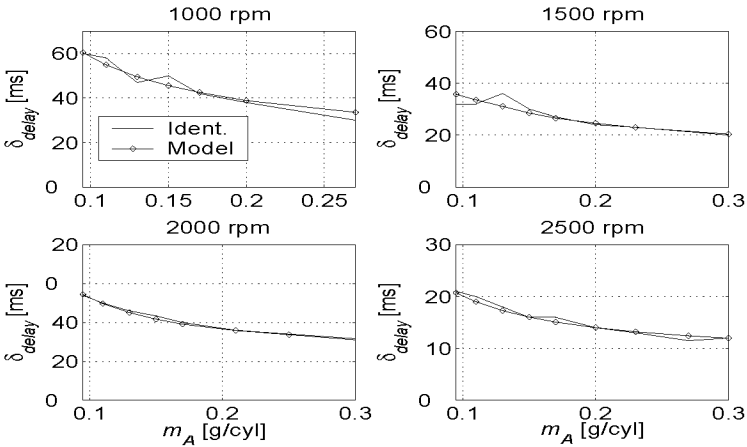


Figure 3.18: Identified delay vs. modeled delay (δ_{delay}).

The identification was performed in various operating points, which are described by engine speed n and air mass per cylinder per cycle m_A .

3. Dynamics Adjacent to the Wall Wetting

Table 3.1: Operating points.

m_A [g/cyl]	n [rpm]
0.095	1000
0.11	1500
0.13	2000
0.15	2500
0.17	3000
0.20	
0.23	
0.27	
0.30	

Figure 3.19 shows an example of the frequency response of the system and the results of the identification. Figures 3.20 and 3.21 show the results of the identification of the residual gas fraction C in every operating point.

3.3. Estimation of the Exhaust Gas Dynamics

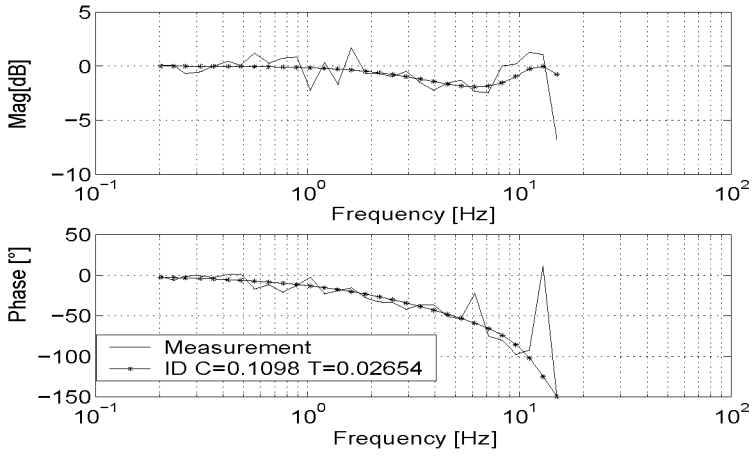


Figure 3.19: Frequency response at 1500 rpm, 0.17 g/cyl.

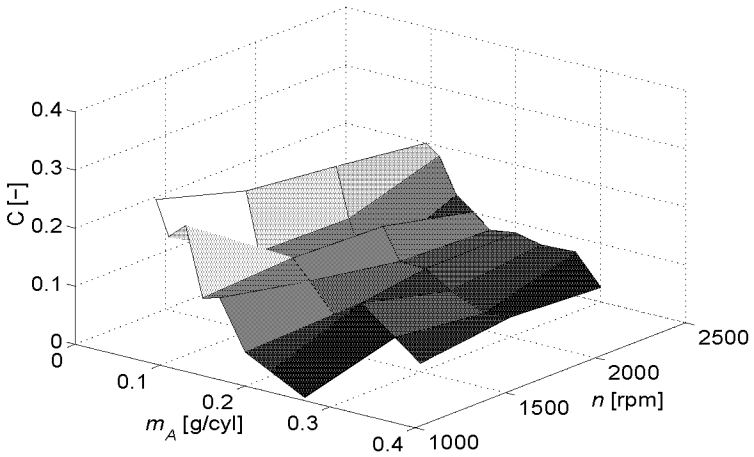


Figure 3.20: Residual gas fraction C .

3. Dynamics Adjacent to the Wall Wetting

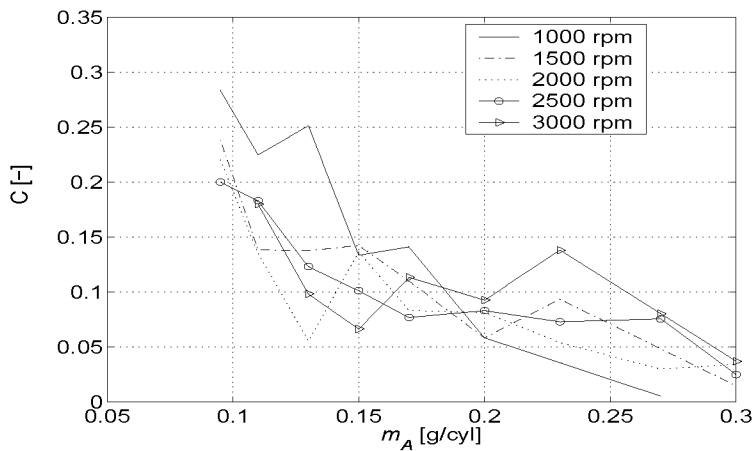


Figure 3.21: Residual gas fraction C .

3.4. Discussion

In conclusion of this investigation some interesting points are discussed.

An useful tool to identify the residual gas fraction for a single cylinder with a NO sensor placed near to the exhaust valve was obtained. However, this process is not cost-free; In particular the identification process is quite time-consuming: every measurement in an operating point lasts from 15 up to 20 minutes. Moreover, if the sensor is placed too far from the exhaust valve, i.e., where the exhaust mixing dynamics are strongly expected (see Section 2.2), the distinction between in-cylinder mixing and exhaust mixing becomes problematic. This is due to the same type of both system, i.e., first order low-pass filter.

Problems may also arise in case of difficult operating points, such as operating points with high load and high engine speed, because of the high temperature in the exhaust. The phenomenon of the residual gases is strong only at low loads and low engine speeds, therefore the measurements for this investigation were limited up to 3000 rpm.

These models represent the desired starting point for investigations of the wall wetting system. For the following part of the thesis, the adjacent dynamics can be considered as known.

3. *Dynamics Adjacent to the Wall Wetting*

4. Model of the Wall Wetting Dynamics based on Physics

4.1. Introduction

Now that all the adjacent dynamics have been identified, the focus can be set on the actual wall wetting dynamics. The goal of this chapter is to provide a general, rapidly tunable wall wetting model. The model is developed taking into account the effects of the temperature, pressure, and composition of the fuel. The result of this process should be able to model every possible situation which occurs in the intake manifold. The rapid tunability implies that the model should maintain a simple structure without losing the sensitivity to the major influence factors on the dynamic behavior (air mass flow, temperature, and pressure).

The chapter is structured in two parts: The first part gives an introduction in the mass-transfer by convection (Section 4.2). The second part describes the wall wetting model (Sections 4.3-4.7). The model itself can be separated into three subsystems, namely the evaporation of the droplets (Section 4.3), the evaporation of the fuel film (Section 4.5), and a model for the temperature of the film (Section 4.7). In Sections 4.4 and 4.6, the wall wetting parameters obtained with the droplet and film model are compared to the results obtained by identification on a current SI engine.

4.2. Description of the Convection Phenomenon

The wall wetting system is caused by various physical phenomena. However, the main phenomenon by which the wall wetting can be modeled is the mass transfer by convection.

In mass transfer by convection, gross fluid motion combines with diffusion to promote the transport of species for which there exists a concentration gradient. There are two types of convection, the first is called “free” convection and the second is called “forced” convection. The difference between these convection types resides in the environmental conditions.

4.2.1. Free Convection

The free convection is considered when the convection occurs when no external forcing conditions applies. In fact, the concentration gradient is dependent on the diffusivity coefficient alone. An example for this convection is what happens to a highly volatile fluid (methanol, etc.) left in a calm air condition. Since free convection flow velocities are generally much smaller than those associated with the forced convection, the corresponding transfer rates are also smaller.

4.2.2. Forced Convection

The main difference between free and forced convection lies in the fact that the gradient is “forced” by external means, for example a blowing flow at the surface.

4.2. Description of the Convection Phenomenon

Both convection types have the form:

$$\dot{N} = -D_{AB} \cdot \frac{\partial C_c}{\partial y}, \quad (4.1)$$

where C_c can be temperature, velocity or concentration. \dot{N} can be the heat flux, the frictional drag, or the molar flux, respectively. In the case of heat flux, Equation 4.1 is called Fourier's law. In the case of molar flux, it is called Fick's law. In Fick's law D_{AB} represents the *binary diffusion coefficient* [33, Chapter 6]. In this section, the attention will be focused on the implications of the Fick's law.

The mass convection is caused by a difference in concentration of a specific species. In analogy with the heat transfer, it can be written as:

$$\dot{N}_A = \bar{h}_m A_s (C_{A,s} - C_{A,\infty}), \quad (4.2)$$

where \bar{h}_m [m/s] is the average *convection mass transfer coefficient*. Combining Equations 4.1 and 4.2, it follows that:

$$h_m = \frac{-D_{AB} \cdot \partial C_A / \partial y|_{y=0}}{C_{A,s} - C_{A,\infty}}. \quad (4.3)$$

The solution of every convection problem is found by measuring or estimating this coefficient. Several methods are possible, one of them is called Reynolds analogy and it will be discussed later. As mentioned before, the forced convection is boosted due to a flowing media on the surface of another media. The boosting strength is dependent on the velocity of this flux and on its flow characteristic. The layer where the convection takes place is the *boundary layer*.

An essential first step in the treatment of any convection problem is to determine whether the boundary layer is laminar or turbulent.

4. Model of the Wall Wetting Dynamics based on Physics

In the laminar boundary layer, fluid motion is highly ordered and it is possible to identify streamlines along which particles move. Fluid motion along a streamline is characterized by velocity components in both directions (normal and parallel to the surface). In contrast, fluid motion in the turbulent boundary layer is highly irregular and is characterized by velocity fluctuations. These fluctuations enhance the transfer of species, and hence increase the convection transfer rate.

The distinction between laminar and turbulent layer can be achieved approximatively with the help of the dimensionless variable called *Reynolds number*:

$$Re_x \equiv \frac{u_\infty x}{\nu}, \quad (4.4)$$

where x is a characteristic length, ν is the *kinematic viscosity* of the fluid and u_∞ is the velocity of the fluid outside the boundary layer. If Re_x grows to be bigger than a critical value Re_{critic} then the turbulence condition applies.

This value is thus relevant for the estimation of the convection mass transfer coefficient.

4.2.3. Reynolds Analogy

In order to explain the Reynolds analogy, we have to introduce other dimensionless groups, namely the *Schmidt number* Sc , and the *Sherwood number* Sh . The Schmidt number represents the ratio between momentum and mass diffusivity:

$$Sc \equiv \frac{\nu}{D_{AB}}. \quad (4.5)$$

4.2. Description of the Convection Phenomenon

The Sherwood number represents the dimensionless concentration gradient at the surface:

$$Sh \equiv \frac{h_m \cdot L}{D_{AB}}. \quad (4.6)$$

The consequence is that the knowledge of Sherwood number is a key factor for the calculation of h_m as defined in Equation 4.3. For the estimation of the Sherwood number, a practical analogy can be used: the Reynolds analogy. The equivalence is given by:

$$Sh = C_r \cdot Re^{m_r} \cdot Sc^{n_r}, \quad (4.7)$$

where the parameters C_r , m_r and n_r can be estimated experimentally and are the same for every equivalent problem. The methodology adopted to derive this analogy equivalence is explained in the literature [33, chapter 7]. This analogy was derived for flowing fluids. To adapt the analogy to the case of free convection, it can be written as:

$$Sh = 1 + C_r \cdot Re^{m_r} \cdot Sc^{n_r}, \quad (4.8)$$

where the term 1 covers the case where the flow is quasi still.

4.2.4. Evaporating Fuel Mass

The equation for the evaporating fuel mass \dot{m}_{EV} can be given in two possible forms:

$$\dot{m}_{EV} = \frac{h_m A_F}{R_F T_F} (p_{vs}(T_F) - p_{vm}), \quad (4.9)$$

where $p_{vs}(T_F)$ is the saturated pressure of the fuel vapor at the surface, A_F is the surface which evaporates. Its temperature de-

4. Model of the Wall Wetting Dynamics based on Physics

pendency can be approximated with the solution of the *Clausius-Clapeyron* equation (see [63]):

$$p_{vs}(T_F) = p_{vs0} \cdot e^{-\frac{svc}{T_F}}. \quad (4.10)$$

The coefficient h_m is given as:

$$h_m = Sh \frac{D_{AB}}{d}, \quad (4.11)$$

where d is a characteristic length.

The second form is expressed in terms of fraction of fuel evaporated:

$$\dot{m}_{EV} = \frac{\rho_{vs} D_{AB} A_F}{d} \cdot Sh \cdot \ln(1 + B), \quad (4.12)$$

where ρ_{vs} is the density at the surface and is calculated by means of the properties of the liquid and of the gas form. For example:

$$\rho_{vs} = \frac{\rho_l + \rho_v}{2}. \quad (4.13)$$

The parameter B represents the *Spalding number*:

$$B = \frac{\chi_{vs,\%}(T_F) - \chi_{vs,\%}\infty}{1 - \chi_{vs,\%}(T_F)}, \quad (4.14)$$

where $\chi_{vs,\%}(T_F)$ stands for the fraction of the fuel vapor at the surface for the specific temperature T_F , and $\chi_{vs,\%}\infty$ stands for the fraction of fuel vapor in the surroundings. The equivalence of these two forms is shown in [37].

In this work, the second form was used.

4.2. Description of the Convection Phenomenon

4.2.5. Fuel Properties

The fuel used in the tests has been analyzed at the EMPA¹. Its characteristics are listed in Table 4.1 and in the evaporation curve (Figure 4.1).

Table 4.1: Fuel data.

Description	Value	Unit
Research octane number RON	99.3	
Motor octane number MON	88.0	
Density Liquid (20°C)	746.6	kg/m ³
Reid's steam pressure	80.6	kPa
Sulfur	0.0035	% Weight
Lead	< 2	mg/l
Benzol	0.6	% Volume
Carbon	85.90	% Weight
Hydrogen	13.29	% Weight
Oxygen	1.70	% Weight
HC-ratio	1.843	
Stoichiometric factor	14.336	kg/kg _{fuel}
Molecular weight	≈ 112.2	kg/kmol

¹Swiss Federal Laboratories for Material Testing and Research.

4. Model of the Wall Wetting Dynamics based on Physics

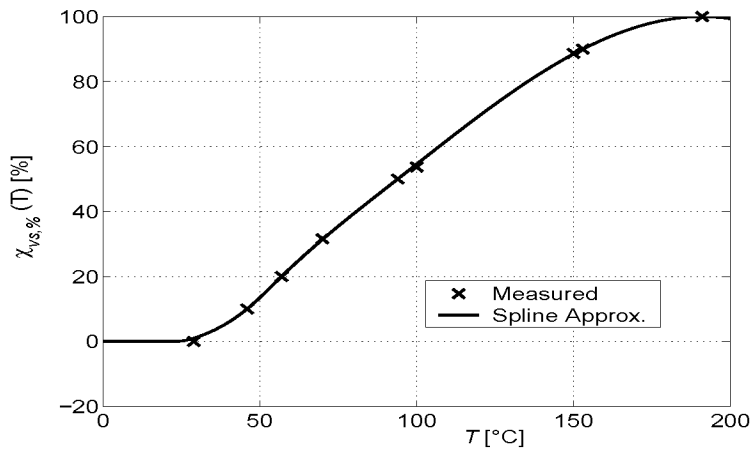


Figure 4.1: Evaporation curve of the fuel.

4.3. Droplet Evaporation

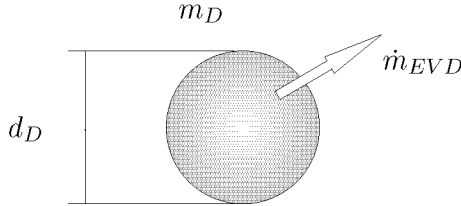


Figure 4.2: Evaporation over a spherical droplet.

There is a large spectrum of documentation which deals with fuel evaporation and droplet evaporation, for example [24] or [43]. The evaporation of the fuel in the intake duct is a special case of convection, a convection with phase change.

The equation for the evaporated fuel mass flow is expressed with the droplet diameter as characteristic length:

$$\dot{m}_{EVD} = \frac{\rho_D v_s D_{AB} A_D}{d_D} \cdot Sh_D \cdot \ln(1 + B). \quad (4.15)$$

The value of the Sherwood number Sh_D has to be estimated.

4.3.1. Forced Convection on a Droplet

The forced convection on a droplet is due to the velocity by which the droplet flies from the injector to the wall. This velocity at the exit of the injector can be quantified with the help of Bernoulli equation:

$$v_{inj} = \sqrt{\frac{2}{\rho_{DI}} (p_{inj} - p_I)}. \quad (4.16)$$

4. Model of the Wall Wetting Dynamics based on Physics

During the flight the velocity will decrease due to aerodynamic forces. Therefore, a mean value for the calculation of Reynolds number can be expressed as:

$$v_D = \alpha_1 \cdot \sqrt{\frac{2}{\rho_{DI}}(p_{inj} - p_I)}, \quad (4.17)$$

with $0 < \alpha_1 \leq 1$. Due to the fact that the droplets are injected into a moving flow (waves), the total velocity is:

$$v_{D\infty} = v_D + v_{Flow}(\dot{m}_A). \quad (4.18)$$

The value for v_{Flow} will be expressed later. The Reynolds number for the droplet is defined as:

$$Re_D = \frac{v_{D\infty} \cdot d_D}{\nu}, \quad (4.19)$$

where d_D is the instantaneous diameter of the droplet.

To express the value of the transfer coefficient h_m with the Reynolds analogy, we need the experimental values m_r , n_r and C_r for Equation 4.7. One opportunity is given by the Ranz-Marshall correlation.

Ranz-Marshall Correlation

This correlation is based on the work of W. E. Ranz and W. R. Marshall on evaporation of droplets [55]. Their results are highlighted in the following equation:

$$\dot{m}_{EVD} = \dot{m}_{fc} \cdot 2 \cdot (1.0 + 0.276 \cdot Re_D^{1/2} \cdot Sc^{1/3}), \quad (4.20)$$

where \dot{m}_{fc} is the evaporation under free convection, that is:

$$\dot{m}_{fc} = \frac{\rho_{Dvs} D_{AB} A_D}{d_D} \cdot \ln(1 + B). \quad (4.21)$$

4.3. Droplet Evaporation

Equation 4.20 represents the standard procedure to solve every droplet evaporation problem.

4.3.2. Description of the Model

The droplet model is based on various assumptions: First of all, the whole constellation of droplets is assumed to be isometric, i.e., all the droplets have the same starting diameter $d_{D,0}$. The total number of droplets is then easily calculated with:

$$N_{tot} = \frac{m_{Finj} \cdot 6}{d_{D,0}^3 \cdot \rho_{Dl} \cdot \pi}. \quad (4.22)$$

The temperature of the droplets during the flight is assumed to be constant. The diffusivity parameter D_{AB} is dependent on the temperature and on the pressure. The kinematic viscosity is held constant, while the density is a function of pressure and temperature. It follows that:

$$\frac{dm_D}{dt} = \rho_{Dl} \frac{dV_D}{dt} = \rho_{Dl} \frac{A_D}{2} \frac{dd_D}{dt} = -\dot{m}_{EVD}. \quad (4.23)$$

The droplet surface area is given by:

$$A_D = \pi \cdot d_D^2. \quad (4.24)$$

By looking at Equations 4.12 and 4.20, we see that the term \dot{m}_{EVD} is dependent on the droplet diameter d_D .

Finally, we have a nonlinear differential equation for the droplet diameter.

$$\frac{dd_D}{dt} = f(d_D, t). \quad (4.25)$$

The solution of this equation yields the behavior depicted in Figure 4.3.

4. Model of the Wall Wetting Dynamics based on Physics

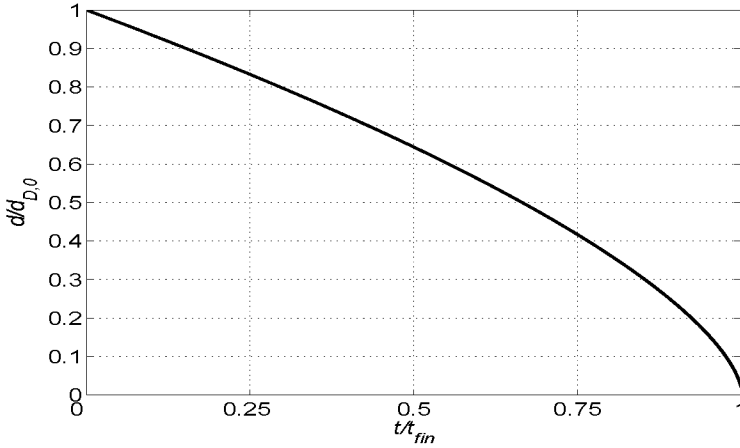


Figure 4.3: Evolution in time of the droplet diameter.

In reality, not all the droplets can follow that evolution because most of them reach the wall of the intake manifold before the evaporation process is completed, thus impinging on the fuel film. To estimate the quantity of fuel that cannot evaporate, we need a model which is able to predict at every instant how many droplets are still airborne.

4.3.3. Impact Model of the Droplets on the Wall

This section is the key point of the whole droplet model. In fact, various simulation works dealt with this problem (for example [28] and [56]). However, the flaw of these models has always been the difficult applicability to a new engine with other injector positions and/or duct diameters.

The goal is a parametrization which should not depend on the

4.3. Droplet Evaporation

operating conditions of the engine and which could be described by the lowest number of parameters. The impact model satisfies these conditions with only one parameter to be tuned.

Idea:

The number of airborne droplets decreases exponentially with the time constant τ_{DA} . The number of airborne droplets is given by:

$$N(t) = N_{tot} \cdot e^{-\frac{t}{\tau_{DA}}}. \quad (4.26)$$

N_{tot} is described in Equation 4.22.

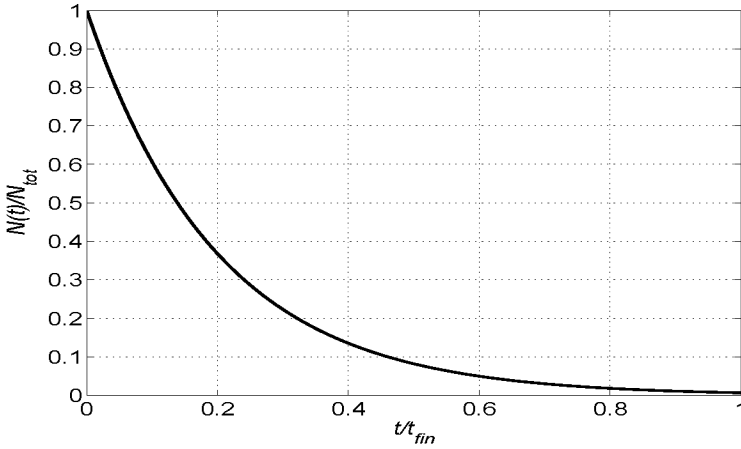


Figure 4.4: Scaled number of airborne droplets.

With the application of this idea in combination with Equation 4.12, Equation 4.25, and Equation 4.20 the definitive droplet

4. Model of the Wall Wetting Dynamics based on Physics

model can be expressed:

$$\frac{dd_D}{dt} = -\frac{2}{d_D} \cdot \frac{\rho_{Dvs}}{\rho_{Dl}} \cdot D_{AB} \cdot \ln(1+B) \cdot Sh_D \quad (4.27)$$

$$\dot{m}_{EVD} = \pi \cdot \rho_{Dvs} \cdot d_D \cdot D_{AB} \cdot \ln(1+B) \cdot Sh_D \cdot N_{tot} \cdot e^{-\frac{t}{\tau_{DA}}}.$$

The total mass that evaporates, and hence enters the cylinder, is given by:

$$m_{EVD} = \int_0^{\Delta t_{max}} \dot{m}_{EVD} \cdot dt, \quad (4.28)$$

where the value of t_{max} depends on the delay between the start of the injection and the closing of the intake valves:

$$\Delta t_{max} = t_{IVC} - t_{IS}. \quad (4.29)$$

If the temperature of the droplet is high (warm engine), the value of t_{fin} in Figure 4.3 lies in the range of 0.1, ..., 1 ms. If the temperature of the droplet is low (cold engine), the time for the complete evaporation rises to 10, ..., 15 ms. Considering that the value of Δt_{max} is dependent on the engine speed, it is possible by high engine speeds and low temperatures that the droplets do not fully evaporate before the intake valves close. The remaining droplets hence land on the wall film.

The exponential behavior can be explained by considering the real droplet speed (not constant as assumed here) as described in the following paragraph.

Real Droplet Speed:

The droplet flies with a starting speed which is given by the pressure difference between the injection rail and the intake manifold.

4.3. Droplet Evaporation

During the flight, the droplet is influenced by the aerodynamic drag:

$$F_D = \frac{1}{2} \cdot C_D \cdot \rho \cdot A_D \cdot u_D^2. \quad (4.30)$$

The drag coefficient C_D is given as function of the Reynolds number Re_D as in [38]:

$$C_D = 0.4 + \frac{24}{Re_D} + \frac{4}{\sqrt{Re_D}}. \quad (4.31)$$

Neglecting the gravity in a first approximation, following equation for the conservation of momentum results:

$$\frac{du_D}{dt} = -\frac{F_D}{m_D}, \quad (4.32)$$

and after the substitutions:

$$\frac{du_D}{dt} = -\frac{3}{4} \cdot C_D \cdot \frac{\rho}{d_D(t)} \cdot u_D^2. \quad (4.33)$$

To solve Equation 4.25, the following approximation can be introduced:

$$d_D(t) = \sqrt{d_{D,0}^2 - 4 \cdot Sh \cdot \ln(1 + B) \cdot D_{AB}}. \quad (4.34)$$

An approximation of the results for the droplet speed yields an exponential-like behavior (Figure 4.5).

4. Model of the Wall Wetting Dynamics based on Physics

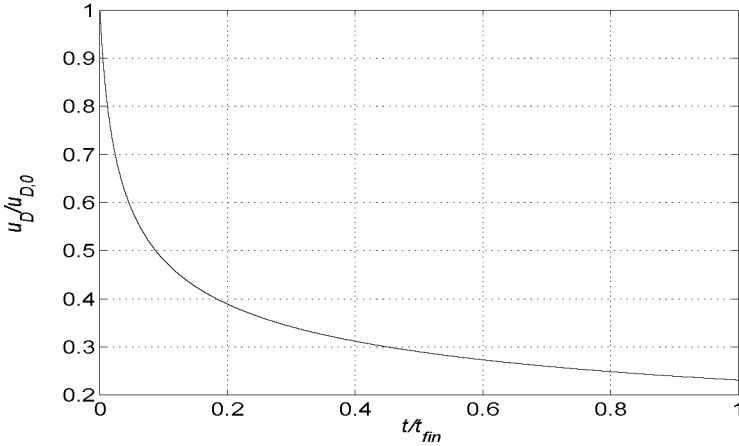


Figure 4.5: Scaled speed of the airborne droplets.

Obviously, these results do not contain information about the droplets which are airborne. A geometrical model of the intake duct and the trajectories of the droplets must be perfectly known in order to predict how many droplets are going to reach the wall and when.

The parameter τ_{DA} summarizes all these effects.

4.3.4. Main Dependencies and Tuning Parameters

This model shows all the dependencies which are expected in the real system, in particular regarding the temperature (Figure 4.8). In Figures 4.6–4.8, the main dependencies are depicted.

4.3. Droplet Evaporation

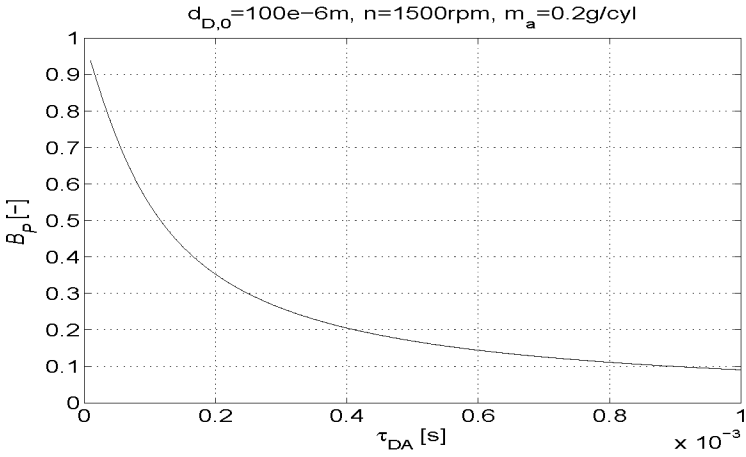


Figure 4.6: Dependency on the value of τ_{DA} .

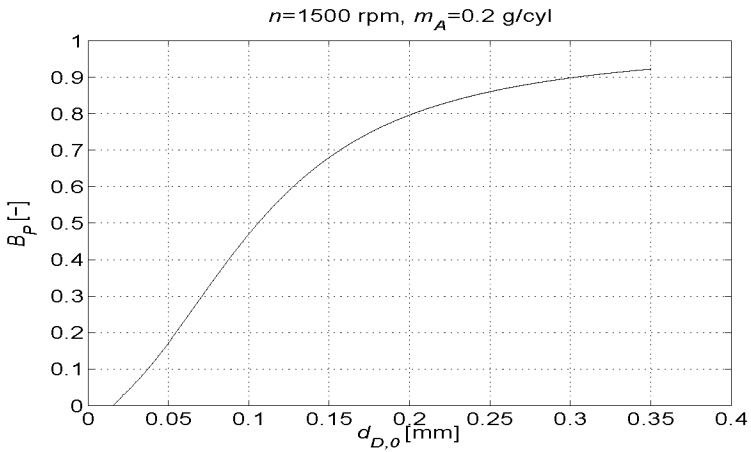


Figure 4.7: Dependency on the initial value of $d_{D,0}$.

4. Model of the Wall Wetting Dynamics based on Physics

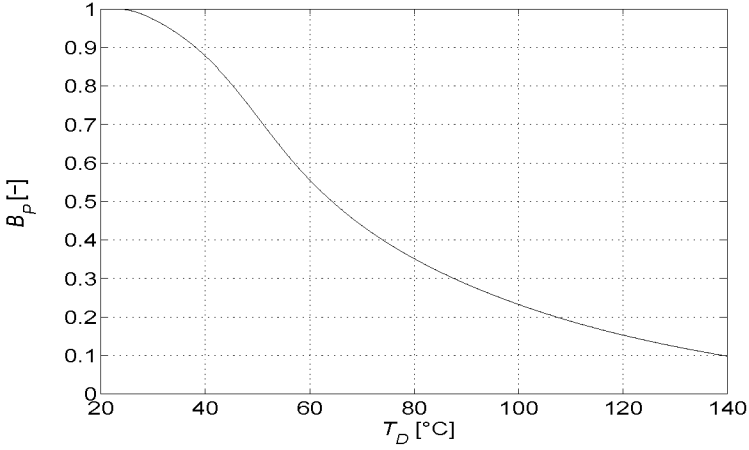


Figure 4.8: Dependency on the droplet temperature T_D .

The tuning parameters for this model are various. However, most of them can be chosen on the basis of the existing literature or be measured in separate experiments (B , for instance). In fact, the main tuning parameter remains τ_{DA} .

For example the initial droplet diameter $d_{D,0}$ depends on the injector design, the injection pressure, and other factors. For this investigation, its value was set on the basis of data collected in the literature (see [39], [44], [45], or [57]).

In future applications, other degrees of freedom could be added, for example by tuning the initial droplet diameter.

4.3.5. Temperature Model for the Droplets

The relevant droplet temperature will be estimated from the air temperature and the engine temperature, although some previous

4.3. Droplet Evaporation

studies describe the influence of the air temperature as negligible ([1] and [13]). The value to be chosen for the temperature of the droplets is given by the results of the temperature model developed in Section 4.7. The influence of the air temperature on the droplet temperature is expected to be minimal, considering the fact that the temperature in the intake manifold does not change dramatically between warm and cold engine.

4.4. Results of the Droplet Model

The comparison between the physical model and the real system can be done in different ways. For instance, a typical experiment includes the measurement of some throttle tip-in and tip-out. However, in this case we chose another procedure: The results of the droplet model will be compared with the experimental results contained in the work of M. Simons [58]. These results are surely representative, because they were obtained by frequency response measurements, technique that proved to be very efficient [53]. This comparison has the advantage that the performance of the droplet model can be tested without including the wall film model. This is obviously not possible by measuring directly on the engine.

In addition to that, the parameters were identified by compensating the exhaust gas dynamics as explained in Chapter 3.

The main goal of this section is to show that the model is able to reproduce all the measured parameters by identifying the constant value of the impact time constant τ_{DA} for the given engine.

4.4.1. Event-Based Wall Wetting Model

The discrete transfer function of the event-based wall wetting model is described as:

$$G(z) = (1 - B_P) + B_P \cdot \frac{(1 - A_P)}{z - A_P}, \quad (4.35)$$

where the parameters A_P and B_P describe the dynamics of the system. The variable z is the discrete equivalent of the variable s of the Laplace transformation:

$$z = e^{s \cdot T_s}, \quad (4.36)$$

4.4. Results of the Droplet Model

with T_s being the sample time. In the case of the event-based model, the sample time is given by the cycle time.

In the work of Simons, the parameters B_P and A_P are described as:

$$\begin{aligned} B_P &= \frac{m_{Finj} - m_{EVD}}{m_{Finj}} \\ A_P &= \frac{m_{WF} - m_{EVF}}{m_{WF}}. \end{aligned} \quad (4.37)$$

These values can be reconstructed with the help of the droplet and film models, and hence compared to the results of Simons' identification.

Measured Parameters

The identified parameters of Simons on a real engine show an increasing behavior with the load of the engine. The engine speed was held constant during the identification.

4. Model of the Wall Wetting Dynamics based on Physics

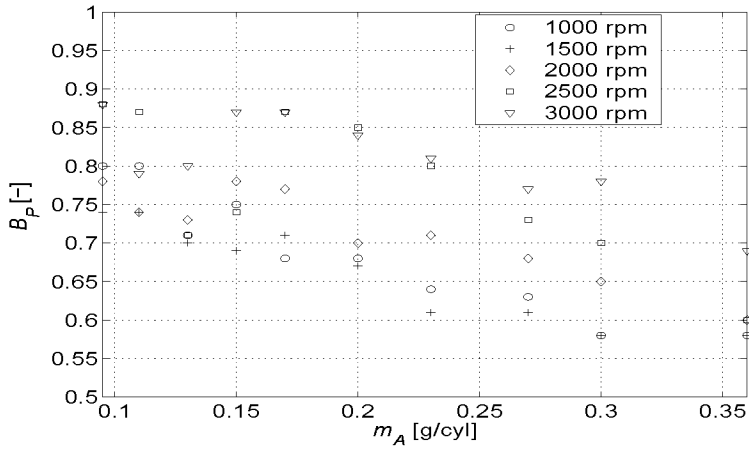


Figure 4.9: Measured impingement parameters B_P .

This means that by increasing air mass flow, and consequently increasing fuel mass flow, a smaller percentage of injected fuel impinges on the wall.

4.4. Results of the Droplet Model

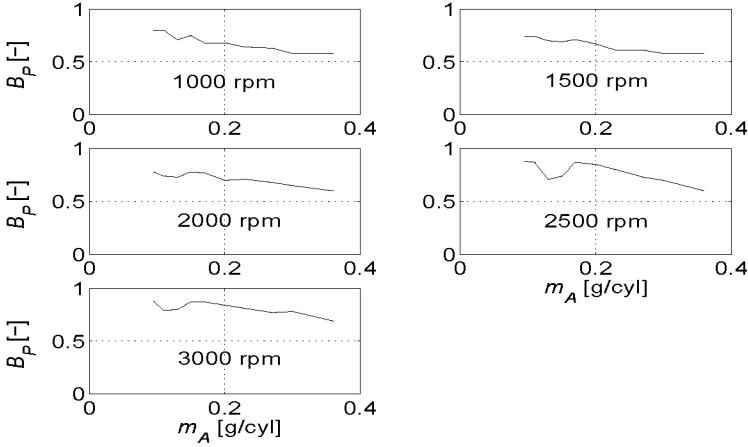


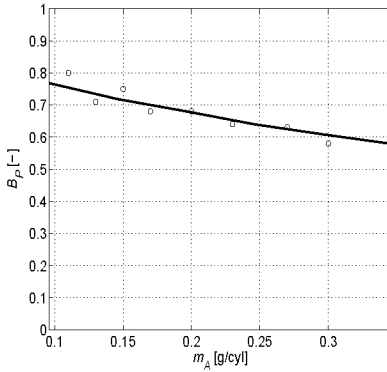
Figure 4.10: Measured impingement parameters B_p .

The uncertainties in the parameters which are remarkable at low loads (up to 0.15 g/cyl) are due to the difficult identification of the exhaust gas dynamics parameters, in particular the residual gas fraction C [42]. This particularly will also play a role in the identification task of Chapter 5.

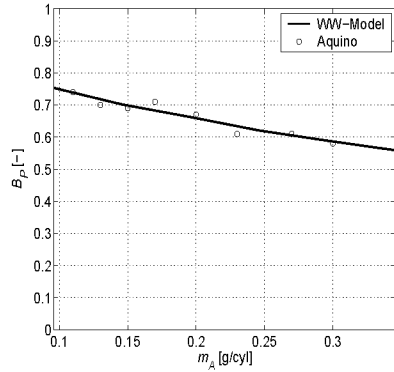
4.4.2. Comparison between Model-based Parameters and Aquino Parameters

In this section, the identified parameters are compared to the parameters which can be obtained by tuning the model. In the following figures, the parameters are depicted for all the operating conditions which were measured. Note that the parameter τ_{DA} is held constant.

4. Model of the Wall Wetting Dynamics based on Physics

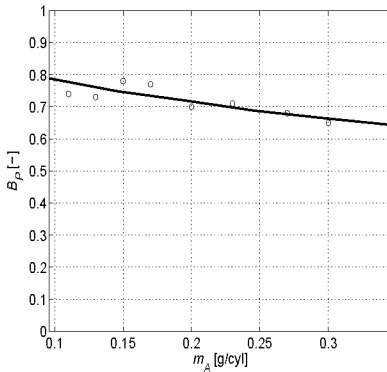


(a) Parameters at 1000 rpm.

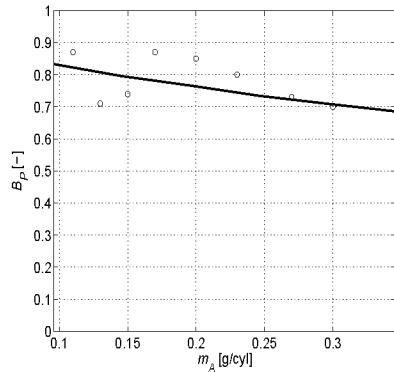


(b) Parameters at 1500 rpm.

Figure 4.11: Model results (-) compared with Simons' results (\circ).



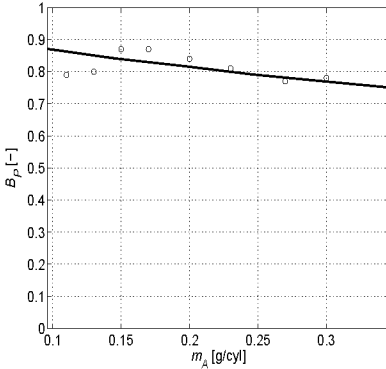
(a) Parameters at 2000 rpm.



(b) Parameters at 2500 rpm.

Figure 4.12: Model results (-) compared with Simons' results (\circ).

4.4. Results of the Droplet Model



(a) Parameters at 3000 rpm

Figure 4.13: Model results (-) compared with Simons' results (\circ).

The results show clearly that a good match between model and identification results is possible. This means that with less parameters the same results obtained with the linear model can be achieved. In addition, the model can extrapolate to the points that were not measured.

A special case is represented by the conditions at 2500 rpm: Where the identification of the residual gas fraction had less representative results, because a remarkable resonance in the intake manifold was observed. Its compensation could have disturbed the identification of the wall wetting parameters. This is suggested also by the wild behavior of the parameters at low load (Figure 4.12b).

4.5. Wall Film Evaporation

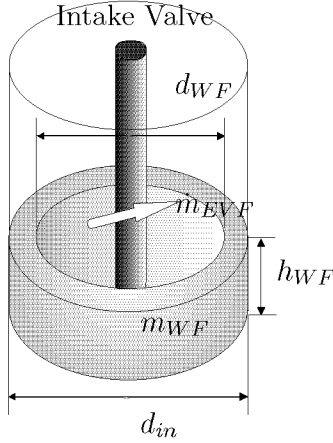


Figure 4.14: Assumption for the wall film model geometry.

Unlike the droplet model, this model is dependent on the whole wall wetting system. That is, the parameter A_P is dependent on the parameter B_P and on the wall film mass m_{WF} . A_P is defined as:

$$A_P = \frac{m_{WF} - m_{EVF}}{m_{WF}}, \quad (4.38)$$

where m_{EVF} is the evaporated fuel mass that reaches the cylinder. This dependency can give some problems in the tuning process of the model. Eventually, a correct value of A_P may be reached without a perfect match of the wall wetting fuel mass m_{WF} , but in reality, the results show a good agreement with the identification results.

4.5.1. Free and Forced Convection on the Wall Film

In the case of the wall film, the convection is driven by the air mass flow which enters or exits the cylinder. Differently from what happens with the droplets, the fuel is nearly still. Actually, a flowing of the fluid is possible due to shear forces (see Chapter 4.5.2).

The velocity responsible for the convection on the film surface is directly dependent on the air mass flow and on the area of the duct:

$$u_{A\infty} = \frac{m_A \cdot n}{20000} \cdot \frac{4}{\rho_A \cdot \pi \cdot d_{in}^2}, \quad (4.39)$$

where m_A is expressed in grams per cylinder [g/cyl], d_{in} in meter [m] and n in revolutions per minute [rpm].

The actual Reynolds number is finally:

$$Re_{WA} = \frac{u_{A\infty} \cdot d_{in}}{\nu_A}. \quad (4.40)$$

For this type of system, the parameter set for the correlation analogy was firstly identified in [23] then applied in [63]. The Sherwood number is given by:

$$Sh_F = 1 + 0.023 \cdot Re_{WA}^{0.83} \cdot Sc^{0.44}, \quad (4.41)$$

and the evaporation film mass is given in [63] as:

$$\dot{m}_{EVF} = \frac{\rho_{Fvs} \cdot A_{WF}}{d_{in}} \cdot D_{AB} \cdot Sh_F \cdot \ln(1 + B). \quad (4.42)$$

The total mass of the wall film can be obtained by integrating the differential equation obtained from the mass balance:

$$\frac{dm_{WF}}{dt} = \dot{m}_{WF_{in}} - \dot{m}_{WF_{out}}. \quad (4.43)$$

4. Model of the Wall Wetting Dynamics based on Physics

Obviously, $\dot{m}_{WF_{in}}$ is the output of the droplet model and it represents the main connection between both subsystems. The value of $\dot{m}_{WF_{out}}$ is the output of the wall film model and can be estimated by assuming the behavior of the wall film. If no film flow can be assumed, only the evaporation process influences the mass transfer, namely $\dot{m}_{WF_{out}} = \dot{m}_{EVF}$. Otherwise we have to take into account the effect of the flowing liquid, namely $\dot{m}_{WF_{out}} = \dot{m}_{EVF} + \dot{m}_{flow}$.

4.5.2. Fuel Film Flow in the Intake

This part of the model has been introduced to take into account the effects of the shear stress on the fuel film surface. The shear stress causes dragging of the film towards the cylinder. This effect has been described as relatively important, in particular for cold engines [17].

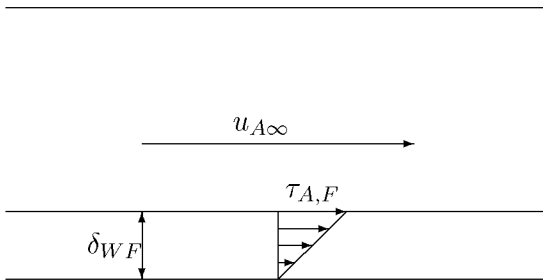


Figure 4.15: Drag effect on a liquid surface.

In order to describe the liquid flow characteristic, we have to make assumptions for the behavior of the gas flow in the duct. One important influence is given by the velocity profile of the fluid. In

4.5. Wall Film Evaporation

[33] the profile is described as:

$$u_F(y) = u_{F\infty} \cdot \left(\frac{y}{r_{in}} \right)^{m_c}, \quad (4.44)$$

where r_{in} is the radius of the duct, y is the direction perpendicular to the wall and m_c is a characteristic of the profile type. In particular, $m_c = 1$ describes a Couette flow, $m_c = 1/2$ describes a laminar flow and $m_c = 1/7$ describes a turbulent flow. The value of $u_{F\infty}$ represents an imaginary fluid velocity outside the boundary layer which has to be estimated.

Now we can calculate the shear stress on the surface with:

$$\tau_{Fs} = \mu_F \cdot \left. \frac{du_F}{dy} \right|_{y=\delta_{WF}} \quad (4.45)$$

With μ_F being the dynamic viscosity of the fluid. It can also be described with the kinematic viscosity, $\mu_F = \rho_F \cdot \nu_F$:

$$\tau_{Fs}(y) = \mu_F \cdot u_{F\infty} \cdot \frac{m}{r_{in}} \left(\frac{y}{r_{in}} \right)^{m_c-1}. \quad (4.46)$$

For the air at the liquid surface, the shear stress is given by:

$$\tau_{As} = \frac{C_f \cdot \rho_A \cdot u_{A\infty}^2}{2}, \quad (4.47)$$

with C_f being the friction coefficient. Confronting Equation 4.46 with Equation 4.47, the solution for the fluid velocity profile is obtained:

$$u_{F\infty} = \frac{r_{in}}{m_c} \cdot \left(\frac{\delta_{WF}}{r_{in}} \right)^{1-m_c} \cdot \frac{C_f}{\mu_F} \cdot \frac{\rho_A \cdot u_{A\infty}^2}{2}. \quad (4.48)$$

Equation 4.44 can be written as:

$$u_F(y) = \frac{r_{in}}{m_c} \cdot \left(\frac{\delta_{WF}}{r_{in}} \right)^{1-m_c} \cdot \frac{C_f}{\mu_F} \cdot \frac{\rho_A \cdot u_{A\infty}^2}{2} \cdot \left(\frac{y}{r_{in}} \right)^{m_c}. \quad (4.49)$$

4. Model of the Wall Wetting Dynamics based on Physics

Finally, the film flow mass is described by:

$$\dot{m}_{flow} = \rho_{Fl} \cdot \int_0^{\delta_{WF}} A_{flow}(y) \cdot u_F(y) \cdot dy, \quad (4.50)$$

where A_{flow} is given by:

$$A_{flow}(y) = \frac{\pi}{4} \cdot (d_{in}^2 - y^2). \quad (4.51)$$

The integral of Equation 4.50 over the thickness of the film yields the definitive mass flow:

$$\dot{m}_{flow} = \frac{C_f}{\mu_F} \cdot \frac{\rho_A \cdot \rho_{Fl}}{2} \cdot \frac{u_{A\infty}^2 \cdot \delta_{WF}^2}{m_c} \cdot \left(\frac{d_{in}^2}{m_c + 1} - \frac{\delta_{WF}^2}{m_c + 3} \right). \quad (4.52)$$

Now, the friction coefficient C_f has to be estimated. For this goal, the friction factor f is introduced:

$$C_f = \frac{f}{4}. \quad (4.53)$$

In order to estimate f , another analogy can be applied [33, 46], namely:

$$f = \frac{64}{Re_A}, \quad (4.54)$$

which is valid for a laminar flow. If the flow is turbulent then $f = 0.316 \cdot Re_A^{-0.25}$ [33].

For a fuel film flow under laminar conditions, i.e., $m_c = 1/2$, Equation 4.54 applies.

The equation for the laminar case is obtained from Equation 4.52 and Equation 4.54 after some algebra:

$$\dot{m}_{flowL} = \frac{42}{9} \cdot \rho_A \cdot \frac{\nu_A}{\nu_F} \cdot \frac{u_{A\infty} \cdot \delta_{WF}^2}{d_{in}} \cdot \left(\frac{2}{3} \cdot d_{in}^2 - \frac{2}{7} \cdot \delta_{WF}^2 \right). \quad (4.55)$$

4.5. Wall Film Evaporation

Note that the first factor in Equation 4.55 comes from the fact that the liquid flows only at opened intake valve, thus during 210° for every two engine rotation.

For the case of turbulent flow ($m_c = 1/7$), Equation 4.55 changes to:

$$\dot{m}_{flowT} = \frac{147}{144} \cdot \rho_A \cdot \frac{C_f}{\nu_F} \cdot u_{A\infty}^2 \cdot \delta_{WF}^2 \cdot \left(\frac{7}{8} \cdot d_{in}^2 - \frac{7}{22} \cdot \delta_{WF}^2 \right). \quad (4.56)$$

The practical experiments in Chapter 5 have shown though that the flowing mass \dot{m}_{flow} is much smaller than the evaporating mass flow \dot{m}_{EVF} . Moreover, the presence of the film flow slows down the calculation of the model remarkably. Due to the fact that the model-matching capability can be improved insignificantly, the flowing fuel will be neglected.

4.5.3. Assumption for the Wall Film Geometry

The wall wetting model for the fuel film is structured as depicted in Figure 4.14.

The wall film develops along the duct in front of the intake valves and covers homogeneously the duct. At this stage, the thickness of the film is assumed to be quasi-constant and is used as tuning parameter of the model:

$$\delta_{WF} \approx const. \quad (4.57)$$

The height of the film is the main state variable of the model. In fact, the total volume of this setup can be expressed as:

$$V_{WF} = \frac{\pi}{4} \cdot (d_{in}^2 - d_{WF}^2) \cdot h_{WF}. \quad (4.58)$$

4. Model of the Wall Wetting Dynamics based on Physics

Therefore, the total mass is calculated with:

$$m_{WF} = \rho_{Fl} \cdot V_{WF} = \frac{\pi}{4} \cdot \rho_{Fl} \cdot (d_{in}^2 - d_{WF}^2) \cdot h_{WF}, \quad (4.59)$$

where $d_{WF} = d_{in} - 2 \cdot \delta_{WF}$.

The dependency of the cylinder mass flow (evaporation only or both effects) on the size of the wall film is evident. Both Equation 4.42 and Equation 4.55 contain the parameter h_{WF} . In Equation 4.42, h_{WF} is contained in the area of the film A_{WF} which evaporates:

$$A_{WF} = \pi \cdot d_{WF} \cdot h_{WF}. \quad (4.60)$$

Note that this implies that the evaporative mass flow is dependent on the thickness of the film, although in a very weak way:

$$\frac{d_{WF}}{d_{in}} \simeq 1. \quad (4.61)$$

Equation 4.42 can be rewritten as:

$$\dot{m}_{EVF} = \pi \cdot \rho_{Fvs} \cdot D_{AB} \cdot Sh_F \cdot \ln(1 + B) \cdot h_{WF}. \quad (4.62)$$

This dependency is particularly interesting if we consider the case where no film flow can be assumed. In this case, a simple but effective formulation for A_P can be achieved. In fact, if we assume a mean value for the temperature and the air mass flow during one cycle, then:

$$\dot{m}_{EVF} = C_1 \cdot h_{WF}, \quad (4.63)$$

and

$$h_{WF} = C_2 \cdot m_{WF}, \quad (4.64)$$

with C_1 and C_2 constant. Assuming that the evaporation rate is constant too, the integral of Equation 4.63 with 4.64 yields:

$$m_{EVF} = C_1 \cdot C_2 \cdot m_{WF} \cdot \Delta, \quad (4.65)$$

4.5. Wall Film Evaporation

with Δ as the period of the cycle. Recalling Equation 4.38 we see that A_P can be expressed as follows:

$$A_P = 1 - \frac{120}{n} \cdot \frac{\rho_{Fvs}}{\rho_{Fl}} \cdot \frac{d_{WF}}{d_{in}} \cdot \frac{D_{AB} \cdot Sh_F \cdot \ln(1+B)}{d_{in}^2 - d_{WF}^2}, \quad (4.66)$$

and with the assumption in (4.61):

$$A_P = 1 - \frac{120}{n} \cdot \frac{\rho_{Fvs}}{\rho_{Fl}} \cdot \frac{D_{AB} \cdot Sh_F \cdot \ln(1+B)}{4 \cdot d_{in} \cdot \delta_{WF}}. \quad (4.67)$$

Alternative Wall Film Geometry

In the previous approach for the wall film geometry, the thickness of the film was supposed to remain constant or to vary slowly. This alternative approach assumes a simultaneous change in both of the values of the height h_{WF} and the thickness δ_{WF} .

The approach starts with the definition of the volume:

$$V_{WF} = \frac{\pi}{4} \cdot (d_{in}^2 - d_{WF}^2) \cdot h_{WF}. \quad (4.68)$$

Then with the assumption $\delta_{WF} \ll d_{in}$, the volume can be expressed as:

$$V_{WF} = \frac{\pi}{4} \cdot \underbrace{(d_{in}^2 - d_{in}^2)}_{=0} + 4 \cdot d_{in} \cdot \delta_{WF} + \underbrace{\delta_{WF}^2}_{\approx 0} \cdot h_{WF}. \quad (4.69)$$

A change in the volume yields:

$$\frac{V_{WF}}{V_{ref}} = \frac{h_{WF}}{h_{ref}} \cdot \frac{\delta_{WF}}{\delta_{ref}}. \quad (4.70)$$

A proportionality between changes in the height and in the thickness has to be assumed to determine the system of equation:

$$\frac{\delta_{WF}}{\delta_{ref}} = \left(\frac{h_{WF}}{h_{ref}} \right)^Z, \quad (4.71)$$

4. Model of the Wall Wetting Dynamics based on Physics

where Z is a proportionality constant. The change in volume can finally be expressed as:

$$V_{WF} = V_{ref} \cdot \left(\frac{h_{WF}}{h_{ref}} \right)^{Z+1}. \quad (4.72)$$

This leads to the final model:

$$\begin{aligned} \frac{dm_{WF}}{dt} &= \dot{m}_{WF_{in}} - \Xi \cdot (m_{WF})^{\frac{1}{1+Z}} \\ \dot{m}_{EVF} &= \Xi \cdot (m_{WF})^{\frac{1}{1+Z}} \\ \Xi &= \pi \cdot D_{AB} \cdot Sh_F \cdot \ln(1+B) \cdot h_{ref} \cdot (V_{ref} \cdot \rho_{Fvs})^{\frac{-1}{1+Z}}. \end{aligned} \quad (4.73)$$

This model is clearly nonlinear. Its tuning parameters are the reference states (volume, height, thickness) and the proportionality constant Z .

The disadvantage of such an approach is the increased complexity, in particular for the parametrization task (see Chapter 5). With this model, the matching performance can be increased, although not significantly (less than 1% by the tests in Chapter 5). The results of the optimization yielded for Z always very small values (e.g., $1.5 \cdot 10^{-5}$), which implies that the thickness is quasi-constant, thus confirming the assumption of Equation 4.57. The increased complexity in combination with the insufficient increased accuracy make this model less suitable for control purposes.

4.5.4. Main Dependencies and Tuning Parameters

In the wall film model, the main tuning parameter is represented by the thickness of the film δ_{WF} . Note that there is an engine speed dependency which is given by different aspects of the operating conditions of the engine.

4.5. Wall Film Evaporation

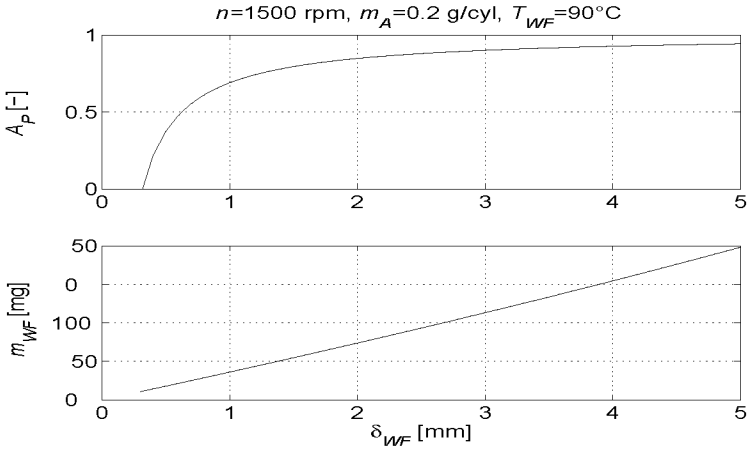


Figure 4.16: Dependency on the film thickness δ_{WF} .

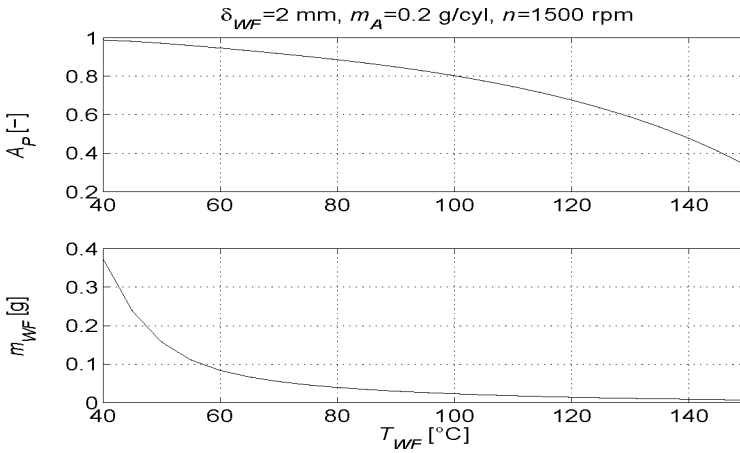


Figure 4.17: Dependency on the film temperature T_{WF} .

4. Model of the Wall Wetting Dynamics based on Physics

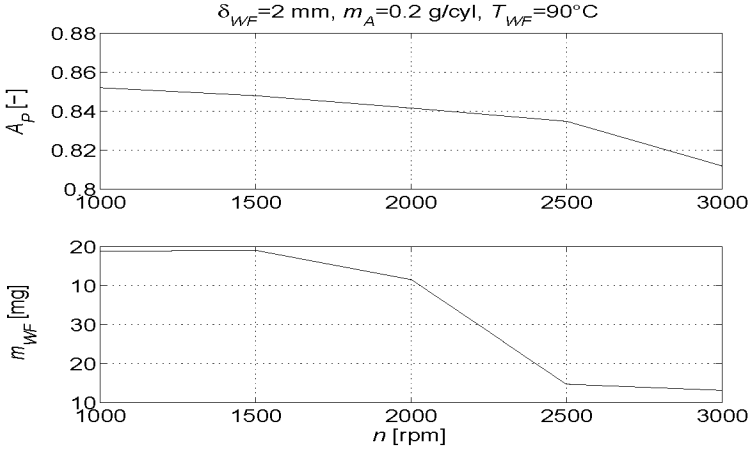


Figure 4.18: Dependency on the engine speed n .

The figure representing the engine speed dependency has only a few points because the identification of the impingement parameter B_P was performed only for a few engine speeds.

Actually, the most important dependency for a spark ignited engine is shown in Figure 4.19.

4.5. Wall Film Evaporation

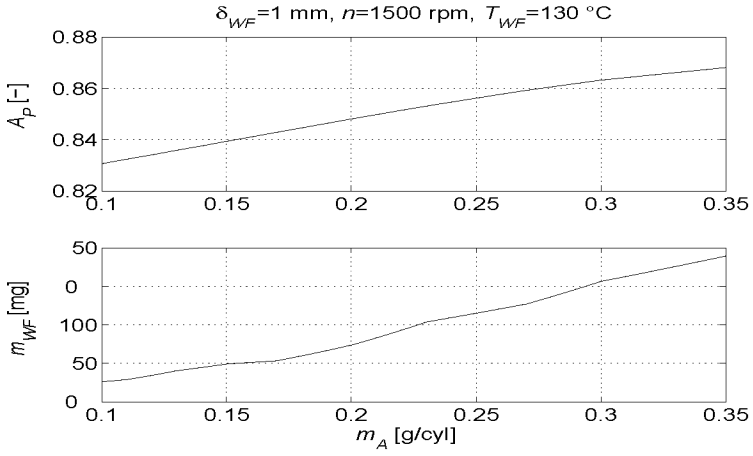


Figure 4.19: Dependency on the air mass flow.

4.6. Results of the Wall Film Model

As for the droplet model, the wall film model will be compared with the experimental results obtained by Simons [58]. Obviously the wall film cannot be isolated from the impingement part. Therefore, the results in this section include it as well.

4.6.1. Identified Parameters

The parameters which have been identified on a real engine showed a slowly increasing behavior in respect of the load. At low loads the gradient depends on the engine speed, while at high load this dependency fades.

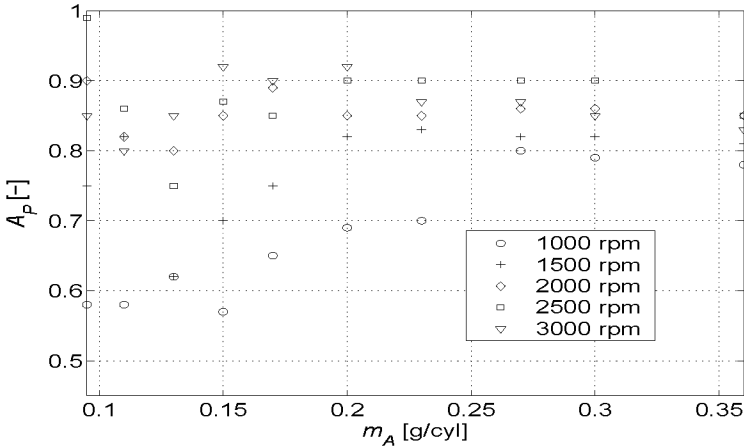


Figure 4.20: Identified parameters A_P .

4.6. Results of the Wall Film Model

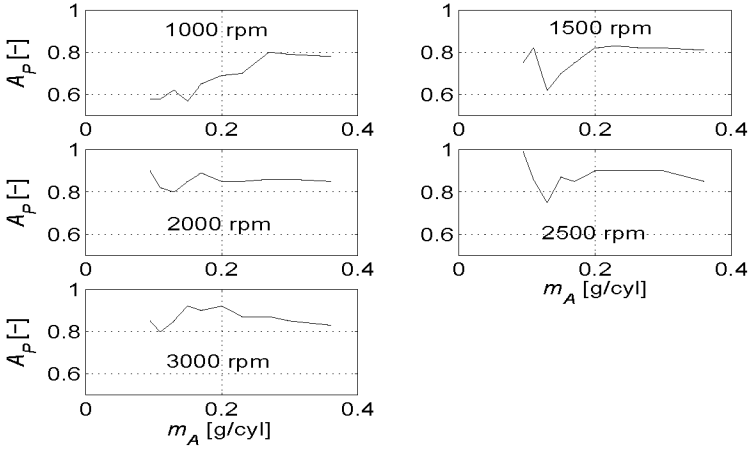
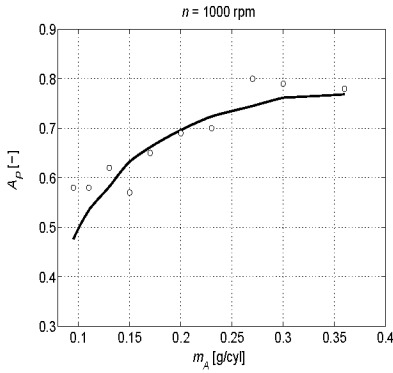


Figure 4.21: Identified parameters A_P .

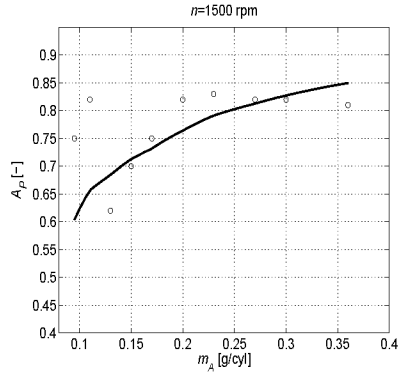
4.6.2. Comparison between Model-based Parameters and Simons' Parameters

The parameters identified by Simons are compared to the parameters that can be obtained by tuning the model. In the following figures, the behavior of the model for various engine speeds is shown. Note that the wall film thickness δ_{WF} is held constant for the same engine speed. The values are between 0.5 mm and 2 mm.

4. Model of the Wall Wetting Dynamics based on Physics

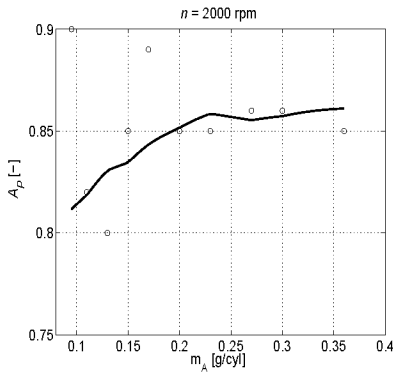


(a) Parameters at 1000 rpm.

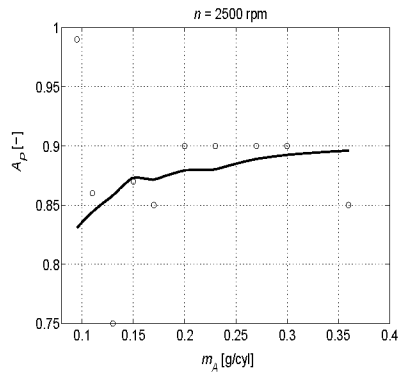


(b) Parameters at 1500 rpm.

Figure 4.22: Model results (-) compared with Simons' results (\circ).



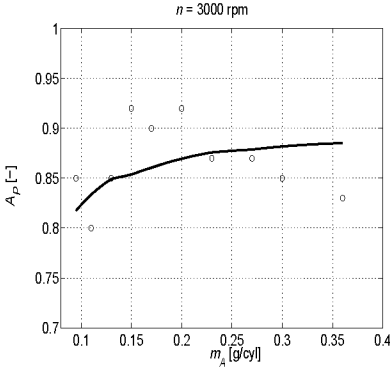
(a) Parameters at 2000 rpm.



(b) Parameters at 2500 rpm.

Figure 4.23: Model results (-) compared with Simons' results (\circ).

4.6. Results of the Wall Film Model



(a) Parameters at 3000 rpm.

Figure 4.24: Model results (-) compared to Simons' parameters (o).

As in the case of the droplet model, the results show a good match with the identified parameters. The temperature was not constant but had to be adapted to provide a good match.

However, the results are not so good as the results of the droplet model. On one hand, this has to do with the difficult identification related to the parameters A_P and B_P . In fact, A_P and B_P are identified simultaneously; some trade-offs are possible. On the other hand, nothing speaks against a dependency of the film thickness δ_{WF} on the operating conditions.

Furthermore, the identification results are less sensitive to A_P than to B_P [59]. This means that a relatively large error in the estimation of A_P has a small influence on the identification performance.

This effect is shown in all figures by the quite wild behavior of the identified parameters.

4.7. Temperature Model of the Intake Valve

For both models presented here the estimation of the temperature plays an important role: while for the droplet model, the temperature can be quasi measured with the available in-car sensors, for the film model the situation looks differently. In fact, the temperature of the film is influenced by various factors, last but not least by the temperature of the intake valves. Therefore, the temperature of the top of the valves and the temperature in the surroundings have to be considered in the modeling effort.

The purpose of this section is to calculate the intake valve temperature, which is relevant for the film temperature, and the intake duct temperature using the available measurements. The relation between these temperatures is given by an energy balance equation for both systems which form the intake valve-duct, i.e., the duct itself and the intake valve. Normally, there is a definite number of intake valves per cylinder dependent on the engine type. However, the system can be modeled like a cylinder with only one larger intake valve.

4.7.1. Physical Background

Heat Conduction

In a solid, conduction may be attributed to atomic activity in the form of lattice vibrations. The rate equation is known as Fourier's law and for the one-dimensional plane wall with a temperature distribution $T(x)$, it is expressed as

$$\dot{q} = k_q \frac{dT}{dx}, \quad (4.74)$$

4.7. Temperature Model of the Intake Valve

where \dot{q} is the heat flux per unit of area [$\frac{W}{m^2}$]. Under steady-state conditions, the temperature distribution is linear. The thermal conductivity k_q is a characteristic of the material of the wall.

Heat Convection

The term “heat convection” describes energy transfer between a surface and a fluid moving over the surface. When the motion of the fluid is produced by forces other than gravity, the term “forced convection” is used [30, 33].

The heat flux transferred to a solid surface at temperature T_w from a flowing fluid stream at temperature T_A is determined by the heat transfer coefficient h from the relationship:

$$\dot{q} = h_q(T_A - T_w). \quad (4.75)$$

The Nusselt number is equal to the dimensionless temperature gradient at the surface, and it provides a measure of the convection heat transfer occurring at the surface. It is defined as:

$$Nu = \frac{h_q \cdot d}{k}, \quad (4.76)$$

where d is a characteristic length of the system. For many flow geometries (such as flow through pipes or over a plate), the following Reynolds analogy holds:

$$Nu = C_h \cdot Re^{m_h} Pr^{n_h}, \quad (4.77)$$

where C_h, m_h, n_h are constants which depend on the geometry. The Reynolds number tells if the boundary layer is laminar or turbulent. With the relation $\dot{m} = \rho_A u_\infty A$ the Reynolds number can be related to the mass-flow rate \dot{m} :

$$Re = \frac{\dot{m}d}{\mu A}, \quad (4.78)$$

4. Model of the Wall Wetting Dynamics based on Physics

where μ is the flow viscosity.

For gases, the Prandtl number varies little [33] and can be assumed as constant, thus Equation 4.77 can be rewritten as:

$$Nu = C_h \cdot Re^{m_h}. \quad (4.79)$$

Finally, we can calculate the heat-transfer rate with the following relation:

$$\dot{Q} = h_q A (T_A - T_W) = \frac{Nu \cdot k_q}{d} \cdot A \cdot (T_A - T_W). \quad (4.80)$$

4.7.2. Intake-Valve Thermal Balance

The transient conservation of energy applied to the body of the intake valve (see [2], [15], [16], and [43]) is shown schematically in Figure 4.25.

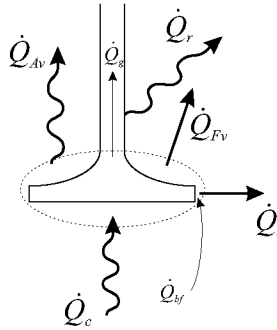


Figure 4.25: Energy flow through the intake valve.

Separating the heat transfer processes according to their direction (i.e., in or out of the valve), the heat transfer processes into the intake valve are:

4.7. Temperature Model of the Intake Valve

- Heat transfer from combustion-chamber gases during the closed intake valve period \dot{Q}_c .
- Heat transfer from combustion-chamber gases, which back flow into the intake port during the valve overlap period \dot{Q}_{bf} .

The heat transfer processes out of the intake valve are:

- Convective heat transfer to the air flowing over the valve during the intake process \dot{Q}_{Av} .
- Conduction heat transfer through the valve seat during the closed intake valve period \dot{Q}_s .
- Conduction heat transfer through the valve guide \dot{Q}_g .
- Fuel spray cooling via heat conduction and evaporation during the injection and fuel evaporation period \dot{Q}_{Fv} .
- Radiation from the valve \dot{Q}_r .

Mathematically, the change of stored energy in the valve can be interpreted as the variation of the valve temperature T_v as:

$$m_v c_v \frac{dT_v}{dt} = \dot{Q}_c + \dot{Q}_{bf} - [\dot{Q}_s + \dot{Q}_{Av} + \dot{Q}_{Fv} + \dot{Q}_g + \dot{Q}_r], \quad (4.81)$$

where m_v is the mass of the valve and c_v its specific heat. According to [15], the heat flux from the back-flow and that into the valve guide are so small compared with the heat flux into the valve seat that they can be neglected. As the valve is usually wetted, the radiation is small too (see [16]). Equation 4.81 simplifies to:

$$m_v c_v \frac{dT_v}{dt} = \dot{Q}_c - [\dot{Q}_s + \dot{Q}_{Av} + \dot{Q}_{Fv}]. \quad (4.82)$$

4. Model of the Wall Wetting Dynamics based on Physics

The models for the different heat flows are developed taking into account the main dependencies.

Heat Transfer From the Combustion Gases (\dot{Q}_c)

The prime driver of this heat-transfer problem is the energy convected to the intake valve from the combustion gases. Intuitively, one can relate the heat-transfer rate to the operating conditions of the engine, i.e., the energy convected to the valve will vary mainly as a function of engine speed and load. Since no sensor is available in the cylinder to measure the combustion-chamber pressure or temperature, this function can be expressed in a very simple way using the Reynolds analogy:

$$\dot{Q}_c = \frac{Nu \cdot k_c}{L} A_v (T_c - T_v) = \frac{C Re_c^{x_c} \cdot k_c}{L} A_v (T_c - T_v). \quad (4.83)$$

Assuming constant fluid and material properties and also a constant temperature difference between combustion gases and intake valve, the only parameter that remains variable is the mass-flow rate contained in the Reynolds number. The rest is collected in the constant C_c . Thus, Equation 4.83 can be written as follows:

$$\dot{Q}_c = C_c \cdot (\dot{m}_F + \dot{m}_A)^{x_c}. \quad (4.84)$$

According to [1] the combustion exponent x_c is set to 0.54, while the combustion constant C_c is set to $2857 \frac{m^2}{s^2}$. The mass-flow rate of fuel and air to the combustion chamber is a representative quantity because it is both proportional to the engine speed (higher speed means more cycles per second) and to the load (more load means higher intake-manifold pressure).

4.7. Temperature Model of the Intake Valve

Heat Conduction Through the Intake Valve Seat (\dot{Q}_s)

A great part of the heat stored in the intake valve flows towards the cooling medium through the seat of the intake valve. A good thermal coupling between the cooling medium and the pipe where it flows is assumed, i.e., the temperature of the cooling medium and that of the pipe wall are assumed to be the same. Another assumption regards the thermal contact resistance of the junction of intake valve and valve seat. In effect, depending on the pressure in the combustion chamber, the valve is pushed against its seat by a different force in every different operating point. Since the pressure in the combustion chamber cannot be measured in normal engines, one can use the intake-manifold air pressure p_I instead (which is normally used to define the load of an engine) and assume that the pressure in the cylinder is direct proportional to p_I . Thus the heat-transfer rate can be calculated as:

$$\dot{Q}_s = C_s \cdot A_s \cdot p_I \cdot (T_v - T_{cool}), \quad (4.85)$$

where T_{cool} is the temperature of the cooling medium, A_s the area of the valve's seat and d_s the distance between the intake valve border and the cooling-medium duct. The parameter C_s is an experimentally fitted constant ($C_s = 4580 \frac{\text{m}}{\text{s}\cdot\text{K}}$).

Effect of the Air Flow (\dot{Q}_{Av})

The air flow in the inlet helps to cool down the back surface of the valve. The heat transfer occurs through convection, thus the Nusselt number has to be calculated from Equation 4.79 as:

$$Nu_{Av} = C_{Av} \cdot Re_{Av}^{x_{Av}}. \quad (4.86)$$

4. Model of the Wall Wetting Dynamics based on Physics

Further experiments [20] have shown that the exponent x_{Av} varies depending on the inclination angle of the valve-port. In the specific case of this thesis, the inclination angle is about 30° and hence $x_{Av} = 0.5$ and $C_{Av} = 0.868$. The convective heat-transfer rate from the intake valve to the fresh air is the same as Equation 4.80 and more precisely:

$$\dot{Q}_{Av} = \frac{Nu_{Av} \cdot k_A}{d_{in}} \cdot A_v \cdot (T_v - T_{Av}), \quad (4.87)$$

where T_{Av} is the temperature of the air-fuel mixture leaving the intake valve-duct and flowing over the intake valve into the combustion chamber, while k_A is the thermal conductivity of air.

Fuel Evaporating from the Intake Valve Surface (\dot{Q}_{Fv})

Liquid fuel is injected on the back surface of the intake valve to promote its evaporation, because the valve surface is hotter than the port walls. The fuel has a large cooling effect on the valve, both through heating (raising the fuel temperature to the valve temperature) and through the enthalpy of vaporization $H_{F,ev}$. The energy transferred to the fraction of liquid fuel ξ_y which reaches the valve surface can thus be calculated as:

$$\dot{Q}_{Fv} = \xi_y \cdot \dot{m}_{Finj} \cdot [(T_v - T_{Av}) c_{pF} + H_{F,ev}], \quad (4.88)$$

where c_{pF} is the specific heat of fuel. The Figure 4.26 shows how the ratio between these heat fluxes behaves during a warm-up phase with constant engine speed and constant manifold pressure.

4.7. Temperature Model of the Intake Valve

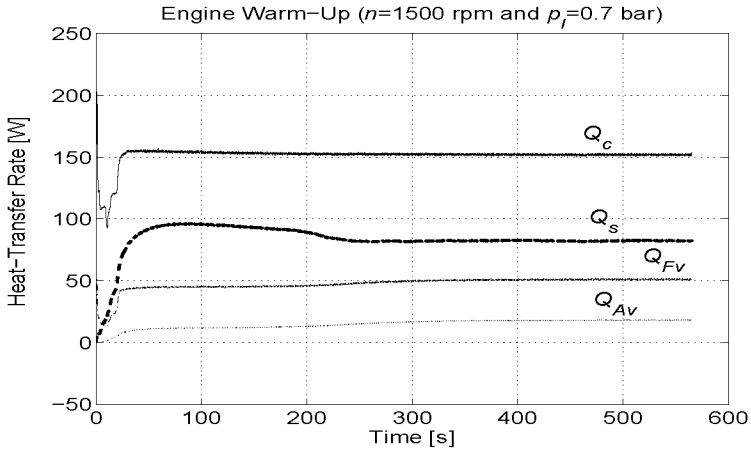


Figure 4.26: Behavior of the heat fluxes by a warm-up phase.

4.7.3. Intake-Valve Duct Thermal Balance

As first approach, the intake-valve duct can be described by a cylindrical pipe with inlet and outlet temperatures as in Figure 4.27.

4. Model of the Wall Wetting Dynamics based on Physics

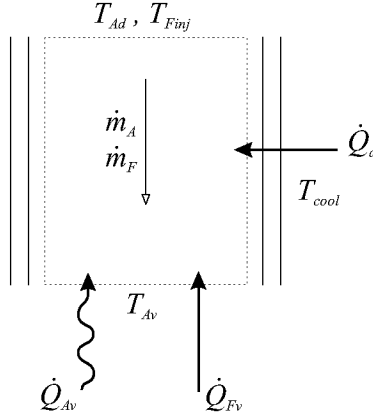


Figure 4.27: Energy balance of the intake-valve duct.

It is assumed that the air traveling through the intake valve-duct is heated only by the cooling medium and by the heat coming from the intake valve. The general energy balance equation for this situation is given by:

$$\frac{d(E_A + E_F)}{dt} = [\dot{H}_{A,in} + \dot{H}_{F,in}] - [\dot{H}_{A,out} + \dot{H}_{F,out}] + \dot{Q}_d + \dot{Q}_{Av} + \dot{Q}_{Fv}, \quad (4.89)$$

where E_A and E_F are the internal energies in the control volume of air and fuel, respectively. The \dot{H}_i are enthalpy fluxes and \dot{Q}_d is the heat transferred to the air by the cooling medium. The heat exchange expressed by \dot{Q}_{Av} and \dot{Q}_{Fv} has already been calculated in Section 4.7.2. The system can be assumed stationary, i.e., the variation in the internal energy of the air-fuel mixture is set to zero. With this assumption and replacing the enthalpy transfer

4.7. Temperature Model of the Intake Valve

rates with:

$$\begin{aligned}\dot{H}_{Ain} + \dot{H}_{Fin} &= \dot{m}_{ACpA}T_{Ad} + \dot{m}_{FCpF}T_{Finj} \\ \dot{H}_{Aout} + \dot{H}_{Fout} &= \dot{m}_{ACpA}T_{Av} + \dot{m}_{FCpF}T_{Av}\end{aligned}\quad (4.90)$$

Equation 4.89 becomes:

$$\dot{m}_{ACpA}\Delta T_{Ad} + \dot{m}_{FCpF}\Delta T_{Finj} + \dot{Q}_d + \dot{Q}_{Av} + \dot{Q}_{Fv} = 0, \quad (4.91)$$

where

$$\begin{aligned}\Delta T_{Ad} &= T_{Ad} - T_{Av} \\ \Delta T_{Finj} &= T_{Finj} - T_{Av}.\end{aligned}\quad (4.92)$$

Note that the dynamics of the system intake valve and intake duct is given by the intake valve alone.

Heat Transfer from the Cooling Medium

The heat flux transferred from the cooling medium through the intake valve duct wall to the intake air can be modeled as constant along all the duct length L_d . The mean air temperature over the whole duct is necessary to calculate the heat-transfer rate, which is:

$$\dot{Q}_d = U\pi d_{in}L_d \left(T_{cool} - \frac{T_{Ad} + T_{Av}}{2} \right), \quad (4.93)$$

where U is the overall heat transfer coefficient defined in terms of the inside area of the intake duct:

$$U = \frac{1}{\frac{1}{h_{Ad}} + \frac{d_{in}}{2k_d} \ln \left(\frac{d_{in} + \delta_d}{d_{in}} \right)}. \quad (4.94)$$

4. Model of the Wall Wetting Dynamics based on Physics

The heat transfer coefficient h_{Ad} is calculated from the definition of the Nusselt number:

$$h_{Ad} = \frac{Nu_{Ad} \cdot k_A}{L_d}. \quad (4.95)$$

Since the Reynolds number of the intake air flow:

$$Re_{Ad} = \frac{\dot{m}_A \cdot d_{in}}{\mu_A \cdot A_d} = \frac{4 \cdot \dot{m}_A}{\mu_A \cdot \pi \cdot d_{in}}, \quad (4.96)$$

turns out to exceed the critical Reynolds number, i.e., $Re_{Ad} > 2300$, the flow can be considered turbulent. Moreover, considering that the hydrodynamic entry length L_d is about 10 times the duct diameter, a fully developed turbulent flow can be assumed [33]. Hence, the Nusselt number is calculated with:

$$Nu_{Ad} = 0.021 \cdot Re_{Ad}^{0.8} \cdot Pr^{0.42}. \quad (4.97)$$

Figure 4.28 shows the warm-up temperatures for the intake valve and the coolant fluid.

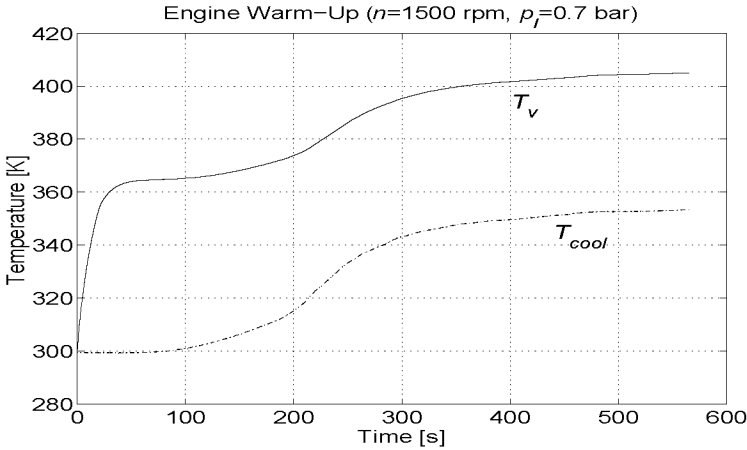


Figure 4.28: Temperature behavior during the engine warm-up.

4.7. Temperature Model of the Intake Valve

The first rapid increase of T_v is due to the heat released by the combustion, the second slower increase is caused by the reduced heat transfer to the coolant because of the increased T_{cool} .

4.8. Discussion

The model presented in this chapter fulfils the requirements for which it was developed: Its structure is sufficiently simple to be used for control purposes. Actually it is the same structure as the Aquino model. The linear parameters have a good agreement with the identification results. And the tuning of this model is as simple as with the Aquino model. Moreover, extrapolation capabilities are included, in particular by changing the temperature. However, it is important to remark that though this model contains a lot of information on the physics of the wall wetting system, it is a phenomenological model. This means that the parameters of the model do not have a strict physical meaning. For instance, a value of δ_{WF} cannot be compared with the real thickness of the fuel film which could be measured with optical methods (e.g., in [29]).

The real improvement lies in the fact that this model is able to follow changes in the single operating condition up to the extrapolation of non-measured operating conditions and to reduce the number of parameters to be measured or identified. For instance, the impact time constant τ_{DA} could be held constant when comparing the results of the droplet model with the identification results of Simons. This fact is promising for the goal of reducing the number of measurements to be made. The thickness of the film instead, does not appear to be constant, however, its value should remain within a small range.

The next chapter investigates the actual tuning of these parameters by means of off-line and on-line identification methods.

5. Identification of the Wall Wetting Parameters

5.1. Introduction

After having introduced the model in detail, an efficient method for the identification of its parameters has to be chosen. The main procedures for parameter identification are divided into off-line and on-line methods. Off-line methods are particularly interesting for the identification of the parameters that are constant for a long period of time and are the same for the most operating points. The parameter that is most important to be identified off-line is therefore the impact time constant τ_{DA} (Equation 4.26). On-line methods are useful in case of parameters which are not constant over time and not the same in every operating point which change slowly.

This chapter is divided into two sections:

The first section describes the off-line identification procedure, where the wall wetting parameters are identified on the basis of measurements on the test bench. The second section describes the on-line method, that is Kalman filter, which was used to identify the wall film parameters and the internal state variables of the wall film, such as the wall wetting fuel mass.

The results of the model are compared with the results of a simple Aquino approach which is parameterized on the same measure-

5. Identification of the Wall Wetting Parameters

ments. For practical reasons, from now on the nonlinear model will be called WW-model, while the Aquino model will be called Aq-model.

5.2. Off-Line Optimization

5.2.1. Starting Point

Before starting the optimization, the parameters which are not considered tuning parameters, are pre-set. Moreover, the following assumptions are made:

- The intake manifold dynamics is assumed to be known, with the exception of a freely tunable gain factor k_A .
- The wall film temperature is calculated with the temperature model (Section 4.7).
- The exhaust gas dynamics is assumed to be known, i.e., the residual gas fraction C , the delay δ_{delay} , and the dynamics of the λ -sensor are known.

The main tuning parameters for the WW-model are represented by the time constant of the impact model (τ_{DA}), the temperature of the droplet (T_D), and by the wall film thickness (δ_{WF}) as listed in Table 5.1.

Table 5.1: Parameters to optimize in the WW-model.

Parameters:	Description:
k_A	Gain for the estimation of the air mass flow
τ_{DA}	Droplet time constant
δ_{WF}	Thickness of the fuel film
T_D	Droplet temperature

5. Identification of the Wall Wetting Parameters

The parameters to be investigated for the optimization of the Aq-model are two: the impingement and the evaporation parameter (see Equation 4.35).

Table 5.2: Parameters to optimize in the Aq-model.

Parameters:	Description:
k_A	Gain for the estimation of the air mass flow
A_P	Evaporation parameter
B_P	Impingement parameter

5.2.2. Off-Line Method

The off-line investigation has two goals. First of all, the assumption made in Section 4.3.3 about the behavior of the characteristic impact time constant τ_{DA} has to be verified. Second, the behavior of the thickness of the film δ_{WF} and of the droplet temperature T_D have to be studied to eventually detect specific trends.

The off-line optimizations are performed with an algorithm implemented in Matlab, `lsqnonlin`. The algorithm solves problems of the form:

$$\min_{\theta} \left(\sum_{n=0}^N f(X_n)^2 \right), \quad (5.1)$$

where X_n and the values returned by $f(X_n)$ can be vectors or matrices. The function $f(X_n)$ can obviously be a nonlinear function, for the algorithm is particularly suited for nonlinear optimizations. The function to be minimized is the difference between model and experiments in every time step t_n :

$$f(X_n) = \text{Error}(t_n) = \lambda_{real}(t_n) - \lambda_{model}(t_n) \quad (5.2)$$

5.2. Off-Line Optimization

The algorithm permits to set limits for the range of identification of the parameters. For this specific problem, the limits can be set quite precisely, for the parameters must remain in a specific range to maintain some physical meaning.

In order to test the model appropriately, the experiments are performed on the engine operated with two extreme coolant temperatures, a very cold temperature and the normal, warmed-up engine temperature.

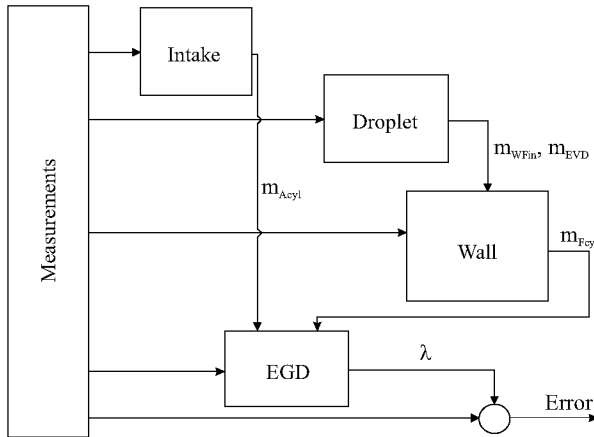


Figure 5.1: Model setup for off-line optimizations.

5.2.3. Description of the Experiments

To excite the wall wetting system, various experiments are performed:

First, the behavior of the system is tested for the engine map of Table 5.3 with a fuel injection modulation and a constant air mass flow to reduce any possible error in the air estimation.

5. Identification of the Wall Wetting Parameters

Table 5.3: Engine map for the optimization (measured points).

Experiment	Lower load	Upper load	Engine speed.
1–5	0.1 g/cyl	0.3 g/cyl	1000 rpm
6–10	0.1 g/cyl	0.3 g/cyl	1500 rpm
11–15	0.1 g/cyl	0.3 g/cyl	2000 rpm
16–20	0.1 g/cyl	0.3 g/cyl	2500 rpm
21–25	0.1 g/cyl	0.3 g/cyl	3000 rpm

Second, the system is tested with a complete throttle tip-in and tip-out, which represents the usual problem in a normal driving situation.

Table 5.4: Tip-in/tip-out experiments.

Experiment	Descriptions	Boundary Cond.
1	Tip-in/tip-out	$0.2 \pm 30\%$ g/cyl, 1500 rpm
2	Tip-in/tip-out	$0.2 \pm 50\%$ g/cyl, 1500 rpm
3	Tip-in/tip-out	$0.15 \pm 30\%$ g/cyl, 1500 rpm
4	Tip-in/tip-out	$0.2 \pm 30\%$ g/cyl, 2000 rpm
5	Tip-in/tip-out	$0.2 \pm 30\%$ g/cyl, 2500 rpm

Finally, the system is tested with steps for the air mass flow with constant injection times, to check its sensitivity to the air mass flow (Figures 5.7–5.8).

The results for both the Aq-model and the WW-model are depicted in the Figures 5.2–5.10.

The curves represent the values of the A/F ratio measured in the exhaust pipe, that is, the exhaust gas dynamics are included.

Results of the WW-Model

Figure 5.2 shows a typical result of the optimization of the model parameters by fuel injection modulation for a warmed-up engine. In this case, the estimation of the air mass flow into the cylinder is simple, because it can be directly measured with the air mass flow sensor. It is evident that the model can match the trace of the A/F ratio very well. This was expected, given the remark made in [58] that assumes the Aquino parameters to be dependent on the load of the engine (air mass flow) and on the temperature only.

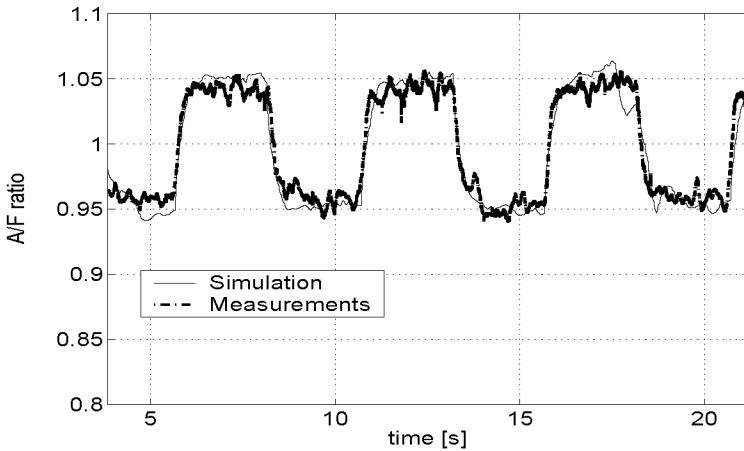


Figure 5.2: A/F ratio for the warmed-up engine (85°C), fuel injection modulation.

The wall wetting effects are usually more evident in a cold engine, because of the fact that the evaporation of the fuel strongly depends on the temperature. An example of an optimization result

5. Identification of the Wall Wetting Parameters

for a cold cold engine is depicted in Figure 5.3.

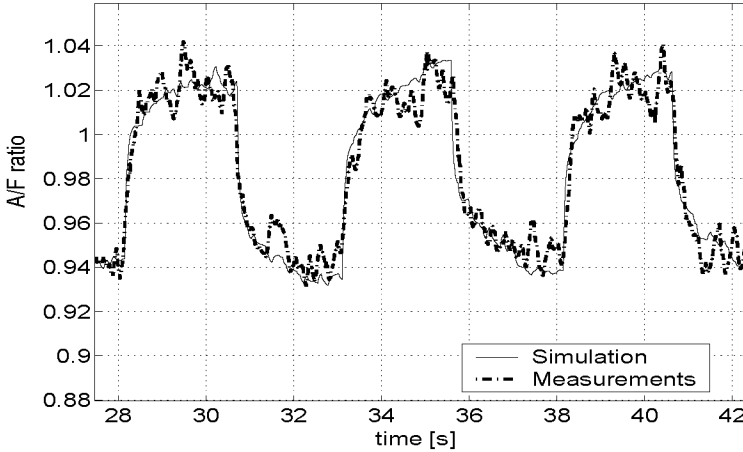


Figure 5.3: A/F ratio for the cold engine (35°C), fuel injection modulation.

For cold and warmed-up conditions, the resulting parameters of the engine map of Table 5.3 are depicted in Figure 5.4. There are two interesting aspects of these results, namely the behavior of the film thickness δ_{WF} and the behavior of the droplet temperature T_D .

5.2. Off-Line Optimization

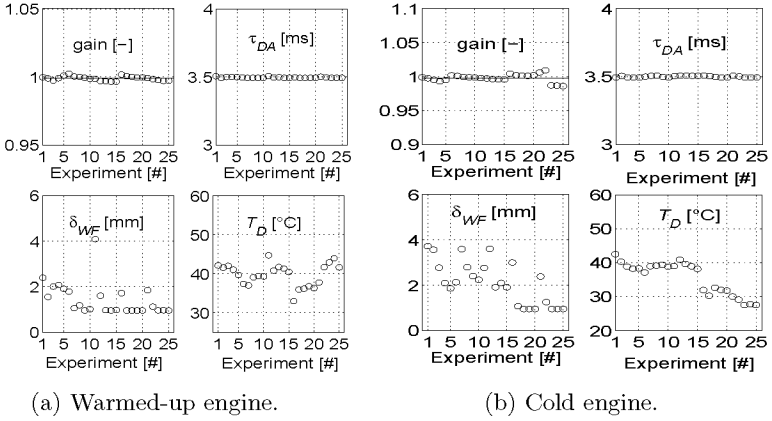


Figure 5.4: Resulting parameters of the off-line identification.

The droplet temperature seems to be independent on the load of the engine and on the engine speed, at least for low engine speeds, while the fuel thickness is inversely proportional to the air mass flow.

Figure 5.5 and Figure 5.6 show typical results of the optimization of the tip-in and tip-out for a warmed-up and a cold engine. The results have been obtained by holding the impact time constant τ_{DA} at the value identified by the fuel injection modulation experiments and optimizing the other parameters.

5. Identification of the Wall Wetting Parameters

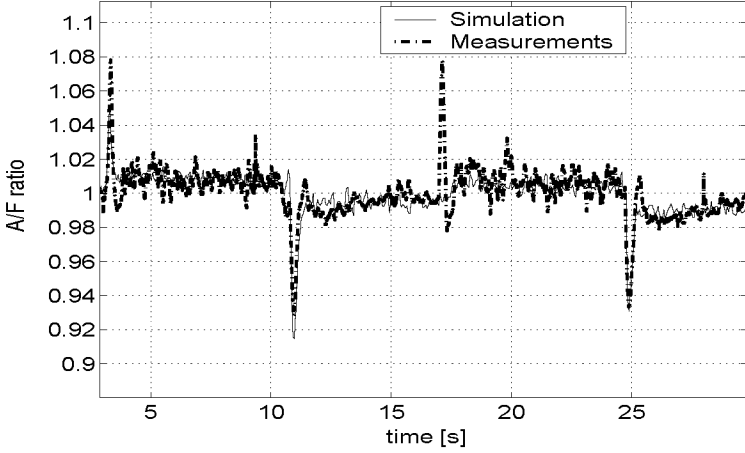


Figure 5.5: A/F ratio for the warmed-up engine (85°C), tip-in followed by a tip-out.

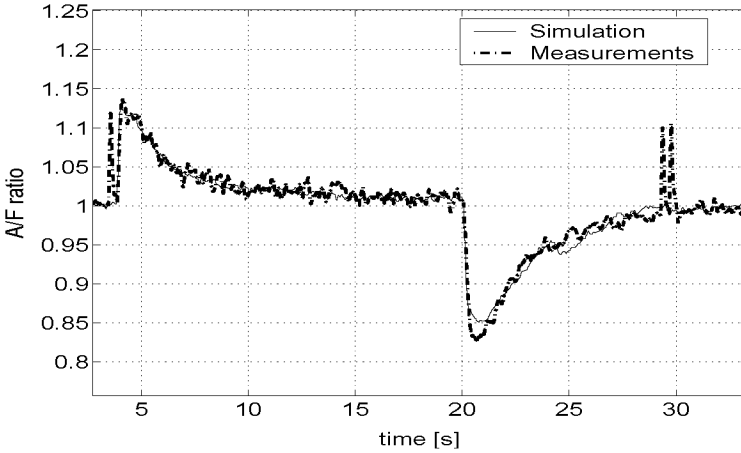


Figure 5.6: A/F ratio for the cold engine (35°C), tip-in followed by tip-out.

5.2. Off-Line Optimization

In this case, the wall wetting effects are modeled as well as in the previous, simpler case. There are cases where these results were difficult to obtain even with a very detailed model [28].

By looking closely at the curves in the transient phase, a certain imprecision can be spotted. The suspected reason is an imperfect estimation of the influence of the air mass flow on the evaporation. The experiments with the air mass flow modulation may help to verify this hypothesis.

The results with air mass flow modulation are indeed quite interesting. In fact, this kind of event does not occur in normal operations. A couple of examples of the results are depicted in the Figures 5.7–5.8.

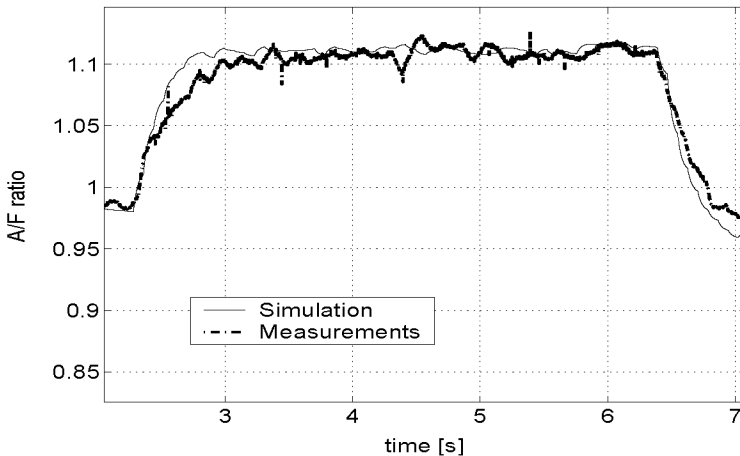


Figure 5.7: A/F ratio for the warmed-up engine (85°C), air mass excitation.

5. Identification of the Wall Wetting Parameters

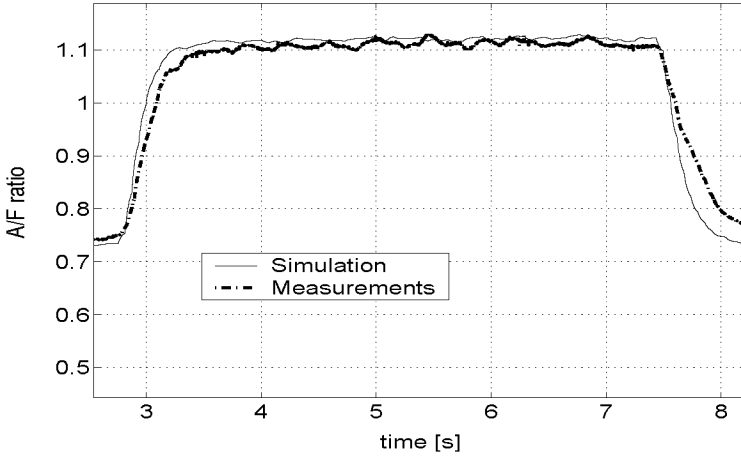


Figure 5.8: A/F ratio for warmed-up engine (85°C), air mass excitation.

While by fuel injection modulation and by tip-in/tip-out experiments the results were excellent, in these experiments the results show a lack of precision. So there is a slight discrepancy between the real and the modeled influence of the air mass flow into the cylinder. However, the error is quite limited, in particular for the tip-in/tip-out events.

Results of the Aq-Model

The same experiments are replicated with the Aq-model. In Figures 5.9–5.10 the results of the optimization of the parameters of the Aq-model are depicted. As expected, the experiments with constant air mass flow (Figure 5.9) yield almost the same very good results as the WW-model or even better. The results for

tip-in/tip-out experiments are slightly worse.

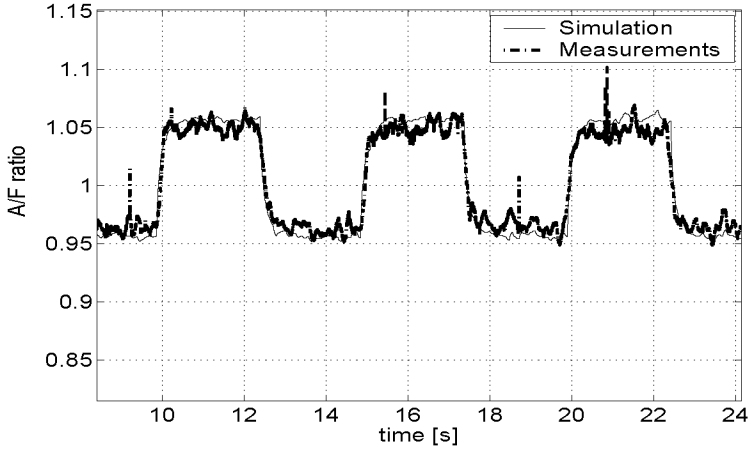


Figure 5.9: A/F ratio for the warmed-up engine (85°C), fuel injection modulation.

5. Identification of the Wall Wetting Parameters

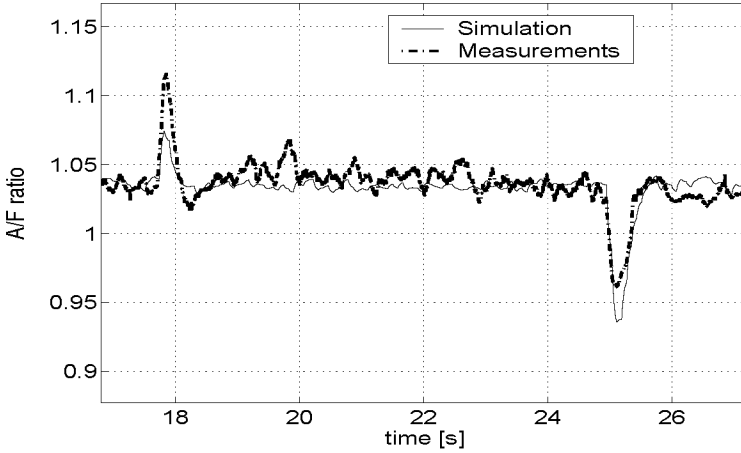


Figure 5.10: A/F ratio for the warmed-up engine (85°C), tip-in followed by tip-out.

Aq-Model vs. WW-Model

Visually, it is not very easy to compare the performances of the WW-model with the Aq-model. For this reason, the residuum of the optimizations (Equation 5.3) is considered for every operating point described in Table 5.3 and for the experiments described in Table 5.4.

$$\text{Residuum} = \sum_0^{t_{\text{end}}} (\lambda_{\text{measurements}} - \lambda_{\text{simulation}})^2. \quad (5.3)$$

The residuum for every operating point is plotted in the Figures 5.11–5.12.

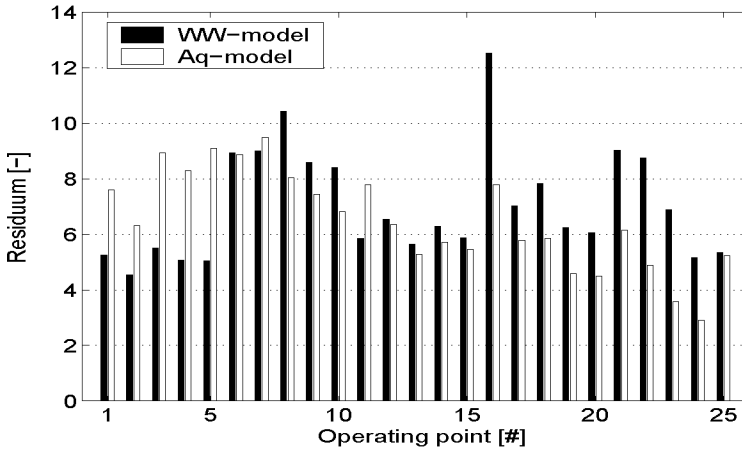


Figure 5.11: Residuum of the optimizations for the warmed-up engine (Experiments of Table 5.3).

Figure 5.11 shows clearly that the Aq-model gives slightly better results than the WW-model for the majority of the fuel injection modulation experiments. In some experiments (1–5), the WW-model was clearly better, while in experiments 16, 18, and 21–23 it was clearly worse.

5. Identification of the Wall Wetting Parameters

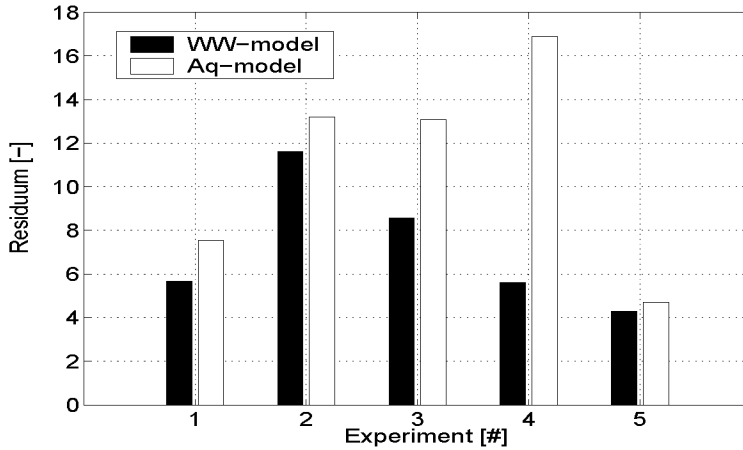


Figure 5.12: Residuum of the optimizations for the warmed-up engine (Experiments of Table 5.4).

However, for the tip-in/tip-out experiments (Figure 5.12), the WW-model yielded significantly better results than the Aq-model. Due to the fact that these events represent the major problem for the compensator by normal operating condition, the main goal is achieved.

5.3. On-Line Optimization

Due to the fact that the currently known impact time constant τ_{DA} is the same for all operating points and that the droplet temperatures have already been identified off-line, half of the wall wetting dynamics are known. The rest, i.e., the parameters and the state variables of wall film dynamics, have to be estimated on-line.

There exist various methods for the on-line estimation of model parameters. Among them, the maximum-likelihood method with all its related algorithms, such as least-square, instrumental variables, etc., can be used. The prediction error method was applied for the wall wetting system in [58] with appreciable results. In this work, however, the development of an extended Kalman filter was preferred [64] because it permits the estimation of the state variables of the wall film along with the unknown parameters (e.g., δ_{WF}).

5.3.1. Kalman Filter

One of the best known methods to estimate the non-measurable state variables of a dynamic system is the filter by Kalman. The Kalman filter was initially designed for systems which can be described by linear differential equations expressed in state-space form, when the measurements are linearly dependent on the state variables. In most realistic problems, the systems have to be described by nonlinear differential equations. To cope with these situations, the theory of the Kalman filter was extended. This extension permitted interesting new advantages, like the estimation of system parameters.

5. Identification of the Wall Wetting Parameters

Theory of the Extended Kalman Filter (EKF)

Consider the state-space representation of the nonlinear time-varying process:

$$\begin{aligned}\dot{x}(t) &= f(x(t), u(t), t) + v \\ y(t) &= g(x(t), u(t), t) + r,\end{aligned}\tag{5.4}$$

where v and r are the process and the measurement noise, respectively, with autocovariance matrices $Q = E\{vv^T\}$ and $R = E\{rr^T\}$, which are supposed to be independent from each other and have only diagonal elements. For a second order system with two outputs, for example:

$$Q = \begin{bmatrix} \phi_1 & 0 \\ 0 & \phi_2 \end{bmatrix}, \quad R = \begin{bmatrix} r_1 & 0 \\ 0 & r_2 \end{bmatrix}.\tag{5.5}$$

To obtain the linear system matrices, the process has to be linearized in every operating point for every time step:

$$\begin{aligned}A &= \left. \frac{\partial f(x,u)}{\partial x} \right|_{x=\hat{x}} & B &= \left. \frac{\partial f(x,u)}{\partial u} \right|_{x=\hat{x}} \\ C &= \left. \frac{\partial g(x,u)}{\partial x} \right|_{x=\hat{x}} & D &= \left. \frac{\partial g(x,u)}{\partial u} \right|_{x=\hat{x}},\end{aligned}\tag{5.6}$$

where \hat{x} is the filter estimation of the states. The transition matrix Φ_k for the discrete Riccati equation is obtained by a Taylor-series expansion for e^{AT_s} :

$$\Phi_k \approx \text{Taylor}(A) \approx I + AT_s,\tag{5.7}$$

or it can eventually be expressed with the bilinear approximation:

$$\Phi_k \approx \left[I - A \frac{T_s}{2} \right]^{-1} \left[I + A \frac{T_s}{2} \right].\tag{5.8}$$

5.3. On-Line Optimization

The discrete output of the process can be represented as:

$$y_k = H_k x_k + r_k, \quad (5.9)$$

where $H_k = C$.

An alternative way to linearize the system and to express the state-space matrices is to approximate the partial derivatives of the state equations calculating their mean slope in every cycle (Figure 5.13). The matrix Φ_k is then approximated as:

$$\Phi_k \approx \text{Tay} \left(\frac{\partial f(x_k, u_k)}{\partial x_k} \right) \approx \text{Tay} \left(\frac{f(x_{k+1}, u_k) - f(x_k, u_k)}{x_{k+1} - x_k} \right). \quad (5.10)$$

This method has an evident disadvantage: if the state variable is nearly constant, the elements of the matrix Φ_k go to infinity. This method was thus discarded.

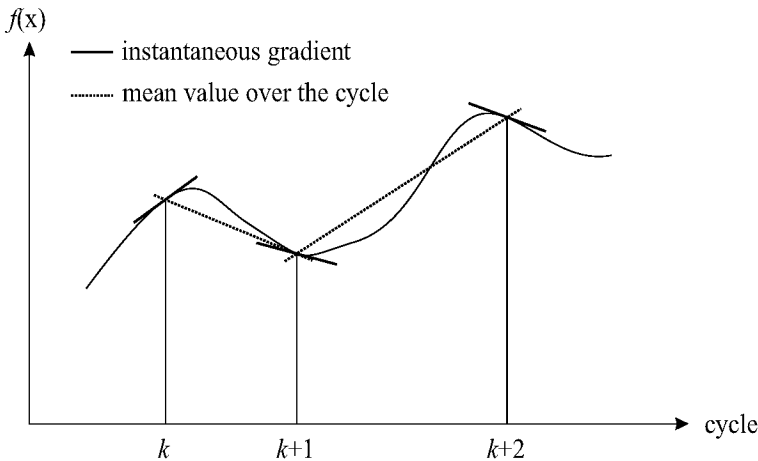


Figure 5.13: Linearization strategy: slope approximation.

5. Identification of the Wall Wetting Parameters

The Kalman filter algorithm consists essentially of two steps [22]:

- extrapolation of the state variables
- state-update

In the extrapolation step, the state variables \hat{x}_k are directly propagated by integrating the nonlinear differential equation at each sampling interval T_s , e.g., by using Euler integration:

$$\bar{x}_k = \hat{x}_{k-1} + T_s f(\hat{x}_{k-1}, u_k). \quad (5.11)$$

The covariance matrix $\bar{\Sigma}_k$, which represents the errors in the state variables estimates before the state-update is approximated by:

$$\bar{\Sigma}_k = \Phi_k \hat{\Sigma}_{k-1} \Phi_k^T + Q_k. \quad (5.12)$$

Note that the discrete process-noise matrix Q_k can be calculated from the continuous process-noise matrix Q [65]:

$$Q_k = \int_0^{T_s} \Phi(\tau) Q \Phi^T(\tau) d\tau. \quad (5.13)$$

In the state-update step, the Kalman gain K_k is calculated from the Riccati equation:

$$K_k = \bar{\Sigma}_k H_k^T [R_k + H_k \bar{\Sigma}_k H_k^T]^{-1}. \quad (5.14)$$

The state variables are updated on the basis of this gain and on the measurement error:

$$\hat{x}_k = \bar{x}_k + K_k [y_{mk} - g(\bar{x}_k, u_k)]. \quad (5.15)$$

The covariance matrix $\hat{\Sigma}_k$, which represents the errors after the state-update is calculated with the Kalman gain:

$$\hat{\Sigma}_k = [I - K_k H_k] \bar{\Sigma}_k. \quad (5.16)$$

The algorithm needs the starting values for the state variables and the covariance matrix to be set up. Therefore, at the time step $k = 0$:

$$\begin{aligned}\hat{x}_0 &= x_0 \\ \hat{\Sigma}_0 &= \Sigma_0.\end{aligned}\tag{5.17}$$

The choice of Σ_0 tells about the confidence that we have on the starting values of the parameters and affects how quickly the state estimation converges to the actual values. A large value of Σ_0 means a large uncertainty in the estimation and will cause the filter to corrects the state variables more rapidly. Eventually, a too large value can cause convergence problems. Another possibility to tell the filter about the confidence on the model is to tune the process noise ($\phi_{1,2,\dots,n}$) or the measurement noise autocovariances ($r_{1,2,\dots,p}$).

Parameters as “Fictitious” State Variables

The idea is to express the parameter to be estimated (x_P) as a “fictitious” state-variable and to write a differential equation for its propagation [65]. Because the parameter is assumed to be constant, the model is given by:

$$\dot{x}_P = v_P,\tag{5.18}$$

where v_P is the process noise of the parameter. Considering a simple example:

$$\begin{aligned}\dot{x}_1 &= -a \cdot x_1 + u \\ \dot{x}_2 &= x_1.\end{aligned}\tag{5.19}$$

5. Identification of the Wall Wetting Parameters

If the parameter a has to be estimated, the system has to be expanded as follows:

$$\begin{aligned}\dot{x}_1 &= -x_3 \cdot x_1 + u + v_1 \\ \dot{x}_2 &= x_1 + v_2 \\ \dot{x}_3 &= v_3,\end{aligned}\tag{5.20}$$

where $x_3 = a$, and v_1, v_2, v_3 are the process-noises. From the previous linear system, a nonlinear system is derived. The extended version of the filter can thus be used as observer.

5.3.2. Extended Kalman Filter Applied to the Wall Film and the Exhaust

The wall wetting system can be mainly described with one state variable, i.e., the wall wetting mass m_{WF} .

This value cannot be measured directly, but only estimated from the behavior of the A/F ratio in the exhaust gases. In order to be able to compare the output of the model with the measured signal, two more discrete state variables are necessary: the mass of air and the mass of fuel that are burned in the cylinder (m_{Acyl} , m_{Fcyl}). These state variables describe the exhaust gas dynamics model as developed in Chapter 3.

Usually, the extrapolation of the state variables and the state-update occur one after the other at every sampling time. In the fuel path dynamics however, the state-update is performed only at the end of each combustion cycle, i.e., when a new outcome of the combustion is available in the exhaust, and thus measurable. The sample time of the state-update depends therefore on the engine speed (cycle time, Figure 5.14), while the extrapolation of the state variables occur at a faster rate (5 ms).

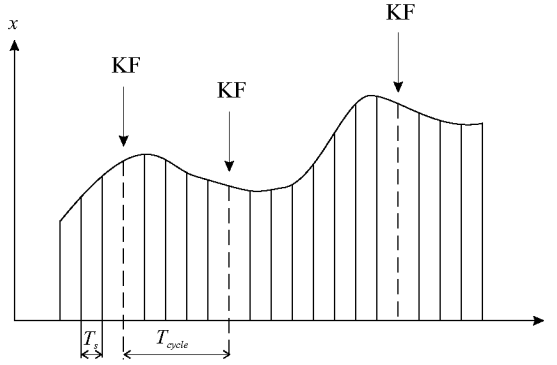


Figure 5.14: Timing of the extended Kalman filter, state propagation every T_s (KF=states-update).

Simplified Model

The Kalman filter technique is applied to the model presented in Chapter 4. To reduce the complexity of the calculations, it is advisable to simplify the model. As remarked in Equation 4.61, the thickness of the film is very small compared to the diameter of the valve. Additionally, the density of the fuel gas is much smaller than of the liquid. Therefore the surface, the volume, and the density can be approximated as:

$$\begin{aligned}
 A_{WF} &\approx \pi \cdot h_{WF} \cdot d_{in} \\
 V_{WF} &\approx \pi \cdot h_{WF} \cdot d_{in} \cdot \delta_{WF} \\
 \rho_{Fvs} &\approx \rho_{Fl}/2.
 \end{aligned} \tag{5.21}$$

5. Identification of the Wall Wetting Parameters

These approximations lead to following equations:

$$\begin{aligned}\frac{dm_{WF}}{dt} &= \dot{m}_{WF_{in}} - \frac{1}{2} \cdot \frac{D_{AB}Sh_F \ln(1+B)}{d_{in} \cdot \delta_{WF}} \cdot m_{WF} \\ \dot{m}_{EVF} &= \frac{1}{2} \cdot \frac{D_{AB}Sh_F \ln(1+B)}{d_{in} \cdot \delta_{WF}} \cdot m_{WF}.\end{aligned}\quad (5.22)$$

This model as well as the complete model are tested with the Kalman filter.

Choice of the State Variables

The wall wetting system can be described with various state variables. This is due to the relationships between different variables, such as the wall film mass m_{WF} and the wall film height h_{WF} . This relationship is present because of the geometric assumption which was made for the wall film geometry; with any other geometric assumption, other variables will be connected to the wall film mass. The state-space representation of the original system with the “fictitious” state variable is expressed in Equation 5.23:

$$\begin{aligned}\frac{dm_{WF}}{dt} &= \dot{m}_{WF_{in}} - \gamma \cdot m_{WF} + v_m \\ \frac{d\delta_{WF}}{dt} &= v_p \\ \dot{m}_{EVF} &= \gamma \cdot m_{WF} + r_m \\ \gamma &= \frac{D_{AB} \cdot Sh_F \cdot \ln(1+B)}{2 \cdot d_{in} \cdot \delta_{WF}}.\end{aligned}\quad (5.23)$$

The same equations expressed with the height h_{WF} instead of the film mass is:

$$\begin{aligned}
 \frac{dh_{WF}}{dt} &= -\frac{\alpha}{\beta} \cdot h_{WF} + \frac{1}{\beta} \cdot \dot{m}_{WF_{in}} + v_m \\
 \frac{d\delta_{WF}}{dt} &= v_p \\
 \dot{m}_{EVF} &= \alpha \cdot h_{WF} + r_m \\
 \alpha &= \pi \cdot \rho_{Fvs} \cdot D_{AB} \cdot Sh_F \cdot \ln(1 + B) \\
 \beta &= \pi \cdot \rho_{Fl} \cdot d_{in} \cdot \delta_{WF}.
 \end{aligned} \tag{5.24}$$

Both representations have two state variables (one real and one “fictitious”) and the same output. The main difference between these representation lies in the fact that the influence of the parameter δ_{WF} is remarkable both in the state variable and in the output equation (γ of Equation 5.23), or is remarkable only in the state equation (β of Equation 5.24). This influences the behavior and the performance of the Kalman filter, in particular because of the required condition of observability of the system.

Observability Issues

The main condition for the proper application of the Kalman filter is the complete observability of the system [11, pp. 260–264], [36, pp. 182–185]. One method to check the observability of the system is given by the properties of the linear system [22], namely the observability matrix Λ_n must have full rank ($A \in \mathbb{R}^{n \times n}$).

$$\Lambda_n = \begin{bmatrix} C \\ CA \\ CA^2 \\ \dots \\ CA^{n-1} \end{bmatrix} \tag{5.25}$$

5. Identification of the Wall Wetting Parameters

If we assume that we can measure the evaporating fuel flow \dot{m}_{EVF} for the state-space representation of Equation 5.23 we have:

$$A = \begin{bmatrix} -\gamma & \gamma \frac{m_{WF}}{\delta_{WF}} \\ 0 & 0 \end{bmatrix}. \quad (5.26)$$

And for the output matrix C :

$$C = \begin{bmatrix} \gamma & -\gamma \frac{m_{WF}}{\delta_{WF}} \end{bmatrix}, \quad (5.27)$$

and therefore:

$$\Lambda_2 = \begin{bmatrix} \gamma & -\gamma \frac{m_{WF}}{\delta_{WF}} \\ -\gamma^2 & \gamma^2 \frac{m_{WF}}{\delta_{WF}} \end{bmatrix}. \quad (5.28)$$

The matrix Λ_2 has rank 1, therefore complete observability is never granted. This state-space representation is not feasible to be observed. This fact can be physically explained by considering the connection between the wall wetting fuel mass and the geometry of Figure 4.14. In fact, the wall wetting fuel mass m_{WF} is calculated with both the height and the thickness (h_{WF} , δ_{WF}), however the mapping is not unique, because two or more different pairs can be mapped to the same wall wetting fuel mass (Figure 5.15).

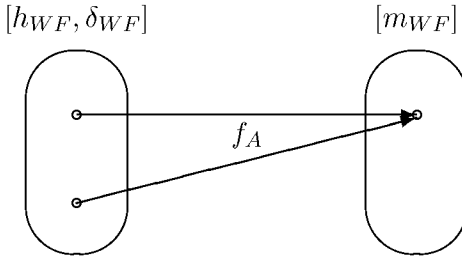


Figure 5.15: Mapping of pair $[h_{WF}, \delta_{WF}]$ to $[m_{WF}]$.

5.3. On-Line Optimization

To guarantee observability, both values have to be expressed as in Equation 5.24. For that state-space representation we have:

$$A = \begin{bmatrix} -\frac{\alpha}{\beta} & f(\alpha, \delta_{WF}, \dot{m}_{WFIn}) \\ 0 & 0 \end{bmatrix}, \quad (5.29)$$

where $f(\alpha, \delta_{WF}, \dot{m}_{WFIn})$ is defined as:

$$f(\dots) = \frac{1}{\delta_{WF}} \left(\frac{\alpha}{\beta} \cdot h_{WF} - \frac{\dot{m}_{WFIn}}{\beta} \right), \quad (5.30)$$

and for the output matrix C :

$$C = [\alpha \quad 0]. \quad (5.31)$$

The observability matrix for Equation 5.24 is defined as follows:

$$\Lambda_2 = \begin{bmatrix} \alpha & 0 \\ -\frac{\alpha^2}{\beta} & \alpha \cdot f(\alpha, \delta_{WF}, \dot{m}_{WFIn}) \end{bmatrix}. \quad (5.32)$$

In this case, the observability is always granted, because the matrix Λ_2 has always full rank as long as $\alpha \neq 0$. The state-space representation of Equation 5.23 cannot be used here and will be abandoned.

Implemented System

The Kalman filter is designed to be applied to discrete systems. Therefore, the system is sampled and integrated at every sample time T_s with the Euler integration algorithm:

$$\bar{x}_k = \hat{x}_{k-1} + T_s \cdot f(\hat{x}_{k-1}, u_k, t_k), \quad (5.33)$$

5. Identification of the Wall Wetting Parameters

where f is:

$$f = -\frac{\alpha}{\beta} \cdot h_{WF} + \frac{1}{\beta} \cdot \dot{m}_{WFin}. \quad (5.34)$$

In a first academic approach (Section 5.3.3), the value of the evaporative mass flow \dot{m}_{EVF} is assumed to be measured.

$$\dot{m}_{EVF} = \alpha \cdot h_{WF}. \quad (5.35)$$

5.3.3. First Step

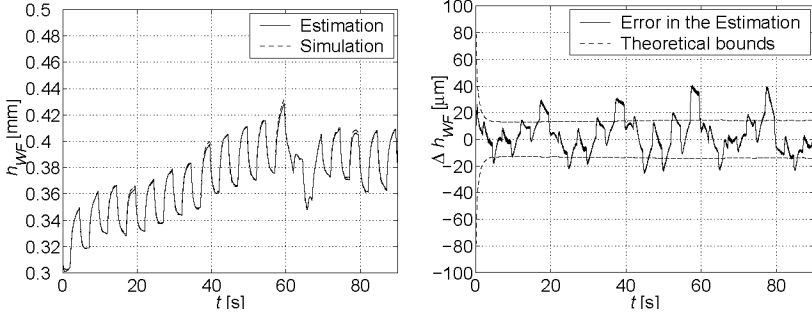
The first step of the Kalman filter design assumes that the signal used to update the state variables is the wall wetting evaporative mass flow \dot{m}_{EVF} , which is actually not measurable. This step was performed in order to check the performance of the various choices for the state-variables of the filter. Moreover, the matching between the estimated states with their simulations was tested.

Both the complex and the simplified model were tested. To quantify the EKF performance, the estimated state variables were initialized with some percentage of error with respect to those of the model. The tuning parameter of the EKF, the autocovariances of the process noise $\phi_{1,2}$ and the covariance of the measurement noise r_k (see Equation 5.5), were tuned to optimize the performance.

Results with the Complex Model

The lines in the following plots, indicated as theoretical ranges, are the square roots of the respective covariance matrix diagonal elements. If they converge to zero and they enclose the error in the estimate of states, it means that the EKF is performing an unbiased estimate.

5.3. On-Line Optimization



(a) Estimated height of the wall film

(b) Error in the estimation

Figure 5.16: Complex model, 10% initial bias in the state variables.

As depicted in Figure 5.16b, the estimation of the height is a success in a very small amount of time. The same cannot be said by the estimation of the thickness δ_{WF} (Figure 5.17b) where the convergence is very slow, and a bias is obtained.

5. Identification of the Wall Wetting Parameters

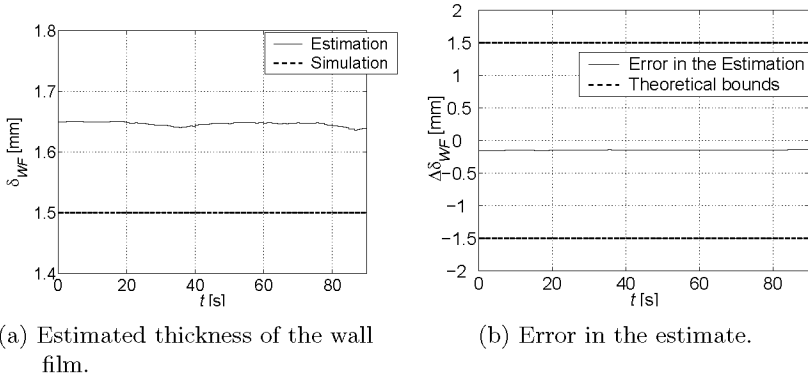
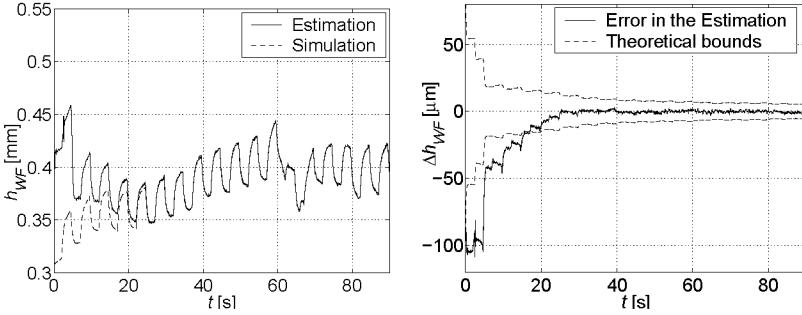


Figure 5.17: Complex model, 10% initial bias in the state variables.

In order to avoid this problem, another set of state variables was chosen, namely the height of the film h_{WF} and the internal diameter of the fuel coat d_{WF} .

5.3. On-Line Optimization



(a) Estimated height of the wall film.

(b) Error in the estimate.

Figure 5.18: Complex model, 30% initial bias in the state variables.

Taking the internal diameter d_{WF} instead of δ_{WF} as parameter turned out to be very helpful, since a good convergence of both h_{WF} and d_{WF} is achieved. With an initialization error of 30%, after about 20 s the estimated variables perfectly match the simulated reference values.

5. Identification of the Wall Wetting Parameters

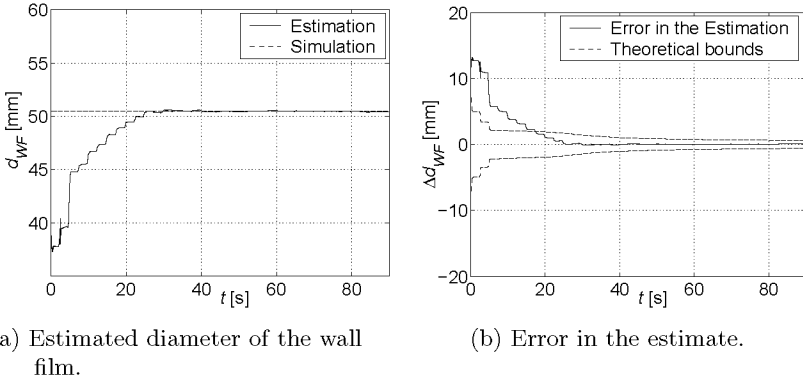
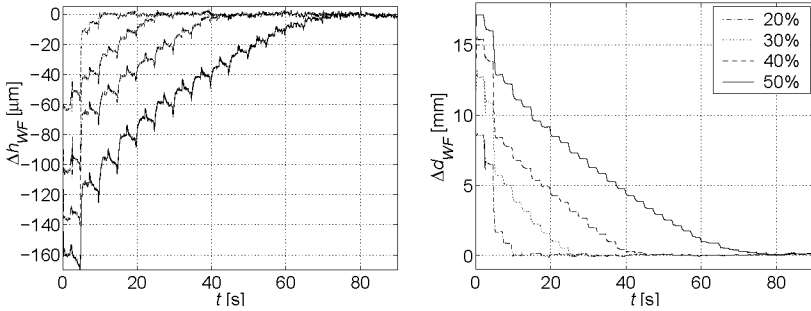


Figure 5.19: Complex model, 30% initial bias in the state variables.

The first consequence of this investigation is that the choice of the state variables for the complete model are definitively the height of the film h_{WF} and the internal diameter d_{WF} .

To demonstrate the actual performance of the filter, the convergence of the state variables with different initial bias was tested on the same simulation results (Figure 5.20).

5.3. On-Line Optimization



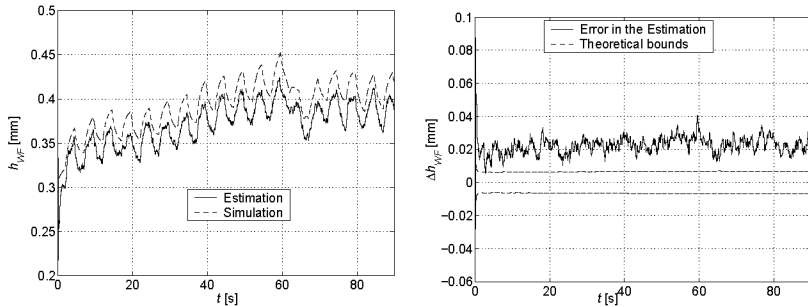
(a) Error in the estimate of the height. (b) Error in the estimate of the diameter.

Figure 5.20: Complex model, different initial biases in the state variables.

Results with the Simplified Model

The results depicted in Figures 5.21-5.22 concern the simplified model as expressed in Equation 5.22.

5. Identification of the Wall Wetting Parameters



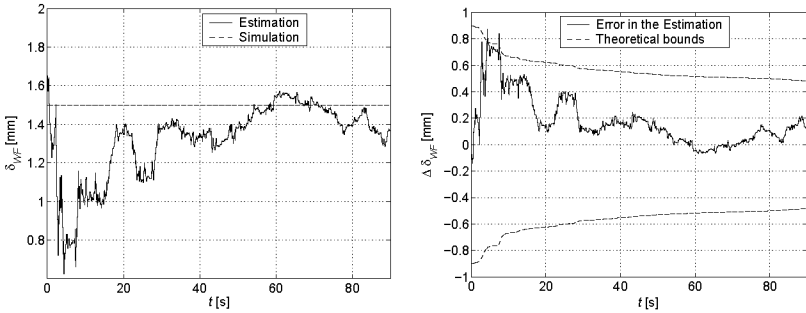
(a) Estimated height of the wall film. (b) Error in the estimate of the height.

Figure 5.21: Simplified model, 30% initial bias in the state variables.

Figures 5.21-5.22 show that the parameters tend to a value that is not the exact value of the complex model to which they are compared. Rather, a small bias is present.

Anyway, the estimation of the fuel mass in the cylinder is almost perfect (Figure 5.23).

5.3. On-Line Optimization



(a) Estimated thickness of the wall film. (b) Error in the estimate of the thickness.

Figure 5.22: Simplified model, 30% initial bias in the state variables.

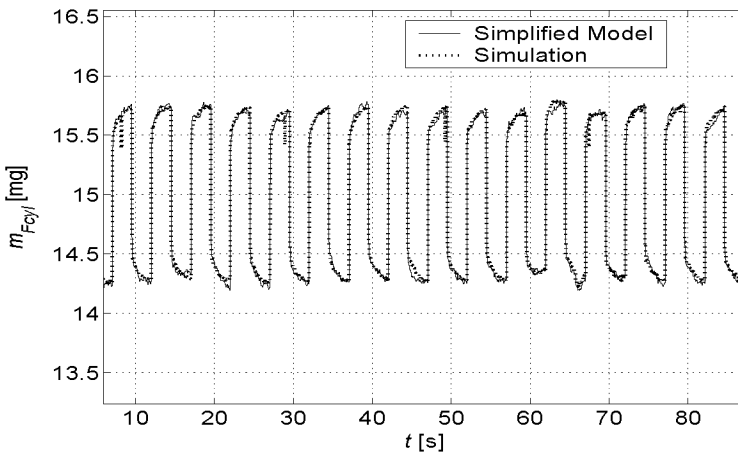


Figure 5.23: Simplified model vs. simulation, fuel in the cylinder.

5. Identification of the Wall Wetting Parameters

5.3.4. Second Step

Provided that the Kalman filter performs satisfactorily, the additional state variables of the exhaust gas dynamics are implemented. The result is a fourth-order system with following state variables:

$$x_{KF} = \begin{bmatrix} h_{WF} \\ d_{WF} \\ m_{Fcyl} \\ m_{Acyl} \end{bmatrix}. \quad (5.36)$$

In the simplified model, the state variable d_{WF} is replaced by the thickness δ_{WF} .

The measurement used by the Kalman filter for the correction of the states is the value of the A/F ratio in the exhaust (λ). However, the measurement of the A/F ratio is not enough to observe the system completely, for the same reason expressed in the example of Figure 5.15. In order to obtain observability, the system needs another measurement, namely the air mass exiting the cylinder. So, the measurements for the Kalman filter are:

$$y_{meas} = \begin{bmatrix} \lambda \\ m_{Aexh} \end{bmatrix}, \quad (5.37)$$

where m_{Aexh} is calculated with the intake manifold and the exhaust gas dynamics. Obviously, the assumption that the air mass is estimated correctly is of a bigger importance here. It is possible though, that a slight error in the estimation of the air can be compensated by the filter, for example by adjusting the evaporation from the film.

Merging Discrete and Continuous State Variables

The connection between the wall wetting and the exhaust gas dynamics is given by the evaporated fuel masses m_{EVF} and m_{EVD} . While the wall wetting evaporation is a continuous phenomenon, the exhaust gas dynamics is a discrete system. To calculate the fuel mass in the cylinder the mass evaporation rate \dot{m}_{EVF} is integrated over the cycle T_{cycle} . This way, the informations about the behavior of \dot{m}_{EVF} during the cycle is lost.

To compensate for this loss, for the calculation of the state matrices a mean value over the cycle of the continuous state variables is chosen, as for example h_{WF} . Its value could differ from the current h_{WF} . In other words the EKF have to correct on the basis of mean value informations.

The approximation for m_{EVF} used for the linearization of the system is made assuming that the evaporation rate has small, constant changes during the cycle:

$$m_{EVF} \approx T_{cycle} \cdot \dot{m}_{EVFlin} = C_p \cdot \frac{120}{n} \cdot \alpha \cdot h_{WF}(k), \quad (5.38)$$

where C_p is calculated with the nonlinear integrated m_{EVF} at the end of the cycle, namely when the state-update is performed (Figure 5.24). The results with the complete model are depicted in the Figures 5.25–5.28.

5. Identification of the Wall Wetting Parameters

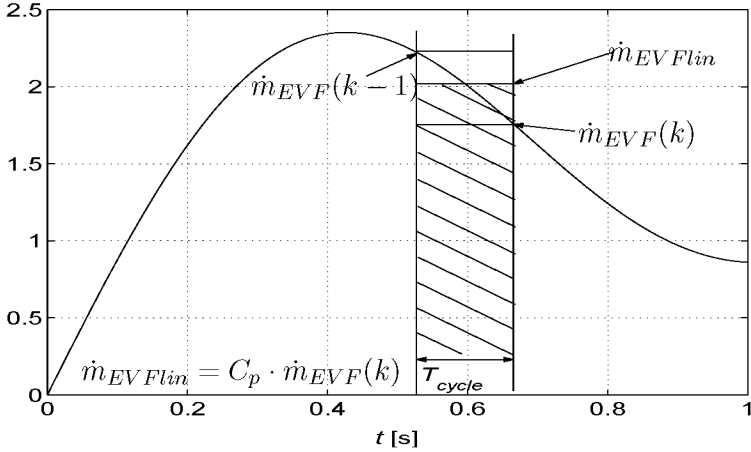
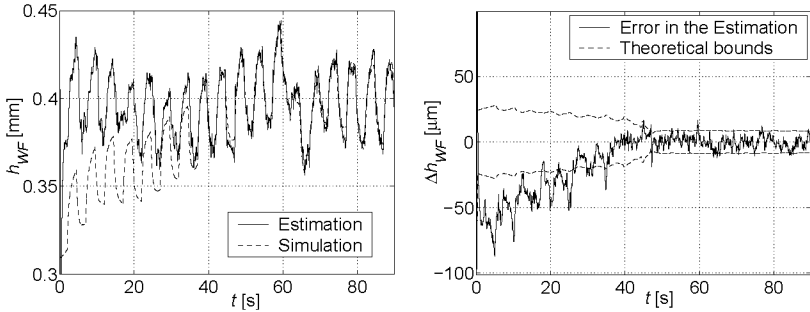


Figure 5.24: Linearization strategy for $\dot{m}_{EV F}$.



(a) Estimated height of the wall film. (b) Error in the estimate of the height.

Figure 5.25: Simulation results with the complete model, 30% initial bias in the state variables.

5.3. On-Line Optimization

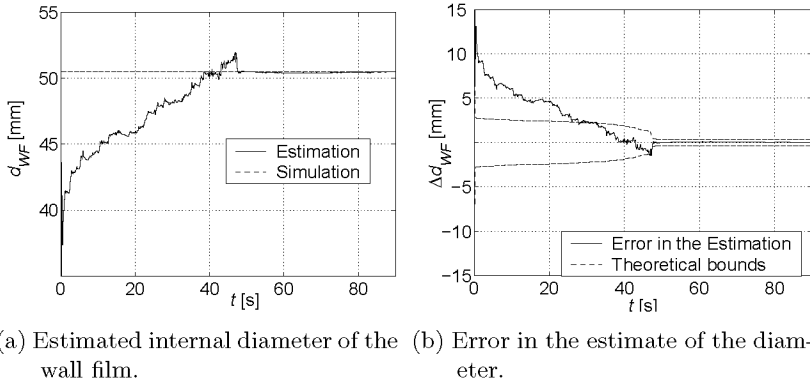


Figure 5.26: Simulation results with the complete model, 30% initial bias in the state variables.

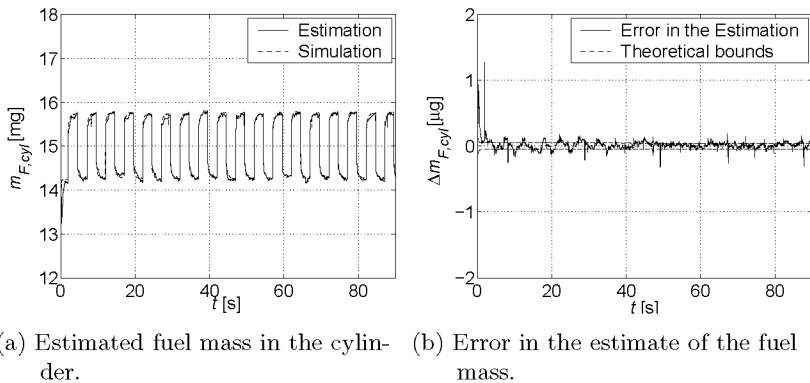


Figure 5.27: Simulation results with the complete model, 30% initial bias in the state variables.

5. Identification of the Wall Wetting Parameters

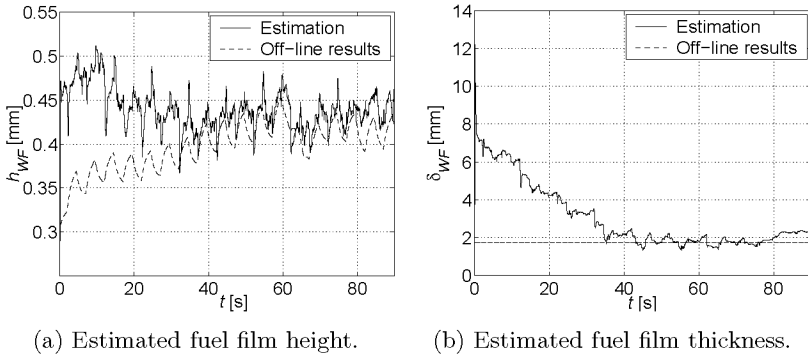


Figure 5.28: Test bench results with the complete model, compared with off-line results (dashed thin line).

The Kalman filter provides good results with the complete model as well. Figure 5.28 show the results obtained with data from the test bench. In order to evaluate the performance, the results are compared with the model parameterized off-line on the basis of the test bench operating conditions.

5.4. Discussion

The WW-model was developed to be as simple as possible and to have the best performance. This trade-off reduced the complexity of the model in a relevant way. In particular with the droplet model, the real complexity of a nonlinear, 3-D model was reduced significantly without losing too much on performance and extrapolation capability. This was demonstrated with the aid of different kind of experiments, which were performed on the test bench.

The connection between droplet model and wall film model provided excellent results, and its simplicity is proven by the equations implemented in the Kalman filter. The number of the parameters to be measured on the test bench was decreased in comparison with the simplest structure of Aquino, although the reduction to one single parameter was not possible.

The choice of the state variables of the Kalman filter was investigated focusing on the observability of the system and on the performance of the estimation. Actually, the Kalman filter has proved to be able to cope with small errors, and yield the internal state variables of the system in real time with a certain accuracy. The negative aspect of the Kalman filter is the need of a persistent excitation of the system in order to work properly. Moreover, in some cases the convergence of the algorithm was slow and difficult.

This chapter concludes the modeling of the fuel path and opens the chapter of the compensation, where different strategies to cope with the discussed dynamics are presented and tested.

5. *Identification of the Wall Wetting Parameters*

6. Wall Wetting Compensator

6.1. Introduction

After having introduced the model of the fuel path and having identified its relevant parameters, schemes for the compensation of the effects of the wall wetting dynamics are developed. This chapter presents two different approaches:

In the first approach, the knowledge acquired with the model is used in combination with the well-known compensator structure introduced by Aquino [4]. The WW-model is used to calculate the value of the parameters to make the compensator operate as an LPV system as described in [35] and in [43], while the Kalman filter, or any other identification algorithm, can be used to estimate the parameters of the WW-model (see Figure 6.1).

In the second approach, the knowledge of the state variables of the wall wetting and of the cylinder is used to calculate the future injection time on the basis of the current operating conditions (see Figure 6.2 and [47]).

The results of these approaches are presented in Section 6.5.

6. Wall Wetting Compensator

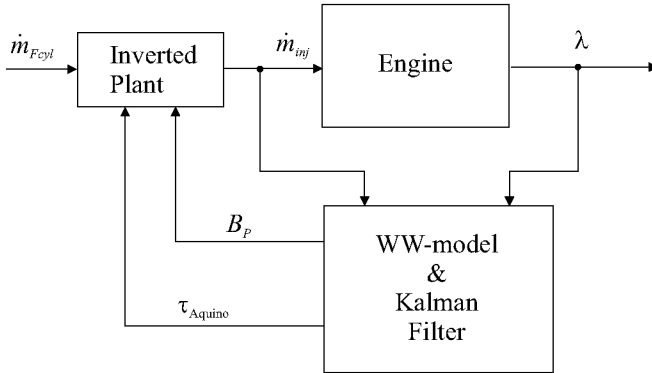


Figure 6.1: Compensator setup based on inverted LPV dynamics.

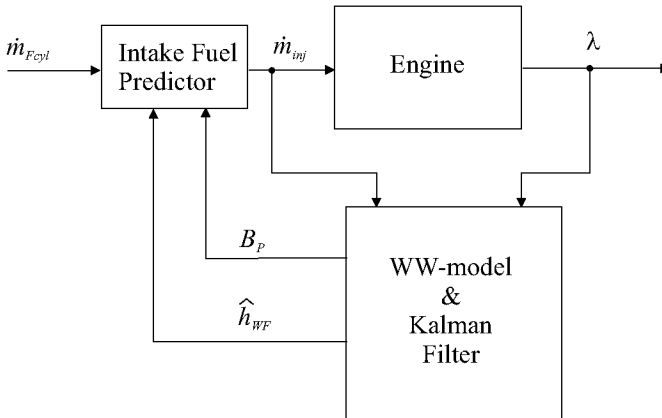


Figure 6.2: Compensator setup based on estimated state variables.

6.2. Compensation of the Timing Error

In port fuel injected engines, the injection of the fuel occurs before the intake valves open. This means that the actual air mass flow in the cylinder is measured after the injection and the quantity of fuel to be injected is based on a pre-estimate of the quantity of air. This time difference is described as timing error [64].

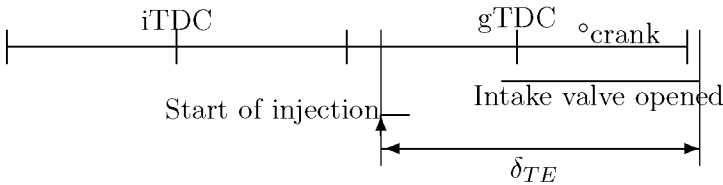


Figure 6.3: Minimal timing error δ_{TE} .

In a standard engine management system, the injection control is based on the measured air mass flow of the previous cylinder. In the management system used on the test bench, the air is calculated every millisecond and the injection control is based on the last possible estimate. In any case, the least possible timing error is depicted in Figure 6.3.

To compensate this error, the systems with electric-driven throttle can be very useful. Actually, by delaying the actuator signal to the throttle and using the model to predict the air mass flow in the cylinder, the timing error can be compensated (Figure 6.4).

6. Wall Wetting Compensator

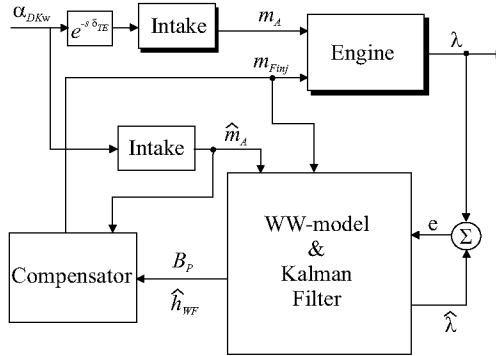


Figure 6.4: Compensation of the timing error (shaded blocks represent the real world).

The timing error compensation can be useful for the wall wetting compensation too. The estimation of the air mass flow in advance gives the opportunity to the WW-model to calculate the quantity of evaporated fuel and therefore calculate the correct wall wetting compensation.

6.3. LPV Structure of Aquino

The transfer function of the wall wetting system can be built on the basis of the nonlinear wall wetting model:

$$\begin{aligned}\frac{dh_{WF}}{dt} &= -\frac{\alpha}{\beta} \cdot h_{WF} + \frac{1}{\beta} \cdot \dot{m}_{WF\text{in}} \\ \dot{m}_{F\text{cyl}} &= \alpha \cdot h_{WF} + \dot{m}_{EVD},\end{aligned}\quad (6.1)$$

where α and β are:

$$\begin{aligned}\alpha &= \pi \cdot \rho_{Fvs} \cdot D_{AB} \cdot Sh_F \cdot \ln(1 + B) \\ \beta &= \pi \cdot \rho_{Fl} \cdot d_{in} \cdot \delta_{WF}.\end{aligned}\quad (6.2)$$

The relationship between the values $\dot{m}_{WF\text{in}}$ and \dot{m}_{EVD} with the injected fuel mass $\dot{m}_{F\text{inj}}$ is given by:

$$\begin{aligned}\dot{m}_{WF\text{in}} &= B_P \cdot \dot{m}_{F\text{inj}} \\ \dot{m}_{EVD} &= (1 - B_P) \cdot \dot{m}_{F\text{inj}},\end{aligned}\quad (6.3)$$

where the parameter $B_P = f(T_D, p_I, n, \tau_{DA})$ is given by the following expression:

$$B_P = 1 - \frac{1}{\dot{m}_{F\text{inj}}} \int_0^{t_{max}} \dot{m}_{EVD} \cdot dt, \quad (6.4)$$

which is a direct output of the droplet model (see Equation 4.27). The transfer function of the wall wetting is then:

$$G(s) = \frac{(1 - B_P)s + \frac{\alpha}{\beta}}{s + \frac{\alpha}{\beta}}. \quad (6.5)$$

Due to the fact that the A/F ratio in the cylinder changes once per engine cycle, the wall wetting compensator is usually programmed

6. Wall Wetting Compensator

in its digital form. The discrete transfer function of the plant is given by:

$$G(z) = \frac{m_{F_{cyl}}}{m_{F_{inj}}} = \frac{(1 - B_P)z + (B_P - A_P)}{z - A_P}, \quad (6.6)$$

where the parameter A_P is connected to the continuous model as follows [22]:

$$A_P = e^{-\frac{\alpha}{\beta} T_s}, \quad (6.7)$$

where T_s is the cycle time¹. The value of A_P can eventually be expressed as in Equation 4.67.

The parameter B_P is the same as for the continuous model, because the evaporation of the droplet happens only once per cycle and its value does not change until the following cycle. Concerning the calculation of B_P , the assumption of a constant τ_{DA} for a given engine, which was verified in Chapter 5, reduces the model to a 3D-characteristic diagram that can be calculated in advance. The inputs for this characteristic diagram are the droplet temperature T_D , the manifold pressure p_I , and the engine speed n . Two examples of B_P calculated with two different values of τ_{DA} are depicted in the Figures 6.5–6.6.

¹ $T_s = 120/n$ for a single cylinder

6.3. LPV Structure of Aquino

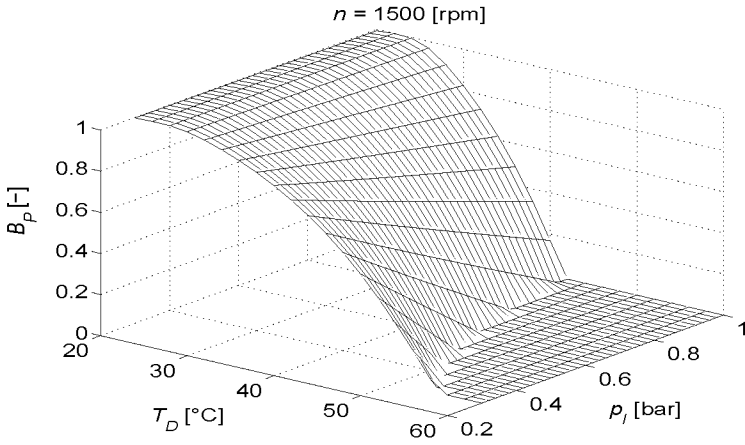


Figure 6.5: Aquino parameter B_P for $\tau_{DA}=3.45$ ms.

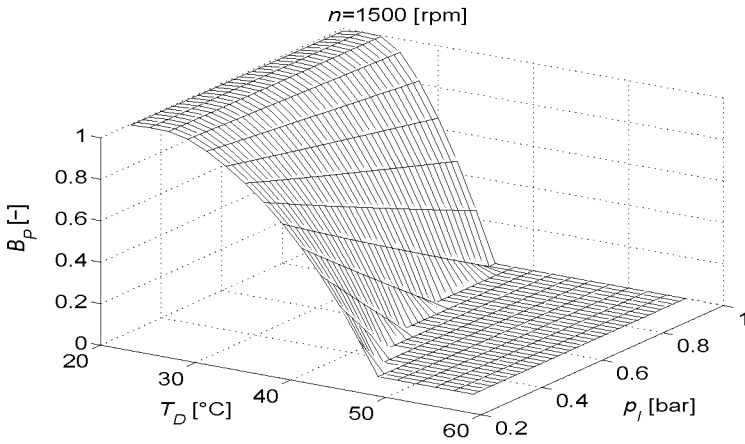


Figure 6.6: Aquino parameter B_P for $\tau_{DA}=7$ ms.

6. Wall Wetting Compensator

6.3.1. Design of the Compensator

The design of the compensator is described in Equation 6.8:

$$G_{comp}(s) = G_{WW}^{-1}(s) = \frac{s + \frac{\alpha}{\beta}}{(1 - B_P)s + \frac{\alpha}{\beta}}, \quad (6.8)$$

with the state space representation:

$$\begin{aligned} \frac{dh_{WF}}{dt} &= \frac{1}{1 - B_P} \left(-\frac{\alpha}{\beta} \cdot h_{WF} + B_P \cdot \dot{m}_{F_{cyl_w}} \right) \\ \dot{m}_{F_{inj}} &= \frac{1}{1 - B_P} (\dot{m}_{F_{cyl_w}} - \alpha \cdot h_{WF}), \end{aligned} \quad (6.9)$$

where $\dot{m}_{F_{cyl_w}}$ is the desired fuel mass flow into the cylinder. The discrete transfer function is given by:

$$G_{comp}(z) = G_{WW}^{-1}(z) = \frac{z - A_P}{(1 - B_P)z + (B_P - A_P)}. \quad (6.10)$$

The strategy is based on the inversion of the plant to eliminate all its effects. If the model is perfectly matched with the real system, this strategy is very effective. However, some small errors or disturbances can always be expected. Moreover, the Bode diagram of a usual compensator shows an amplification of the high frequencies which causes high frequency noise to be amplified (Figure 6.7a).

6.3. LPV Structure of Aquino

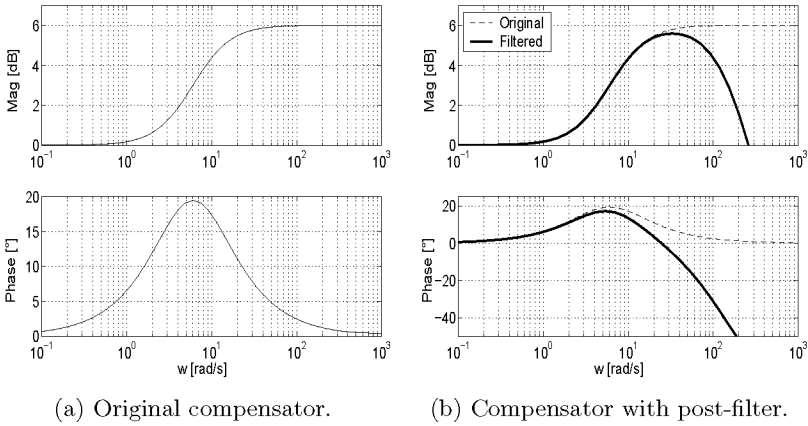


Figure 6.7: Example for the Bode diagram of the wall wetting compensator, normal and filtered.

In order to reduce the problem of the amplification at high frequencies, a possible solution is the application of a post-filter, parameterized to cut the frequencies higher than the bandwidth of the wall wetting dynamics (Figure 6.7b).

6.3.2. Stability of the Compensator

To check the stability of the compensator, the poles of its transfer function need to be investigated. The pole of the discrete transfer function must lie within the unit circle of the complex plane, i.e., when $|z_P| < 1$ is true:

$$|z_P| = \left| \frac{A_P - B_P}{1 - B_P} \right| < 1. \quad (6.11)$$

6. Wall Wetting Compensator

Therefore, the condition of stability is:

$$A_P > 2B_P - 1. \quad (6.12)$$

The region where this condition is satisfied is depicted in Figure 6.8. The main difference between the continuous and the discrete compensator is that the output of the discrete compensator can oscillate. The region of this under-damped condition is given in [43]:

$$A_P < B_P \cap A_P \leq 2B_P - 1. \quad (6.13)$$

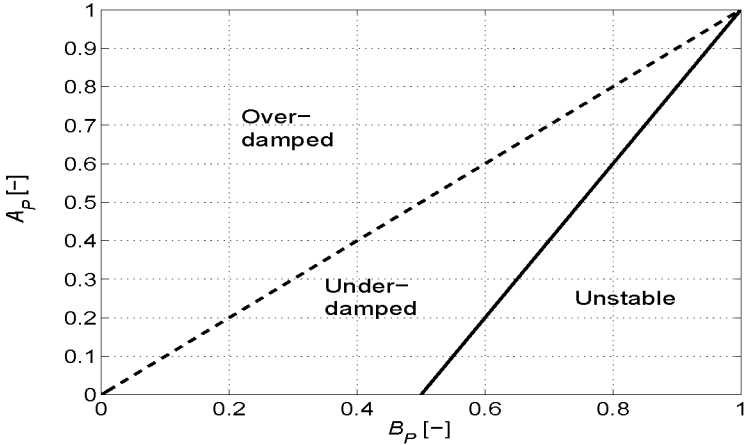


Figure 6.8: Stability region of the discrete compensator.

Note that a large impingement parameter B_P implies a danger of instability, depending on the value of the evaporation parameter A_P . In other words, the faster the film evaporation is ($A_P \rightarrow 0$) and/or the larger the impingement on the intake walls

is ($B_P \rightarrow 1$), the higher is the risk of instability. For a B_P smaller than 0.5 the transfer function of the compensator will always be stable.

The effect of a bigger value of τ_{DA} is interesting: As shown in Figure 6.6, the critical value for B_P is reached at higher temperatures. If we consider the fact that τ_{DA} increases for a decrease of the injection-timing advance¹, the conclusions are obviously that the compensator for an engine with injection into the opened intake valves cannot be unstable. If the compensator is not stable, another method has to be applied, as for example the one suggested in [47], the method described in the following section, or the method based on the Kalman estimate as described in Section 6.4.

Ensure a Good Stability

The main problem of a compensator is the danger of instability. As depicted in Figure 6.8 the region where the wall wetting compensator shows instability is quite small, however it cannot be a-priori excluded that a parameter set exists in this region. Anyway, if the compensator shows stability, it still does not mean that it is working well. The region where the output of the compensator has an oscillating behavior (under-damped) should be avoided too. In order to avoid an oscillating compensator, the approach described in [43] can be used.

The starting point is the value of the evaporation parameter A_P . A horizontal line is drawn as in Figure 6.9 up to the point where it crosses the limit between the over-damped and the under-damped zone. The value of B_P at this point is the maximum possible value

¹decreasing advance = injection starts later, towards opened intake valves

6. Wall Wetting Compensator

to ensure an good stability of the compensator. In other terms:

$$B_{Pmax} = A_P, \quad (6.14)$$

and for the compensator:

$$B_P \in [0, B_{Pmax}]. \quad (6.15)$$

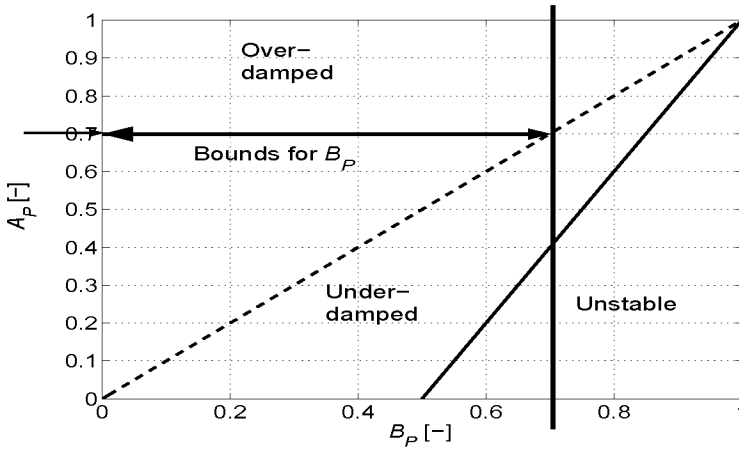


Figure 6.9: Setting bounds for the parameter B_P of the compensator.

The effect of this limit on the compensation can be observed in Figure 6.10, where a step response of a perfectly compensated wall wetting dynamics is compared with step responses of partly compensated dynamics. In particular, the limits for the actual B_P are set at $B_{Pmax} = 0.9 \cdot B_P$, $B_{Pmax} = 0.8 \cdot B_P$, and $B_{Pmax} = 0.7 \cdot B_P$.

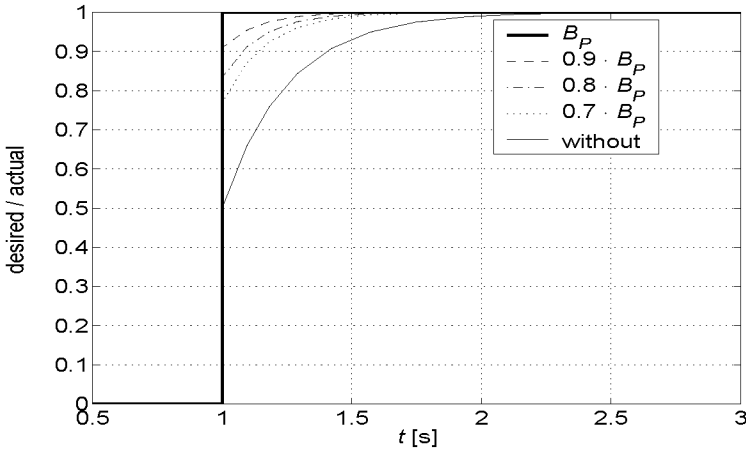


Figure 6.10: Effects of the bounds for the parameter B_P of the compensator on a step response.

The responses show that a limitation of 20% on the value of B_P yields an error in the compensation of about 16% compared to no compensation, while a limitation of 30% yields an error of about 24%. This procedure is obviously sub-optimal, however, in order to avoid oscillations and instability, this error can be afforded.

In addition to the problems caused by an oscillating output of the compensator, disturbances can cause the compensator to over-react. In order to avoid problems of a over-reacting compensator, a slight change in the structure of the compensator may be advisable [64]. The estimation of the fuel mass evaporating from the wall film can help to perform this change.

6.4. Compensator Based on the Estimated State Variables

A compensator based on the Kalman filter was documented in [47] and subsequently in [7]. The procedure is focused on the use of the knowledge of the state variables of the wall wetting to control the fuel flow in the cylinder. This way, the delay between the A/F ratio present in the cylinder and the measured A/F ratio, as discussed in Chapter 3 (Figure 3.4), can be eliminated.

Given a desired quantity of fuel in the cylinder, the quantity of fuel to be injected is given by:

$$\dot{m}_{Finj} = \frac{1}{1 - B_P} \left(-\underbrace{\alpha \cdot \hat{h}_{WF}}_{\hat{m}_{EVF}} + \dot{m}_{F_{cyl_w}} \right). \quad (6.16)$$

The state estimation algorithm provides the height of the film \hat{h}_{WF} , while the values of α and B_P are dependent on the boundary conditions (pressure, temperature, and engine speed). The resulting compensator is relatively simple. However, it relies strongly on the accuracy of the estimation of h_{WF} , and therefore its stability cannot be guaranteed easily. Moreover, due to its dependency on the output of the Kalman filter \hat{h}_{WF} , the compensator has the form of a feedback controller. Actually, the goal is to control the quantity of the fuel flow in the cylinder. One method to apply this control is called model matching.

The model matching method is based on shaping the transfer function of a given plant $G_P(s)$ by specific interventions on the input signal in order to match a desired behavior $G_M(s)$ ("reference model") [12]. The inversion of the plant is an extreme case of this method, where the desired behavior is $G_M(s) = 1$. The scheme of this procedure is depicted in Figure 6.11.

6.4. Compensator Based on the Estimated State Variables

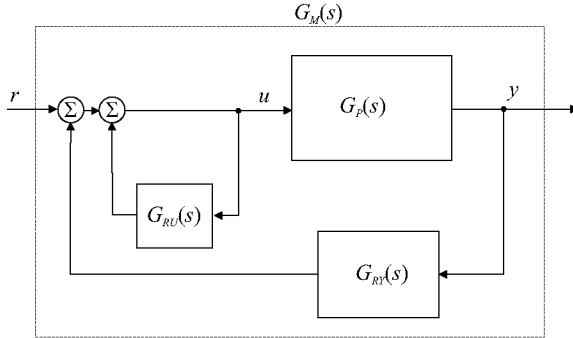


Figure 6.11: Signal flow diagram of the model-matching.

In this case the plant $G_P(s)$ includes the wall wetting dynamics, i.e., from the injection to the fuel mass flow into the cylinder. The meaning of the signals in Figure 6.11 is:

$r = \dot{m}_{F_{cyl_w}}$: desired fuel mass flow into the cylinder

$u = \dot{m}_{F_{inj}}$: fuel to be injected

$y = \hat{\dot{m}}_{F_{cyl}}$: estimated fuel mass flow into the cylinder

The transfer functions G_{RU} and G_{RY} are chosen so that the transfer function between r and y is reshaped. The choices for the wall wetting dynamics are the following transfer functions:

$$G_{RU}(s) = \frac{\gamma_1 \cdot s + \gamma_0}{(1 - B_M)s + \Omega_M} \quad (6.17)$$

$$G_{RY}(s) = \frac{\beta_0}{(1 - B_M)s + \Omega_M}, \quad (6.18)$$

where $\Omega_M = \alpha/\beta$ and B_M are the parameters of the wall wetting

6. Wall Wetting Compensator

reference model;

$$G_M(s) = \frac{(1 - B_M)s + \Omega_M}{s + \Omega_M}. \quad (6.19)$$

To obtain the desired behavior, the parameters γ_0 , γ_1 , and β_0 have to be chosen as follows:

$$\begin{aligned} \gamma_0 &= \Omega_M - \Omega_P \\ \gamma_1 &= B_P - B_M \\ \beta_0 &= -\gamma_0. \end{aligned} \quad (6.20)$$

Note that if a complete compensation is desired ($G_M(s) = 1$, $B_M = 0$), the transfer functions G_{RU} and G_{RY} have the form:

$$G_{RU}(s) = \frac{B_P s + \Omega_M - \Omega_P}{s + \Omega_M} \quad (6.21)$$

$$G_{RY}(s) = \frac{\Omega_P - \Omega_M}{s + \Omega_M}, \quad (6.22)$$

where Ω_M can be chosen almost freely. The wall film evaporation is faster by larger values of Ω_M . So the favorable choice of Ω_M is:

$$\Omega_M \gg 0. \quad (6.23)$$

If the estimation of \hat{m}_{EVF} is disturbed by noise, G_{RY} can filter it by choosing an appropriate value of Ω_M . The discrete equivalents of the model matching parameters are:

$$\begin{aligned} \gamma_0 &= (B_M - A_M) - (B_P - A_P) \\ \gamma_1 &= B_P - B_M \\ \beta_0 &= A_M - A_P, \end{aligned} \quad (6.24)$$

6.4. Compensator Based on the Estimated State Variables

and for $G_M(z) = 1$ the transfer functions are:

$$G_{RU}(z) = \frac{B_P z + (A_P - A_M - B_P)}{z - A_M} \quad (6.25)$$

$$G_{RY}(z) = \frac{A_M - A_P}{z - A_M}. \quad (6.26)$$

The favorable choice of A_M is, according to Equation 6.23 and Equation 6.7:

$$A_M \approx 0. \quad (6.27)$$

This method has the advantage that it can be used in case of a set of parameters which would generate an unstable compensator. However, it has several disadvantages. First of all, the compensator is based on the quality of the estimation of the state variables by the extended Kalman filter. Occurring problems in the convergence of the estimate, such as oscillations, bias, etc., make the compensator work with corrupted informations. This inconvenience can lead to an instability of the process.

6.5. Results with the Compensators

The goal of this section is to test both compensator strategies in order to choose the best to implement on the test bench. The tests are performed with constant air mass flow (fuel modulation) and with variable air mass flow (throttle tip-ins and tip-outs).

On the second part of the section, with experiments on the test bench, the capability of the compensator to cope with all operating conditions is tested at different engine temperatures by means of tip-in and tip-out experiments.

6.5.1. Experiments with Fuel Modulation

As in the task of the identification of the parameters, the first experiments are performed with constant air mass flow and fuel modulation. In this case, the task of the compensator is to ensure the exact amount of fuel in the cylinder as specified by the modulation signal (a square wave). The values for air mass flow, manifold pressure, temperatures, engine speed, etc., come directly from measurements on the test bench, so that all the disturbances are included. Figures 6.12 and 6.13 show some results of these experiments.

6.5. Results with the Compensators

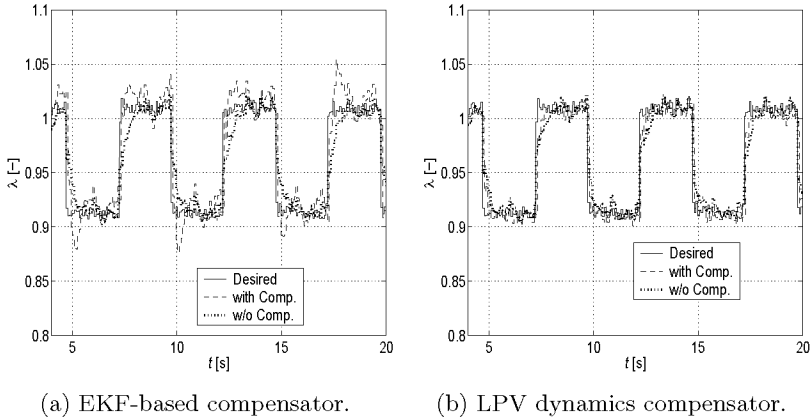


Figure 6.12: Results of the compensator with fuel injection modulation (1500 rpm).

The results with the LPV dynamics show a better performance, in particular during the steady-state phase. The compensator based on the EKF tends to overshoot. However, the EKF was started after approximately 2 seconds from the start of the measurement, so that it has still not reached its optimal estimation. Although the overshoots tend to be reduced with the time, they still appear (see Figure 6.13). The results are clearly sub-optimal.

6. Wall Wetting Compensator

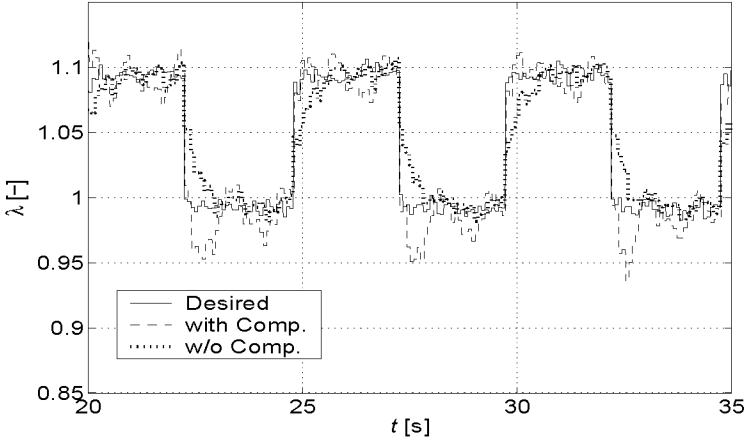


Figure 6.13: Results of the EKF-based compensator.

6.5.2. Experiments with Throttle Tip-In and Tip-Out

For a wall wetting compensator, the throttle tip-ins and tip-outs are the most difficult events to deal with. In this case, the goal of the compensator is almost same as by the previous experiment with the difference that the desired fuel mass in the cylinder is connected to the air mass by the stoichiometric condition, in other terms:

$$m_{F_{cyl_w}} [\text{g/cyl}] = \sigma_0 \cdot \frac{1}{\lambda_w} \cdot m_A [\text{g/cyl}], \quad (6.28)$$

where σ_0 is the stoichiometric coefficient and λ_w is the desired A/F ratio in the cylinder.

The most meaningful results of the compensator, are depicted in Figures 6.14–6.15. The behavior of the A/F ratio with the λ -

6.5. Results with the Compensators

controller without compensator is also shown (dotted line). The compensator with LPV dynamics works clearly better than the EKF-based compensator. The influence of the compensator can be observed in Figure 6.16.

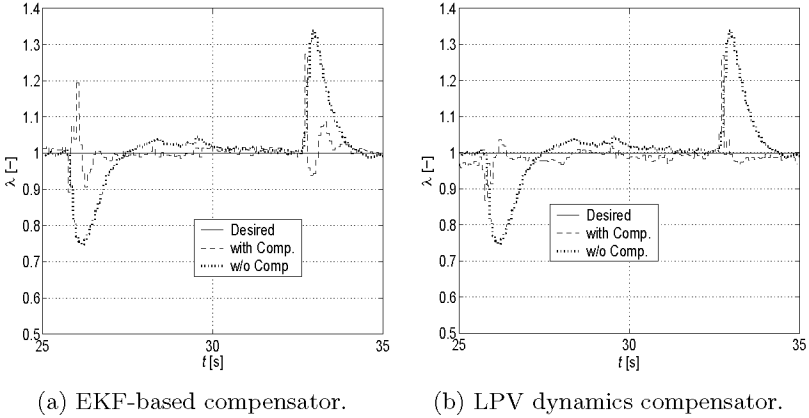
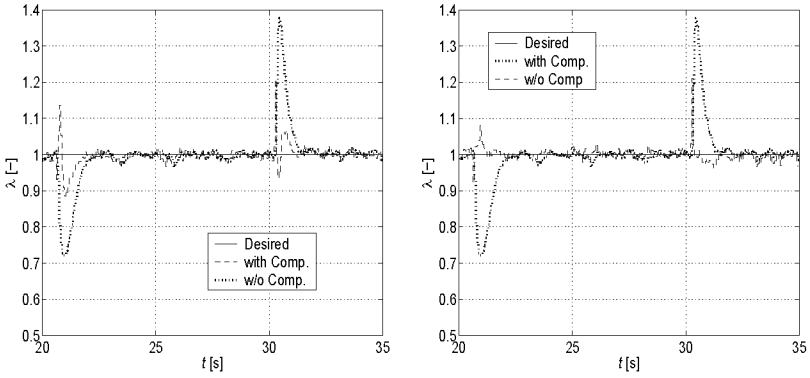


Figure 6.14: Results of the compensator (1500 rpm).

6. Wall Wetting Compensator



(a) EKF-based compensator.

(b) LPV dynamics compensator.

Figure 6.15: Results of the compensator (2000 rpm).

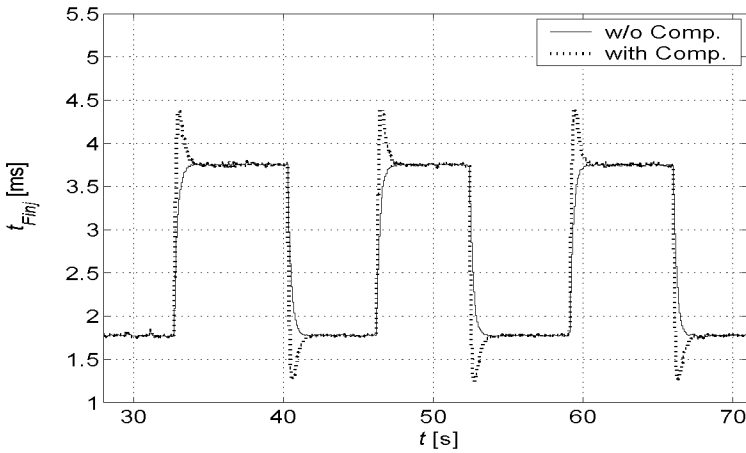


Figure 6.16: Influence of the compensator on the injection signal.

6.5.3. Experiments on the Test Bench

To observe and evaluate the work of the compensator, a simple experiment was measured. During tip-in/tip-out events, the compensator was switched off to show the resulting λ in the exhaust. The difference is evident (see Figure 6.17).

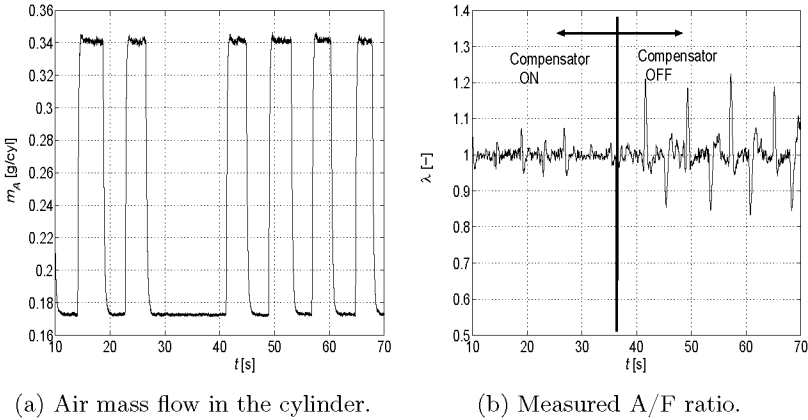


Figure 6.17: Results of the compensator (1500 rpm, switched on-off).

The left part of Figure 6.17b shows that not all the effects could be compensated. Some small peaks are still present. This is due to small errors in the modeling during transients, such as partial misfires (bad combustion), back-flows, etc. However, the main disturbances are compensated.

The same experiment can be performed with a colder engine. The temperature model yields the temperature of the wall film, and

6. Wall Wetting Compensator

the current wall wetting parameters are calculated accordingly (see Equation 6.2). The tuning parameters (τ_{DA} and δ_{WF}) are kept to their “warmed-up” value.

The results for 60°C and 40°C coolant temperature are depicted in Figure 6.18 and in Figure 6.19.

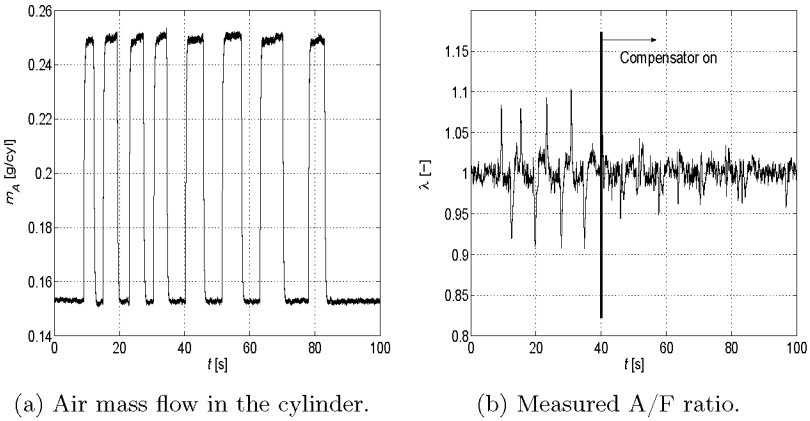


Figure 6.18: Results of the compensator at $T_{cool} = 60^\circ\text{C}$.

6.5. Results with the Compensators

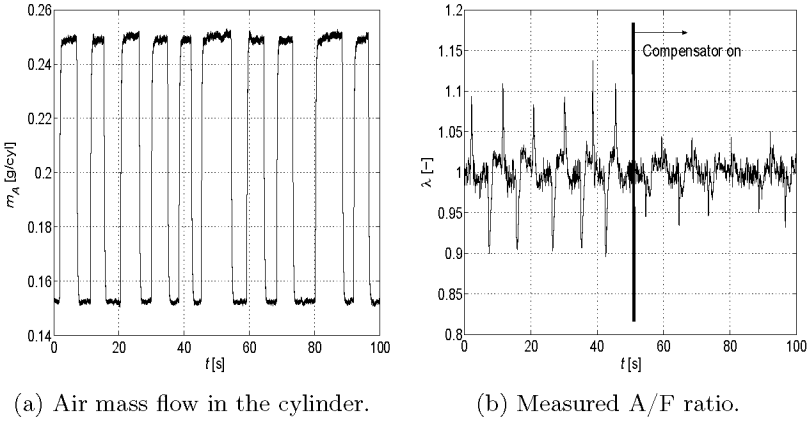


Figure 6.19: Results of the compensator at $T_{cool} = 40^\circ\text{C}$.

For the coldest temperature, the results are still good. With a small adaption of the thickness δ_{WF} the results are slightly better. However, the goal of this experiments was to show that the parameters, which are identified at normal engine conditions, in connection with the temperature model are able to cope with other operating temperatures, which occur, for example, during the engine warm-up phase.

6.6. Discussion

This chapter shows two possible ways to implement the model into the engine management system. Each one has its own advantages and disadvantages. The EKF-based compensator, for instance, has the advantage that it can adjust itself during the transients. This adaptivity can obviously result in a disadvantage if the Kalman filter provides an inexact estimation or its performance is bad, for example because of a bias in the state variables or an instability of the filter. Alas, this possibility cannot be avoided or excluded in advance. Under specific operating conditions, the Kalman filter showed a certain difficulty to reach a stable estimate.

The LPV dynamics compensator is simpler because it does not need an estimation of the internal state variables but only the parameters, which can be either estimated with the Kalman filter or any equivalent on-line identification algorithm, or they can be tuned on the basis of off-line experiments. In addition to these facts, the inverted LPV dynamics offers all the advantages that are applicable to all linear systems, as for example the possibility to check and ensure the stability directly from the parameters (see Equations 6.11 and 6.14). For these reasons, the LPV compensator resulted as the best choice.

The experiments performed on the test bench show that the temperature and pressure dependency of the wall film evaporation is correctly compensated by the algorithm of the WW-model. Actually, the experiments show that colder engine temperatures can be compensated even by maintaining the tuning parameter δ_{WF} to its warmed-up value.

7. Conclusions

The main requirements for this investigation are the reduction of the time to spend on the test bench for the calibration of the wall wetting compensator, and the extension of the compensator capabilities to the operating conditions which apply during the startup of the engine (cold engine and warm-up phase). Both goals have to be reached maintaining a simple structure in order to enable the integration of the result in a standard ECU.

For an engineer, the first task to perform in order to model a real system is to set the system boundaries, which are usually defined by the values that can be measured. A clean definition of these boundaries is a key point for an optimal identification of the parameters of the model. As pointed out during the whole work, the fuel path dynamics have a direct and inevitable relationship with the air filling dynamics. The consequence of this fact is that any modeling and/or compensation of the fuel path dynamics have to consider the behavior of the air mass flow. There are two possibilities to set the boundaries for the wall wetting. On one hand, an additional sensor can be mounted (e.g., a camera to measure the behavior of the wall film), or on the other hand, the adjacent dynamics have to be identified separately. Due to the fact that the goal of this thesis is a model for control purposes, only the second possibility was considered.

7. Conclusions

The first part of the thesis was dedicated to the investigation of the dynamics adjacent to the wall wetting:

- compensation of the intake manifold dynamics
- modeling of the exhaust gas dynamics
- compensation of the timing error

In the literature, the compensation of the intake manifold dynamics has always been treated as a separate problem, because of the fact that it occurs upstream the wall wetting, and it can be investigated without being influenced by the presence of the fuel puddle.

The exhaust gas dynamics, being downstream the cylinder, cannot be isolated from the wall wetting dynamics when changing the air mass flow in the cylinder of the mass of injected fuel, therefore a different approach based on the emission properties of the combustion engine was chosen [58]. For the main parameters of the exhaust gas dynamics (residual gas fraction and delay), the identification method which was chosen is the efficient method of the frequency response fitting. This method has the advantage to collect and average a large quantity of data for each measured frequency, providing big help not only for systems with a relatively small signal-to-noise ratio [27, pp. 534–536], but for engine systems too. This method was used for the wall wetting dynamics in [53, 60] and for other dynamics in [52]. In order to ensure correct measurements, the positioning of the sensors were investigated by means of a one dimensional flow model of the exhaust duct.

The second part of the thesis is dedicated to the development of the wall wetting model and to the identification of its relevant

parameters. A nonlinear model resulted from this investigation, although the wall film alone is actually a linear, parameter varying model. A remark that can be made is that the empirical model of Aquino [4] is based on the same structure which is yielded by the detailed model. On one hand, this similarity underlines the quality of the Aquino approach, while on the other hand it helps to define the physics behind the empirical parameters proposed by Aquino. The parameters which were obtained with the wall wetting model can thus be used in combination with the existing compensator structures with small changes.

The results obtained with the model on the test bench indicate that an actual reduction of measurements on the test bench in order to calibrate the engine is possible. In addition to this, the model is able to reproduce the wall wetting of cold engine just by tuning one single parameter. Hence, both initial requirements are fulfilled.

The last part of the thesis is focused on the application of the knowledge gained on the wall wetting peculiarities to study different compensating strategies. In particular, the utilization of an estimator (Kalman filter) permitted the on-line tuning of the parameters of the linear compensator and, by the estimation of the internal state variables, the application of a controller. The result of this investigation is that the best compensator approach concerning reactivity and stability is the use of an LPV compensator based on the inversion of the wall wetting dynamics with the parameters monitored to ensure good stability.

To conclude this thesis, a few remarks have to be made:

First of all, the basis for all of the investigations of the wall wetting dynamics has been the measurements with the λ sensor in the exhaust. For this reason, a precision of the sensor under a 1%

7. *Conclusions*

error is needed. However, the performance of the sensor is not constant over its life time. An old sensor is usually slower than a new one.

Second, the aging of the other engine parts is still an issue. Carbon deposits on the intake valves and intake manifold tend to increase the wall wetting phenomenon, changing accordingly the wall wetting parameters [14].

In order to cope with these changes, approaches with on-line adaptation algorithms are needed. In the future, with the introduction of faster ECU processors, an adaptation of all the relevant engine parameters will probably be feasible.

The only possibility to ensure an efficient parametrization and adaptivity of the systems is the reduction of the tunable parameters, on-line and off-line, by means of model-based approaches.

A. Frequency Response Plots

This appendix includes the bode plots of the frequency response of the exhaust gas dynamics measured in the exhaust pipe at different operating conditions.

The response from the model is depicted in the same plots.

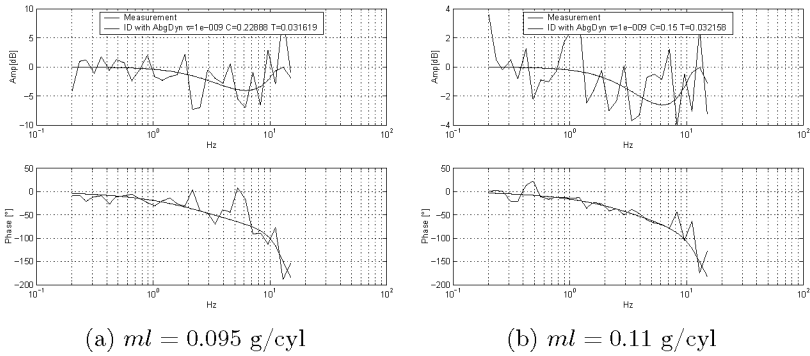
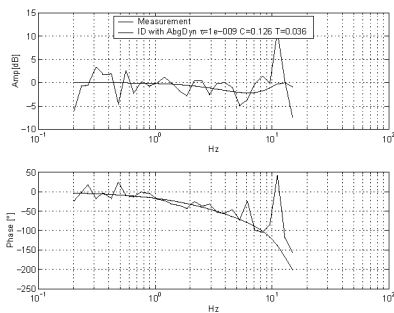
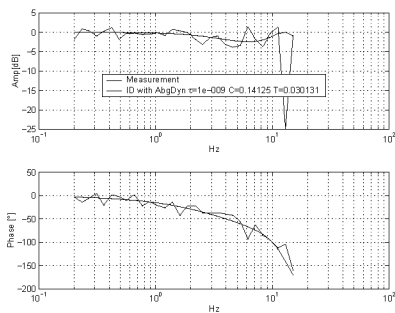


Figure A.1: Bode diagram EGD

A. Frequency Response Plots

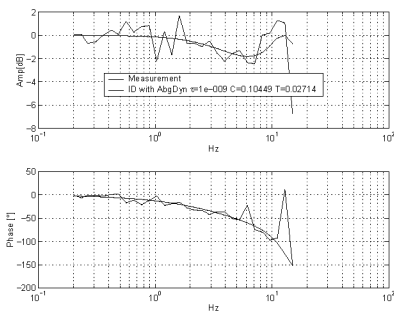


(a) $ml = 0.13$ g/cyl

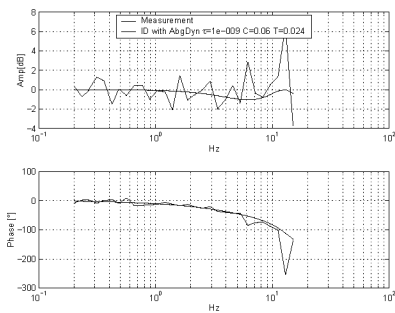


(b) $ml = 0.15$ g/cyl

Figure A.2: Bode diagram EGD

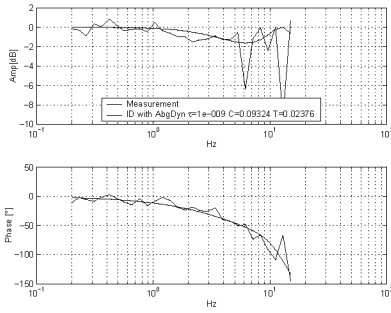


(a) $ml = 0.17$ g/cyl

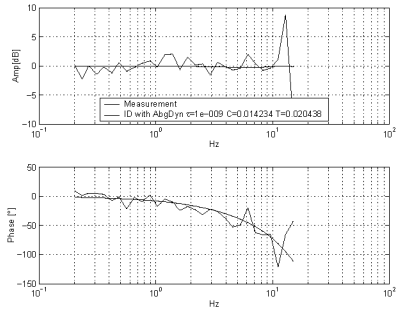


(b) $ml = 0.20$ g/cyl

Figure A.3: Bode diagram EGD



(a) $ml = 0.23$ g/cyl



(b) $ml = 0.30$ g/cyl

Figure A.4: Bode diagram EGD

A. Frequency Response Plots

Bibliography

- [1] A. C. Alkidas. Intake-Valve Temperature and the Factors Affecting it. *SAE Technical Paper Series*, SP-1280(SAE 971729), March 1997.
- [2] A. C. Alkidas. Intake-Valve Temperature Histories During S.I. Engine Warm-Up. *SAE Technical Paper Series*, (SAE 2001-01-1704), March 2001.
- [3] G. Almkvist, I. Denbratt, G. Josefsson, and I. Magnusson. Measurements of Fuel Film Thickness in the Inlet Port of an S.I. Engine by Laser Induced Fluorescence. *SAE Technical Paper Series*, (SAE 952483), March 1995.
- [4] C. F. Aquino. Transient A/F Control Characteristics of the 5 Liter Central Fuel Injection Engine. *SAE Technical Paper Series*, SP-487(SAE 810494), March 1981.
- [5] T. S. Auckenthaler. *Modelling and Control of Three-Way Catalytic Converters*. Diss. ETH No. 15812, ETH Zurich, 2004.
- [6] T. S. Auckenthaler, C. H. Onder, and H. P. Geering. Engine Management without Air Mass Flow Meter. In *Proceedings of the 28th FISITA World Automotive Congress*. FISITA, 2000.

Bibliography

- [7] B. A. Ault, V. K. Jones, J. D. Powell, and G. F. Franklin. Adaptive Air-Fuel Ratio Control of a Spark-Ignition Engine. *SAE Technical Paper Series*, (SAE 940373), March 1994.
- [8] H. D. Baehr. *Thermodynamik*. Springer-Lehrbuch, 8th edition, 1992.
- [9] S. Baltisberger. *Entwicklung eines NO-Messgeräts zur arbeitsspielauflösenden Abgasanalyse an Verbrennungsmotoren*. Diss. ETH No. 11593, ETH Zurich, 1996.
- [10] R. S. Benson, J. H. Horlock, and D. E. Winterbone. *The Thermodynamics and Gas Dynamics of I.C.E.*, volume 1. Clarendon Press Oxford, 1982.
- [11] R. G. Brown and P. Y. C. Hwang. *Introduction to Random Signals and Applied Kalman Filtering*. Wiley & Sons, 3rd edition, 1997.
- [12] H. Butler. *Model Reference Adaptive Control*. PhD Thesis, Technische Universitet Delft, 1990.
- [13] G. Chen, T. W. Asmus, and G. T. Weber. Fuel Mixture Temperature Variations in the Intake Port. *SAE Technical Paper Series*, SP-1178(SAE 961194), March 1996.
- [14] S. S. Cheng. The Physical Parameters that Influence Deposit Formation on an Intake Valve. *SAE Technical Paper Series*, (SAE 922257), 1992.
- [15] J. Cowart and W. Cheng. Intake Valve Thermal Behavior During Steady-State and Transient Engine Operation. *SAE Technical Paper Series*, (SAE 1999-01-3643), March 1999.

- [16] E. W. Curtis, C. F. Aquino, W. D. Plensdorf, D. K. Trumpy, G. C. Davis, and G. A. Lavoie. Modeling Intake Warm-Up. *Fall Technical Conference*, 29-1(97-ICE-40), 1997.
- [17] E. W. Curtis, C. F. Aquino, D. K. Trumpy, and G. C. Davis. A New Port and Cylinder Wall Wetting Model to Predict Transient Air/Fuel Excursions in a Port Fuel Injected Engine. *SAE Technical Paper Series*, SP-1178(SAE 961186), March 1996.
- [18] dSpace GmbH. *ControlDesk, Experiment Guide*, 1.0 edition, 1999. User Manual.
- [19] dSpace GmbH. *Real-Time Interface, Implementation Guide*, 1.0 edition, 1999. User Manual.
- [20] G. T. Engh and C. Chiang. Correlation of Convective Heat Transfer for Steady Intake-Flow Through a Poppet Valve. *SAE Technical Paper Series*, (SAE 700501), March 1970.
- [21] R. Ford and N. Collings. Measurement of Residual Gas Fraction using a Fast Response NO Sensor. *SAE Technical Paper Series*, SP-1418(SAE 1999-01-0208), March 1999.
- [22] H. P. Geering. *Regelungstechnik*. Springer, 5th edition, 2001.
- [23] E. R. Gilliland and T. K. Sherwood. Diffusion of Vapors into Air Streams. In *Industrial and Engineering Chemistry*, volume 26-5, pages 516–523, 1934.
- [24] T. B. Gradinger. *Spray Modeling with Application to Fuel-Air Premixing*. Diss. ETH No. 13497, ETH Zurich, 2000.
- [25] L. Guzzella. Die Anwendung von ICX-1. Internal Report IMRT, 1986.

Bibliography

- [26] L. Guzzella and C. H. Onder. *Introduction to Modeling and Control of Internal Combustion Engine Systems*. Springer-Verlag, 2004.
- [27] R. Haber and L. Keviczky. *Nonlinear System Identification – Input-Output Modeling Approach*, volume 2 of *Mathematical Modelling*. Kluwer Academic Publishers, 1999.
- [28] P. Haluska. *Control Oriented Modeling of Mixture Formation in Spark-Ignition Gasoline Engines*. PhD Thesis, Slovak University of Technology in Bratislava, 1997.
- [29] W. Hentschel, A. Grote, and O. Langer. Measurement of wall film thickness in the intake manifold of a standard production SI engine by a spectroscopic technique. *SAE Technical Paper Series*, SP-1301(SAE 972832), March 1997.
- [30] J. B. Heywood. *Internal Combustion Engine Fundamentals*. McGraw Hill, 2nd edition, 1988.
- [31] J. H. Horlock and D. E. Winterbone. *The Thermodynamics and Gas Dynamics*, volume 2. Clarendon Press Oxford, 1986.
- [32] H. Ihme. Kompensation des Wandfilmeffekts beim Viertakt-Ottomotor. *MTZ Motortechnische Zeitschrift*, 62:584–589, 2001.
- [33] F. P. Incropera and D. P. DeWitt. *Fundamentals of Heat and Mass Transfer*. Wiley and Sons, 4th edition, 1996.
- [34] P. A. Ioannou and J. Sun. *Robust Adaptive Control*. Prentice-Hall, 1st edition, 1996.
- [35] E. W. Kamen and P. Khargonekar. On the Control of Linear Systems Whose Coefficients are Functions of Parameters. In

- IEEE Transactions on Automatic Control*, volume 1-29 of *AC*, pages 25–33. IEEE, 1984.
- [36] E. W. Kamen and J. K. Su. *Introduction to Optimal Estimation*. Grimble, M.J. and Johnson, M.A., Springer, 1999.
- [37] K.K. Kuo. *Principles of Combustion*. Wiley and Sons, 1986.
- [38] H. P. Lenz. *Gemischbildung bei Ottomotoren*. Springer-Verlag, 1990.
- [39] H. P. Lenz, G. K. Fraidl, and H. Friedl. Fuel Atomization with Mixture Preparation Systems of S.I. Engines. *SAE Technical Paper Series*, P-211(SAE 885015), March 1988.
- [40] L. Ljung. *System Identification, Theory for the User*. Prentice-Hall, 2nd edition, 1992.
- [41] M. Locatelli. Non-linear Modeling of the Wall-Wetting Dynamics of an SI-Engine. Diploma work, ETH Zurich, 1999.
- [42] M. Locatelli, C. H. Onder, and H. P. Geering. Exhaust-Gas Dynamics Model for Identification Purposes. *SAE Transactions, Journal of Fuels and Lubricants*(SAE 2003-01-0368), 2003.
- [43] P. J. Maloney. An Event-Based Transient Fuel Compensator with Physically Based Parameters. *SAE Technical Papers Series*, SP-1419(SAE 1999-01-0553), March 1999.
- [44] F. Maroteaux and L. Le Moine. Modeling of Fuel Droplets Deposition Rate in Port Injected Spark Ignition Engine. *SAE Technical Paper Series*, (SAE 952484), March 1995.

Bibliography

- [45] F. Maroteaux and M. Thelliez. Modeling of Unsteady Multi-phase Flow in the Intake Manifold of Spark Ignition Engines. *SAE Technical Paper Series*, (SAE 910392), March 1991.
- [46] B. S. Massey. *Mechanics of Fluids*. Van Nostrand Reinhold, 6th edition, 1989.
- [47] T. Matsumura and Y. Nanyoshi. New Fuel Metering Technique for Compensating Wall Flow in a Transient Condition Using the Model-Matching Method. *JSAE Review*, Vol.10(No.3):5-9, 1989.
- [48] D. Matter. ICX-3, Documentation, Institut für Mess- und Regeltechnik, 1999. User Manual.
- [49] M. Mladek. *Cylinder Pressure for Control Purposes of Spark Ignition Engines*. Diss. ETH No. 14916, ETH Zurich, 2003.
- [50] M. Mladek and C. H. Onder. A Model for the Estimation of Inducted Air Mass and the Residual Gas Fraction using Cylinder Pressure Measurements. *SAE Technical Paper Series*, SP-1511(SAE 2000-01-0958), March 2000.
- [51] P. E. Moraal, D. E. Meyer, A. Cook, and E. G. Rychlick. Adaptive Transient Fuel Compensation: Implementation and Experimental Results. *SAE Technical Paper Series*, SP-1500(SAE 2000-01-0550), March 2000.
- [52] C. H. Onder. *Modellbasierte Optimierung der Steuerung und Regelung eines Automobilmotors*. Diss. ETH No. 10323, ETH Zurich, 1993.
- [53] C. H. Onder, C. A. Roduner, and H. P. Geering. Model Identification for the A/F Path of an SI Engine. *SAE Technical Paper Series*, SP-1236(SAE 970612), March 1997.

- [54] W. H. Piarah. *Numerische Untersuchung des instationären Stofftransports an und in umströmten Einzeltropfen*. PhD Thesis, Technischen Universität Berlin, 2001.
- [55] W. E. Ranz and W. R. Marshall. Evaporation from Drops. In *Chem. Engrg. Prog.*, pages 141–146, March 1952.
- [56] S. M. Schurov and N. Collings. A Numerical Simulation of Intake Port Phenomena in a Spark Ignition Engine Under Cold Start Conditions. *SAE Technical Paper Series*, (SAE 941874), March 1994.
- [57] J. Senda, T. Nishikori, T. Tsukamoto, and H. Fujimoto. Atomization of Spray under Low Pressure Field from Pintle Type Gasoline Engines. *SAE Technical Paper Series*, (SAE 920382), March 1992.
- [58] M. Simons. *Modellbildung und Parameteridentifikation für die Wandfilmdynamik eines Otto-Motors*. Diss. ETH No. 13945, ETH Zurich, 2001.
- [59] M. Simons, M. Locatelli, C. H. Onder, and H. P. Geering. A Nonlinear Wall-Wetting Model for the Complete Operating Region of a Sequential Fuel Injected SI Engine. *SAE Technical Paper Series*, SP-1511(SAE 2000-01-1260), March 2000.
- [60] M. R. Simons, E. Shafai, and H. P. Geering. On-Line Identification Scheme for Various Wall-Wetting Models. *SAE Technical Paper Series*, SP-1357(SAE 980793), March 1998.
- [61] J. J. E. Slotine and W. Li. *Applied Nonlinear Control*. Prentice Hall, 1991.

Bibliography

- [62] B. D. Spalding. *Combustion and Mass Transfer*. Pergamon International Library, 1979.
- [63] R. E. Treybal. *Mass-Transfer Operations*. Mc Graw-Hill, New York, 3rd edition, 1980.
- [64] R. C. Turin. *Untersuchung modellbasierter, adaptiver Verfahren zur Kompensation der Gemischbildungsdynamik eines Otto-Motors*. Diss. ETH No. 9999, ETH Zurich, 1992.
- [65] P. Zarchan and H. Musoff. *Fundamentals of Kalman Filtering: A Practical Approach*. American Institute of Aeronautics and Astronautics, Inc., 2000.

Curriculum Vitae

Marzio Locatelli

- December 9, 1975 Born in Lugano, Switzerland
- 1981-1986 Elementary School in Davesco, TI, Switzerland
- 1986-1990 Middle School in Viganello, TI, Switzerland
- 1990-1994 High School in Lugano, TI, Switzerland
- 1994 Scientific Matura
- 1994-1999 Studies in mechanical engineering, ETH Zurich
Majors: combustion engines and automatic control
- 1999 Diploma in mechanical engineering,
ETH Zurich
- 1999-2004 Teaching and Research Assistant at the
Measurement and Control Laboratory,
Department of Mechanical Engineering,
Swiss Federal Institute of Technology (ETH),
Zurich, Switzerland
Teaching assistance in Engine Systems and
Adaptive Control
- 2001-2004 Research on the topic of this thesis